UNIVERSITY OF CRETE
DEPARTMENT OF CHEMISTRY
POSTGRADUATE PROGRAMME

MASTER THESIS

EFFECT OF MOLECULAR WEIGHT AND STAR SHAPED ARCHITECTURE ON CONDUCTIVITY OF POLY(ETHYLENE OXIDE) ELECTROLYTES

Dimitrios Chatzogiannakis

Supervisors:

Dr. Emmanouil Glynos
Prof. Spiros H. Anastasiadis

HERAKLION 2020

ΠΑΝΕΠΙΣΤΗΜΙΟ ΚΡΗΤΗΣ

ΤΜΗΜΑ ΧΗΜΕΙΑΣ

ΓΕΝΙΚΟ ΜΕΤΑΠΤΥΧΙΑΚΟ ΠΡΟΓΡΑΜΜΑ ΣΠΟΥΔΩΝ

ΜΕΤΑΠΤΥΧΙΑΚΟ ΔΙΠΛΩΜΑ ΕΙΔΙΚΕΥΣΗΣ

ΕΠΙΔΡΑΣΗ ΜΟΡΙΑΚΟΥ ΒΑΡΟΥΣ ΚΑΙ ΑΣΤΕΡΟΕΙΔΟΥΣ ΑΡΧΙΤΕΚΤΟΝΙΚΗΣ ΣΤΗΝ ΑΓΩΓΙΜΟΤΗΤΑ ΗΛΕΚΤΡΟΛΥΤΩΝ ΠΟΛΥ(ΑΙΘΥΛΕΝΟΞΕΙΔΙΟΥ)

Δημήτριος Χατζογιαννάκης

Επιβλέποντες:

Δρ. Εμμανουηλ Γλυνός
Καθ. Σπύρος Αναστασιάδης

ΗΡΑΚΛΕΙΟ 2020

To my parents and
my uncle Manolis

Εξεταστική Επιτροπή

Σπύρος Αναστασιάδης

Καθηγητής, Τμήμα Χημείας, Πανεπιστήμιο Κρήτης

Γεώργιος Σακελλαρίου

Αναπληρωτής Καθηγητής, Τμήμα Χημείας, Εθνικό και Καποδιστριακό Πανεπιστήμιο Αθηνών

Ευάγγελος Χαρμανδάρης

Αναπληρωτής Καθηγητής, Τμήμα Μαθημετικών & Εφαρμοσμένων Μαθηματικών, Πανεπιστήμιο Κρήτης

Examination Committee

Spiros H. Anastasiadis

Professor, Department of Chemistry, University of Crete

George Sakellariou

Associate Professor, Department of Chemistry, National and Kapodistrian University of Athens

Evangelos Harmandaris

Associate Professor, Department of Mathematics and Applied Mathematics, University of Crete

CONTACT

chatz095@hotmail.gr

+30 6940055553

Dionysou, 31
Heraklion, Greece

EXPERTISE

Chemistry

Polymer Physics

Data Analysis

Scientific Writing

ADDITIONAL SKILLS

Electronics

Programming

3D Printing

CAD

Photography

LANGUAGES

English (Proficient)

German (B1)

DIMITRIOS CHATZOGIANNAKIS

Profile

Chemist soon (Fall 2020) to finish MSc in Physical Chemistry regarding Polymer Electrolytes. Passionate about research, exploring and DIY. 4 Years of Research Experience at Foundation for Research and Technology-Hellas as under- and post- graduate student.

Academic and Education

2010-2013	8th High School of Heraklion (18.6 / 20)
2013-2017	BSc in Chemistry, Chemistry Dpt. University of Crete (7.88 / 10)
2017-present	MSc Physical Chemistry, Chemistry Dpt. University of Crete (8.83 / 10*)
	Research Assistant at Institute of Electronic Structure and Laser (IESL) of the Foundation for Research and Technology - Hellas (FORTH)

Research

2017	**Academic Thesis** *"Effect of Salt Concentration on the size of core-shell charged polymeric nanoparticles"* (Supervisor: Prof. Spiros H. Anastasiadis)
2018	Emmanouil Mygiakis, **Dimitrios Chatzogiannakis**, Emmanouil Glynos, Georgios Sakellariou *"Synthesis and characterization of well-defined miktoarm star polymers, (PS)n(PEO)n"* (Poster presented at 12th Hellenic Polymer Society International Conference)

*Before Thesis Defense

ANALYTICAL TECHNIQUES

Chemical Analysis

IR Spectroscopy

Raman Spectroscopy

NMR Spectroscopy

UV-Vis Spectroscopy

Structural Analysis

Dynamic Light Scattering

Static Light Scattering

Powder X-Ray Diffraction

Polarized Optical Microscopy

Scanning Electron Microscopy

Transmission Electron Microscopy

Thermal Analysis

Differential Scanning Calorimetry

Thermo-Gravimetric Analysis

Electrical Analysis

Electrochemical Impedance Spectroscopy

COMPUTER EXPERIENCE

MS Office

OriginLab

Python

Arduino

Autodesk Fusion 360

Autodesk Eagle

Adobe Photoshop

Adobe Lightroom

Adobe Premiere

2019	Lampros Papoutsakis, Georgia Nikolakakou, **Dimitrios Chatzogiannakis**, Paraskevi Petropoulou, Alkmini D. Nega, Emmanouil Mygiakis, Georgios Sakellariou, Emmanouil Glynos, Spiros H. Anastasiadis *"Structure-Property Relationship in Mikto-arm Star/Linear Polymer Blends"* (Poster presented at European Polymer Federation annual conference 2019)
2020	**MSc Thesis** *"Effect of Molecular Weight and Star shaped architecture on the conductivity of Poly(ethylene oxide) based Electrolytes"* (To be defended, Fall 2020) (Supervisor: Prof. Spiros H. Anastasiadis)

Other Actions

2015	Volunteer Assistant at Organic Chemistry Undergraduate Laboratory
2017	Volunteer at Hellenic Polymer Society Conference
2018	Physical Chemistry undergraduate Laboratory Teaching Assistant
2018	General Chemistry undergraduate Laboratory Teaching Assistant
2019	Member of the Organizing committee of the 21st Chemistry Postgraduate Conference of University of Crete.
2019	Member of the Organizing committee of Chemists' Vocational Guidance Workshop in University of Crete.
2019	Volunteer at European Polymer Federation Annual International Conference 2019

Περίληψη

Κατά την παρούσα μεταπτυχιακή εργασία, προσπαθούμε να καταλάβουμε την επίδραση του Μοριακού βάρους του γραμμικού πολυ(αιθυλενοξειδίου) (PEO) καθώς και της αστεροειδούς αρχιτεκτονικής στις θερμικές και ηλεκτρικές ιδιότητες πολυμερικών ηλεκτρολυτών. Αρχικά, σχεδιάστηκε, κατασκευάστηκε, ελέγχθηκε και βελτιστοποιήθηκε ένας ατμοσφαιρικός θάλαμος για την μέτρηση της ιοντικής αγωγιμότητας των ηλεκτρολυτών κάτω από ελεγχόμενη ατμόσφαιρα και θερμοκρασία. Παρασκευάστηκαν ηλεκτρολύτες διαφόρων μοριακών λόγων Λιθίου προς αιθυλενοξειδίο, r = $[Li^+]$ / [EO] στους οποίους, για να κατανοήσουμε την επίδραση των μακρομοριακών χαρακτηριστικών του PEO στην σχέση δομής - ιδιοτήτων, η ηλεκτρική αγωγιμότητα τους αγωγιμότητα συνδυάστηκε με μετρήσεις Διαφορικής Θερμιδομετρίας Σάρωσης, Φασματοσκοπίας Raman καθώς και ρεολογίας. Στην περίπτωση των ηλεκτρολυτών βασισμένων σε γραμμικό PEO, βρέθηκε οτι η αγωγιμότητα μειώνεται καθώς αυξάνεται το μοριακό βάρος και καταλήγει σε πλατό για μοριακά βάρη μεγαλύτερα των 2 kg/mol. Το αστεροειδές PEO με μεγάλο αριθμό κλάδων της εργασίας φέρει ιξώδες μηδενικού ρυθμού διάτμησης (Zero Shear Viscosity) 5 τάξεις μεγέθους υψηλότερο από τα γραμμικά μόρια με την αγωγιμότητα του να μειώνεται λιγότερο από μία τάξη μεγέθους. Η ανάπτυξη στερεών ηλεκτρολυτών με υψηλή αγωγιμότητα ερευνάται σημαντικά καθώς βρίσκει εφαρμογές σε μπαταρίες λιθίου, κυψέλες καυσίμων, φωτοβολταϊκά καθώς και άλλα συστήματα ενέργειας.

Λεξεις Κλειδιά: Στερεοί Πολυμερικοί Ηλεκτρολύτες, Πολυ(αιθυλενοξείδιο), Ιοντική Αγωγιμότητα, Κρυσταλλικότητα, Μπαταρίες Λιθίου

Abstract

Throughout this *MSc* Thesis, we try to understand the effect of linear poly (ethylene oxide), PEO, molecular weight (M_w) and star-shaped macromolecular architecture on the thermal and electrical properties of polymer electrolytes. The starting point of this work is the design, the fabrication and the evaluation/optimization of a custom-, home-made environmental chamber for the measurement of ion-conductivity of the polymer electrolytes under consideration in controlled atmosphere and temperature. Several different electrolytes were prepared having different molar ratios of the lithium salt, $r = [Li^+]/[EO]$. To gain insight on the effects PEO macromolecular characteristics on the structure-property relationship of polymer electrolytes, the ion conductivity measurements were combined with differential scanning calorimetry, Raman spectroscopy, and rheology. In the case of linear PEO polymer electrolytes, the ion-conductivity was shown to decrease with molecular weight, reaching a plateau for M_w larger than around 2 kg/mol. Notably, star-shaped PEO with larger number of arms based electrolytes showed five orders of magnitude increase in their mechanical properties (zero shear viscosity) while the ion-conductivity was less than an order of magnitude lower than the corresponding linear electrolytes. Because the design of mechanical robust electrolytes with superior ion conductivity at room temperature has been the subject of research for other energy-related applications, like anion exchange membranes for fuel cells, or efficient active layers in dye-sensitized solar cells, we believe our findings are of great interest to the corresponding scientific community.

Keywords: Solid Polymer Electrolytes, Poly(ethyleneoxide), Ionic Conductivity, Crystallization, Lithium Batteries

Acknowledgements

After the long trip of my MSc studies, the outcome for me is much much more than this thesis. The days I spent in the lab were full of valuable conversations about science (duh), life, cooking, music and generally, many more subjects I could possibly mention here. I went through happy and sad moments as well as exciting and boring ones yet all of them contributed to an overall unforgettable experience. This part is about saying "Thank you" to all those who contributed to those moments.

Starting, I would like to thank **Dr. Emmanouil Glynos** for supervising me throughout this study. I am very grateful about the time we spent together and the conversations we had in and out of the lab as those contributed greatly to my knowledge on polymers. For the opportunity to pursue my goals and for greatly inspiring me through lessons, conversations and presentations, I want to heartily thank **Prof. Spiros H. Anastasiadis**.

Throughout my study, the support of people at FORTH had great influence to my understanding on a subject as well as the final results of the project. For assisting me in various ways, I want to thank **Lampros Papoutsakis, Antonis Mavromanolakis** and **Georgia Nikolakakou.** Of paramount importance was also the contribution of **Prof. George Sakellariou** and his group, especially **Dr. Emmanouil Mygiakis** for synthesizing/providing molecules necessary for our study, along with valuable information.

People that worked in the hybrid nanostructures group, either on the same project or not also contributed greatly to the overall experience and memories I gained. Some of them I want to say a large "Thank you" to are **Dr.Chrisopoulou, Tasos, Lina** and **Fanis** for the many fruitful conversations about everything and **Hellen, Antigonos, Sokratis, Liana, Niki** as well as **Georgia** and **Michaela** for all the fun time we spent together working in the lab.

Closing, the largest thank you goes to my parents, **Maria** and **George**, along with my sister **Alexandra** as they never stood as an obstacle to my goals and always supported my decisions. Last but definitely not least, I want to thank every friend of mine that was involved in this thesis emotionally, or spent time studying with me.

This research has been cofinanced by the European Union and Greek national funds through the Operational Program Competitiveness and innovation, under the call RESEARCH – CREATE – INNOVATE (Project No. T1ΕΔΚ-02576):

Thank you

FORTH
INSTITUTE OF ELECTRONIC STRUCTURE AND LASER

Ευρωπαϊκή Ένωση
Ευρωπαϊκό Ταμείο Περιφερειακής Ανάπτυξης
ΕΛΛΗΝΙΚΗ ΔΗΜΟΚΡΑΤΙΑ
ΥΠΟΥΡΓΕΙΟ ΟΙΚΟΝΟΜΙΑΣ & ΑΝΑΠΤΥΞΗΣ
ΕΙΔΙΚΗ ΓΡΑΜΜΑΤΕΙΑ ΕΠΑ & ΤΕ
ΕΙΔΙΚΗ ΥΠΗΡΕΣΙΑ ΔΙΑΧΕΙΡΙΣΗΣ ΕΠΑνΕΚ
ΕΠΑνΕΚ 2014-2020
ΕΠΙΧΕΙΡΗΣΙΑΚΟ ΠΡΟΓΡΑΜΜΑ
ΑΝΤΑΓΩΝΙΣΤΙΚΟΤΗΤΑ ΕΠΙΧΕΙΡΗΜΑΤΙΚΟΤΗΤΑ ΚΑΙΝΟΤΟΜΙΑ
ΕΣΠΑ 2014-2020
ανάπτυξη - εργασία - αλληλεγγύη
Με τη συγχρηματοδότηση της Ελλάδας και της Ευρωπαϊκής Ένωσης

Table of contents

1.Introduction

1.1 Motivation

Latest years have been marked by the global warming effect, largely caused by CO_2 emissions from fossil fuel burning. Temperature trends worldwide have alarmed scientists and future predictions are quite dreadful. Simultaneously, energy consumption increases constantly and the humanity is in desperate need of more eco-friendly sustainable energy sources, especially since the available amount of fossil fuels decreases. There has been a great amount of research worldwide on the improvement of renewable energy sources with the main ones being hydropower, wind and solar and less popular the tidal, geothermal and biomass. Figure 1.1 below shows some main trends regarding energy production worldwide.[1]

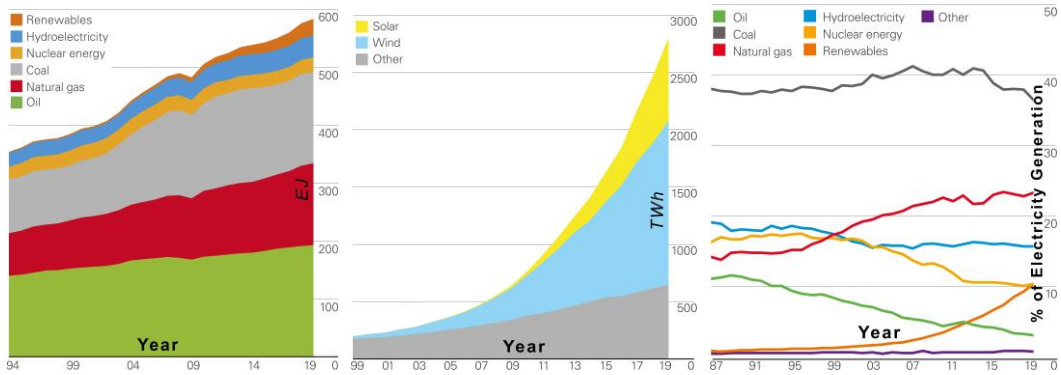

Figure 1.1: (Left) Primary energy consumption (*EJ*) each year by source. (Middle) Renewable energy (TWh) generation each year by source. (Right) Electricity generation percentage each year by source. (Reprint from BP Statistical Review of World Energy 2020 [1].)

What is apparent from Figure 1.1 is that both the energy demand worldwide is increasing significantly and that only a very small fraction is coming from renewable sources. As that results, the annual total CO_2 emissions have increased tremendously over the latest years (Figure 1.2, left), with alarming consequences for the environment, as for example the increasing global temperature (Figure 1.2, right).

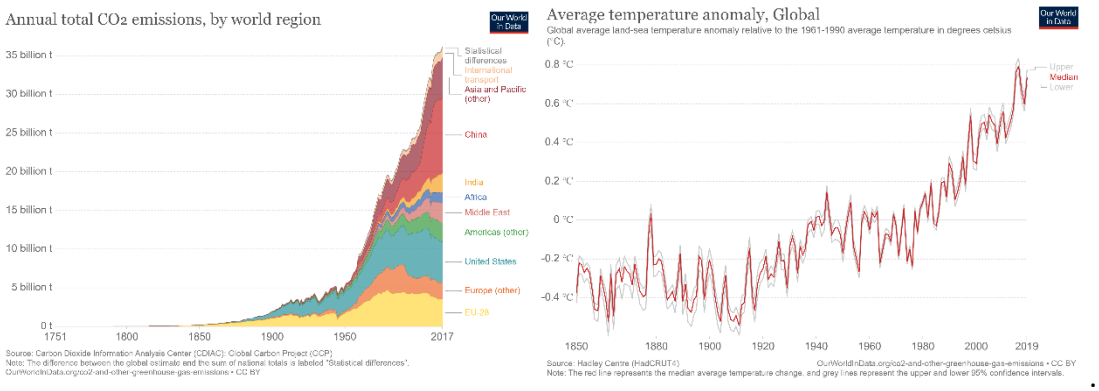

Figure 1.2: (Left) Trend of Annual CO_2 emissions and (Right) global average land-sea temperature relative to 1961-1990. (Sources written on the graphs, Reprint from OurWorldInData.org)

The major problem of the most common renewable energy sources (like solar and wind energy) is that they are scattered in place and time. For example, wind is unpredictable and not daily, while sunlight availability peaks in midday, when not cloudy and when power demands are relatively low. At night, when electricity demand reaches its peak, sunlight is unavailable. The above problem implies that efficient energy storage systems that act as energy buffers are essential for the realization of a green energy landscape where wind turbines or solar panels will be efficiently integrated, meeting the energy demands of the society. Currently, the most used renewable energy source (Figure 1.1a) is hydroelectricity largely due to the fact that there is a way of storing and selectively utilizing the potential energy of water. This is done by pumping water to high altitudes when demands are low, and utilizing it when demands peak (i.e. pumped storage hydroelectricity) (source: National Hydropower Association, NHA)

1.2 Electrochemical Energy Storage Systems-Batteries

Batteries are devices that store electrical energy by converting it to chemical. Using batteries to address the problem mentioned above is a viable solution with some commercial products already available such as Tesla's Powewall introduced in 2015. Aside the fact that batteries can be of major importance for renewable energy source utilization, their importance can be easily seen in personal level too with them being a major part of consumer electronics such as cell phones and laptops. Consumer electronics are getting more and more powerful and batteries have a hard time keeping up with their energy requirements and as a consequence the market of powerbanks has also grown significantly in the latest years.

Current research on batteries is focused on improving their charge capacity while reducing their weight and volume as it is crucial for some applications such as automotive. Typically, the terms *specific energy density* (*Wh/kg*) and *Volumetric energy density* (*Wh*/*L*) are used to compare batteries' performance. Furthermore, secondary batteries deteriorate as they are cycled (limited life time / cycle life) and all batteries lose charge if stored for long time (self-discharge). Last but not least, currently used batteries are highly unsafe as there have been numerous accidents involving them, especially improperly used *Li-ion,* and this is attributed to the flammable liquid electrolytes currently used. Ideally in terms of performance, a battery optimized for portable applications should possess both high specific and volumetric energy densities while being safe to use in everyday life as a part of a car, a cell phone, a computer etc. On the other hand, stationary batteries like batteries that could be used for grid storage should rely more on their cycle life and low cost in order to be successful.

Throughout the years, many different battery chemistries have been developed and utilized. The currently used batteries can be divided into two main categories: Primary (non-Rechargeable) and Secondary (Rechargeable). The working principle of all batteries is based upon two half-reactions, one oxidation and one reduction. The electrode where oxidation happens is named "anode" and the one where reduction happens "cathode". The two half-reactions add up to one full redox

reaction (with $\Delta G < 0$) progressing as power is drawn from the battery. When the reagents are exhausted, battery ceases to function. In case of secondary batteries, they can be recharged by driving current through them to reverse the redox reaction and re-obtain the initial reagents. Some of the most common reactions involved in everyday batteries are presented below (red symbolizes the ion traveling through the electrolyte) and Figure 1.3 schematically represents the functions and structure of a secondary battery[2]:

1. **"*Alkaline*" Battery (Primary)[3]:**

Oxidation: $Zn + 2OH^- \rightarrow ZnO + H_20 + 2e^-$

Reduction: $2MnO_2 + 2H_2O + 2e^- \rightarrow 2MnOOH + 2OH^-$

Full : $Zn + 2MnO2 + H_2O \rightarrow ZnO + 2MnOOH$

2. **"*Lead-acid*" Battery (Secondary)[2]**

Oxidation: $Pb + HSO_4^- \Leftrightarrow PbSO_4 + H^+ + 2e^-$

Reduction: $PbO_2 + 3H^+ + HSO_4^- + 2e^- \Leftrightarrow 2H_2O + PbSO_4$

Full: $PbO_2 + Pb + 2H_2SO_4 \Leftrightarrow 2PbSO_4 + 2H_2O$

3. **"*Li-ion*" Battery (LCO) (Secondary)[4]**

Oxidation: $Li_xC_6 \Leftrightarrow xLi^+ + xe^- + C_6$

Reduction: $Li_{1-x}CoO_2 + xLi^+ + xe^- \Leftrightarrow LiCoO_2$

Full : $Li_{1-x}CoO_2 + Li_xC_6 \Leftrightarrow LiCoO_2 + C_6$

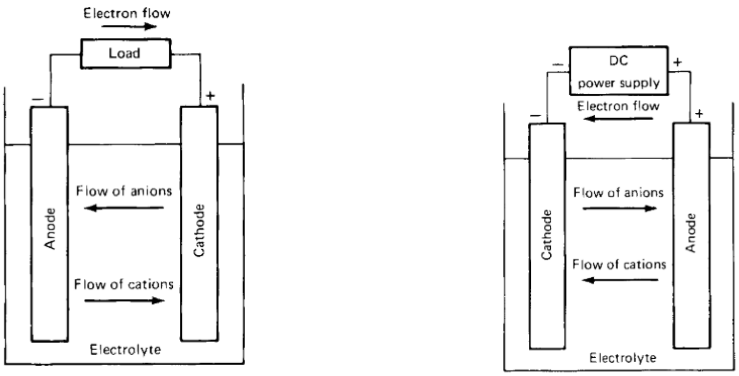

Figure 1.3: Schematic representation of a secondary battery during (Left) Discharging and (Right) Charging. A primary battery has the same behaviour during discharging but cannot be recharged.[2] (Reprint from Ref.2)

Of course, even though the energy density and operating voltage of a battery mainly depend on the redox reaction between its electrodes' active materials, the electrolyte used between them is also a crucial component that has significant effect on the final performance of the battery. Most importantly, a suitable electrolyte should be highly ionically conductive and simultaneously an electric insulator. At the same time, it should not chemically react with any of the other battery components and be able to withstand the operating voltages. Last but not least, it should be thermally stable, ideally nontoxic and finally cost effective.

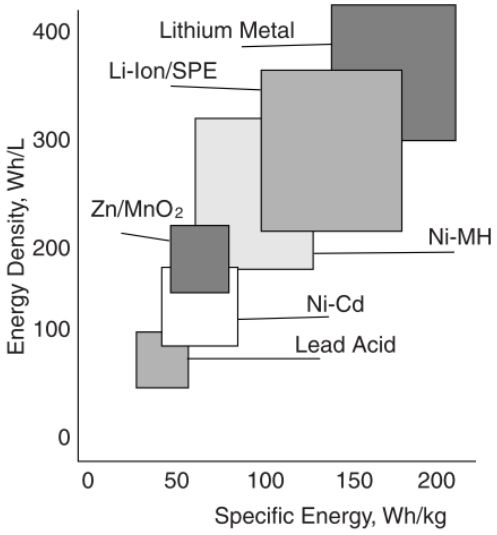

Figure 1.4: Energy storage capabilities of common secondary battery types clearly showing the superiority of Lithium based batteries. Squares represent performance variation due to operating conditions (Reprint from Ref. 2)

A comparison of the most common secondary battery types is presented in Figure 1.4. It is clear that batteries using Lithium metal as an anode significantly outperforms other existing technologies due to Lithium's very low redox potential of -3.04V (vs SHE) and its lightweight nature (Density = 0.534 g/cm^3) giving it the highest theoretical energy density.[4,5,6]

The currently used LIBs are composed of a liquid electrolyte, which is a mixture of a Lithium salt dissolved in an organic solvent, sandwiched between two Lithium-intercalating electrodes. Despite their high ionic conductivity, liquid electrolytes are incompatible with Lithium metal with many safety issues. Currently one of the most difficult challenges to the development of Lithium metal batteries (LMBs), stems from the uneven dendritic Lithium electrodeposition on the negative electrode.[7,8] Once nucleated, these dendrites concentrate the electric field near their tips, which facilitates continuous undesirable, out-of-plane electrodeposition. The growing dendrites have at least two damaging consequences on cell operation. First, the high surface area structures continuously react with the electrolyte solvent to form solid electrolyte interface, which will eventually consume the electrolyte drying out the cell, and cause premature cell failure. Second, unrestrained growth of dendrites creates an electrically conductive connection between the two electrodes, causing the cell to short circuit. In a volatile flammable electrolyte, the dendrite-induced short is both a potential fire and explosion hazard, leading to a catastrophic failure of the battery.[5,6,9,10]

1.3 Solid Polymer Electrolytes (SPE)

After the theoretical prediction by Monroe and Newman that a mechanically robust electrolyte with a shear modulus in the order of GPa would mechanically suppress/block macroscopic dendrite formation, significant research efforts have focused on the development of solid state electrolytes, capable of eliminate the dendrite formation, with high ionic conductivity at room temperature[11]. Solid state electrolytes mainly fall into two categories: inorganic ceramic electrolytes and solid

polymer electrolytes. Despite the fact that inorganic ceramics exhibit satisfactory ionic conductivity and mechanical properties that range from tens to hundreds of GPa, the lack of good adhesion to Lithium electrodes (high modulus materials often do not afford good adhesion) significantly increases interfacial resistance during cycling[12]. Moreover, the electrochemical stability window of ceramic electrolytes is very narrow[13]. To this end, the use of *solid polymer electrolytes* (SPEs) represents the ultimate solution due to their chemical stability toward Lithium metal electrodes and their mechanical resistance to dendrite growth. Furthermore, the adhesion between solid polymer electrolytes and the electrodes is much better than for ceramics, and most SPEs exhibit good flexibility and scalable fabrication, which is favorable for practical battery manufacturing. In addition, having no liquid components makes solid polymer electrolytes leak safe and removes the need for a separator between the two electrodes.

1.4 Poly(ethylene oxide) based solid state electrolytes

Since the groundbreaking findings of Fenton, Parker and Wright reporting the interaction of Alkali ions with Poly(ethylene oxide) in 1973[14], followed by the works of Armand shortly after, regarding the use of such substances as electrolytes[15], PEO-based polymers have gained a great amount of research attention for their potential use as solid state electrolytes in Lithium-ion batteries. The EO group is the key for PEO to dissolve the lithium salt and transport the lithium ions. The ether oxygen atoms on the PEO chains coordinate with the lithium ions, resulting in the dissociation of cations and anions. Owing to the coordination/dissociation between the lithium ions and the oxygen atoms (Li-O), PEO is ionically conductive, while it has good thermal stability, and does not chemically react with any other battery component. At the same time, it can withstand operating voltages, is not toxic and its cost is reasonable[16,17]. The main drawback of PEO based electrolytes is the low room temperature ionic conductivity that is due to its high crystallinity as ion transport occurs via the amorphous PEO regions.[18]

1.4.1 The effect of Crystallinity

As mentioned before, an important property of such electrolytes that needs to be discussed is the high tendency of PEO to crystallize. There have been reports of ionic mobility within a crystalline phase[19,17] yet the observed behaviour and widely accepted view is that ion conduction happens through the amorphous phase, as crystallization of a PEO:Salt type electrolyte heavily reduces sample's conductivity[20,21,18]. In the case of LiTFSI and PEO, introducing salt in the polymer reduces the degree of crystallinity of PEO due to the strong interactions of the EO groups with the Lithium ion. Interestingly, because LiTFSI forms complexes with PEO's backbone, at high salt concentrations these complexes can also crystallize. There is a region of concentrations between those two phenomena that the electrolyte stays completely amorphous at room temperature referred to as "crystallinity gap" and this where most of the research interest is focused. The phase diagram of the LPEO-LiTFSI system is depicted in Figure 1.5 as reported by Armand et.al.[20,22,23,24,25]

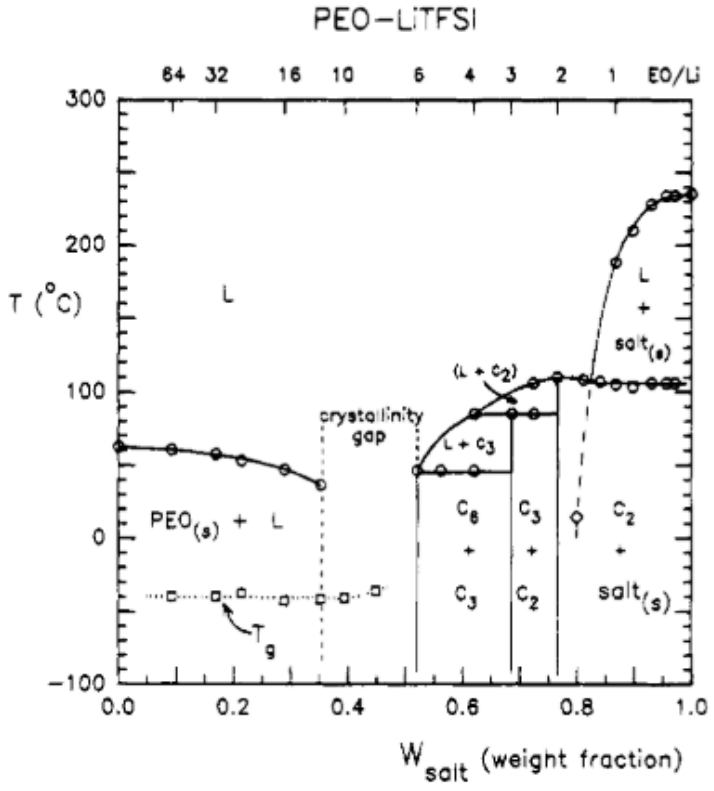

Figure 1.5: Phase diagram of LPEO:LiTFSI system showing the crystallization gap where the blends stay amorphous. [Reprint from Ref. 25] [25]

1.4.2 Mechanism of ion conduction/transport

As stated earlier, Li^+ conduction proceeds through PEO's amorphous regions. There are two main mechanism for that. The first and most important is the so-called "*hopping*" or "*fluctuation driven diffusion*" and is the dominant mechanism for PEO molecular weights above the molecular weight for entanglement (M_e>2*kg/mol*)[26]. In this case, segmental motions distort the structure of the Li-O complexes, and ion movement occurs in the presence of an electric field through bond breaking and reforming. The rate of ion diffusion or ion conductivity of this type is coupled with the segmental dynamics of the polymer chains. [27,28]

The second mechanism is called "*vehicular diffusion*" and occurs only in very low molecular weight PEO, below the PEO molecular weight for entanglements (M_e<*2kg/mol*).[26] During this, the force exerted on Lithium ions can move the polymer chains bound to it towards the direction of the electric field[27]. The speed of this process is absent/very slow above the molecular weight of entanglement and its speed is dictated by the viscosity of the polymer. The total conductivity of the electrolyte can have contributions from both conduction mechanisms yet at high molecular weights the entirety of conductivity is of the *"fluctuation driven"* type.

As explained above, maybe the most important parameter influencing conductivity is polymer's segmental dynamics.[28] Fast segmental dynamics facilitate ion conduction and thus the glass transition temperature, closely related to segmental relaxation of the polymer chains, should be kept as low as possible. Any modification that increases the T_g is thus expected to have a negative impact on ionic conductivity and design of PEO based SPE's should always take that into account.

1.4.3 The effect of salt concentration

The ionic conductivity of polymer electrolyte systems is given by:

$$\sigma_{dc} \propto \sum_i \mu_i q_i n_i \qquad [Eq.\,1.1]$$

Where *i* is each ion, μ_i is the mobility of the ion, q_i is its charge and n_i its concentration

It has been shown from multiple reports that PEO's DC conductivity shows a non-monotonic trend as a function of LiTFSI concentration[22,29,30]. Two factors govern the aforementioned phenomenon; one is the increase of the mobile ions' concentration (*n*) and the other is the slowing down of the polymer's segmental dynamics, both happening as *r* = [Li^+] / [EO] increases. It is well known that fast segmental dynamics enhance conductivity in amorphous polymers[28] and this fact causes ions in samples with low *r* to have higher mobility (μ) than the corresponding ions in a sample of higher *r*. The above phenomena have been measured by Balsara et.al. and their findings are depicted in Figure 1.6.

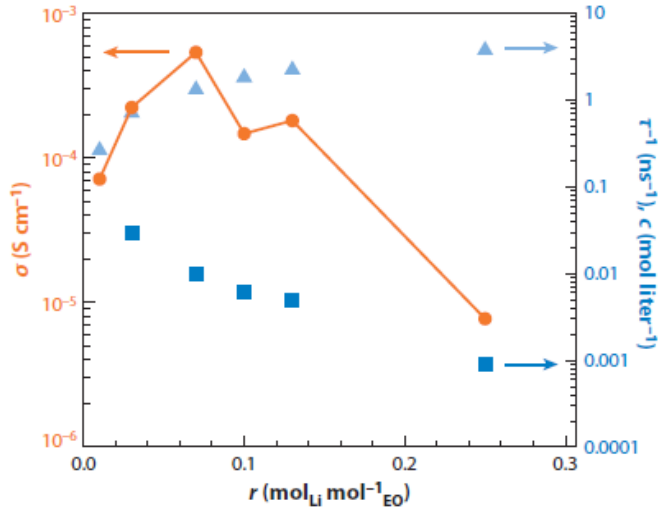

Figure 1.6: Experimental measurements showing (Squares, Right axis) segmental dynamics of polymer, (Triangles, Right axis) Concentration of ions and the resulting (orange circles, Left axis) D.C. Conductivity. [Reprint from Ref.27] [27]

1.4.4 Star-shaped Polymers

Polymer stars is the simplest branched type of polymers. They consist of polymer chains (arms) bound from one side onto a common core. The number of arms attached to the core is called “functionality” of the star and is usually symbolized as *f*. A schematic representation of a star-shaped polymer can be seen in Figure 1.7.

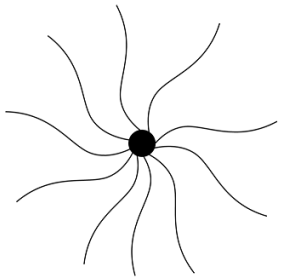

Figure 1.7: Representation of a star-shaped polymer with *f*=10.

Star-shaped polymers, depending on the functionality and the arm length (degree of polymerization per arm, N_{arm}), may possess very large density heterogeneities due to the non-uniform, non-monotonic, monomer intramolecular density profile around the core particle: the density is higher close to the core, where arm monomers touch each other, and decreases towards the corona of the star polymers.[31,32] As a result, with increasing functionality, star polymers progressively have less tendency to overlap with each other, they cannot occupy random position in an incompressible melt and start to correlate spatially. The impact of functionality is equivalent to the entropic repulsion observed in solutions of star polymers, where the effective interactions between the stars can be tuned by functionality ranging from ''soft'' as in linear chains or as ''hard'' as colloidal particles.[33–35] At the same time, for a given functionality, the increase of the degree of polymerization of each the arms, increases the structural disorder of the system, as the system starts to interpenetrate. The emergence of the structural ordering of stars with increasing *f* has be reported also experimentally with small angle x-ray scattering measurements.[36–38] Bead spring MD simulations of the non-entangled stars in melts revealed that the intramolecular monomer density

heterogeneity results in a distribution of segmental dynamics where the relaxation times strongly depend on the monomer position along the arm; the segmental dynamics get slower towards the core and speeds-up towards the chain end.(Figure 1.8)[39]

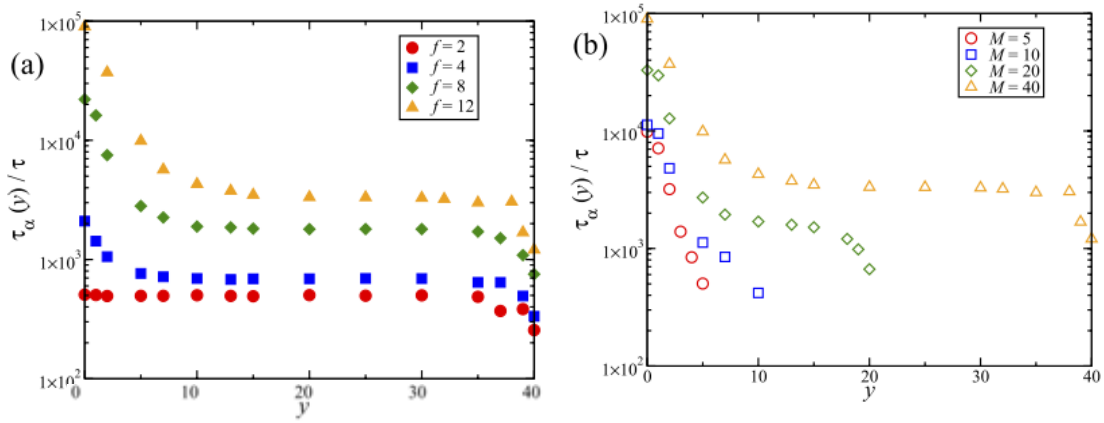

Figure 1.8: Structural relaxation time, τ_α, along a grafted chain at T = 0.5 for (a), M = 40 at different values of f and for (b), f = 12 at different values of M. The values of y correspond to the position of the bead y along the arm with y = 0 and y = M being the core particle and the free-end, respectively. [Reprint from Ref. 44][39]

Spatial density heterogeneities that come from the intramolecular heterogeneities, heterogeneous intramolecular distributions, of the star-shaped polymeric materials results in a very rich and complex dynamical behavior. The dynamic response of multiarm stars in the melt has been studied extensively.[37,40–42] In the case of linear chain melts, which may be thought as density homogeneous material, several models have been introduced to describe their dynamics. For linear chain molecular weights, M_w, below the critical molecular weight for entanglements, M_e, the dynamics are well described by the Rouse model[43], that predicts that the shear viscosity, η, scales as the square of the polymer chain radius of gyration, R_g, i.e. $\eta \sim R_g^2$, or linearly with the molecular weight, $\eta \sim M_w$.[44] The diffusion coefficient, D, for low molecular weight chains is inversely proportional to M_w as the friction coefficient is proportional to the chain length.[43,45,46] These findings are in agreement with experimental data on 4-arm star polymers, where NMR measurements

confirmed a distribution of relaxation times along the arms.[32] The relaxation time becomes shorter as one moves from the center to the outer part of the molecule.

When the linear polymer chain becomes long enough, entanglements between linear chains are formed, and stronger scaling of shear viscosity with the linear chain molecular weight is observed, $\eta \sim M_w^{3,4}$.[44] In entangled polymer chain systems, the reptation (snake-like) motion in the tube, has been very successful in describing the relaxation mechanisms involved, and in agreement with experiments, D scales as , $D \sim M_w^{-2}$. Due to their architecture, star-shaped polymers, depending on the functionality and arm length, display hallmarks of both polymers and colloids, having a hierarchy of length and times scales in their dynamics. For entangled star-shaped polymers with low functionalities and long arms, the center of mass motion is facilitated by the arm retraction mechanism, wherein the arm moves along the primitive path within a tube towards the core.[47–49] As the arm retraction process is entropically unfavorable, the diffusion of a star-shaped polymers diffusion much slower and D depends exponentially on M_w of the arm, M_w^{arm}. With increasing functionality, the longest relaxation time (terminal time that is associated with the center of mass diffusion), is characterized by a two-step relaxation mechanism, in contrast to a single terminal relaxation process of low functionality stars, linear homopolymers, or even colloidal particles. In that case, the polymeric in nature and functionality independent, arm retraction mode is the faster of the two, while a slower mode, of colloidal nature, emerges that is associated with the structural/cooperative rearrangement of the star-shaped macromolecules. This colloidal behavior in the dynamic behavior of star-shaped polymers, strongly depends on the functionality and become more pronounced with increasing number of arms.[40,41] In the limit of the very large functionality, stars behave like colloids, experiencing topological constrains on the scale of their own size, are trapped and jammed into strong cages and the materials behave as an elastic solid, i.e. do not flow.[40] In other words, as the functionality increases and/or molecular weight of the arm decreases, the cages around the particles evolve from fuzzy and soft to harder and sharper potential wells.

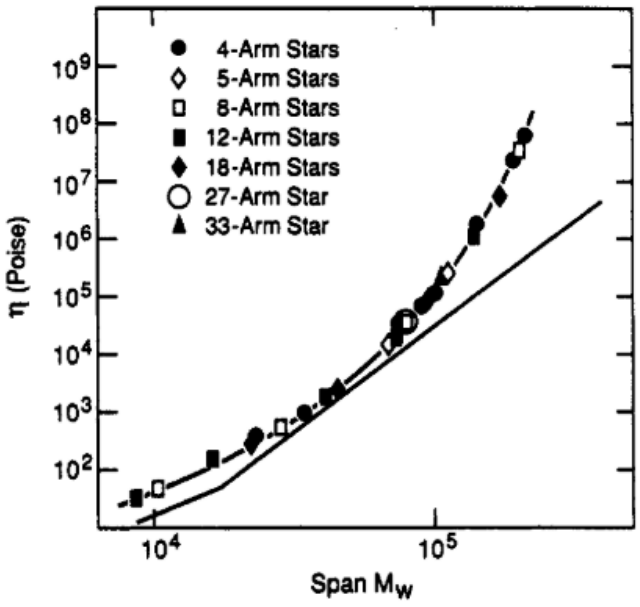

Figure 1.9: Logarithmic plot of the viscosity versus span molecular weight for (Symbols) Star-like molecules with $f \geq 4$ and (solid line) linear polymers. Reprint from Ref.53.[48]

This inherently different diffusion mechanism and the ability for the star to behave as colloid makes such architectures viable candidates for the inherent conductivity-viscosity entanglement when they are comprised from ionically conductive polymers.

1.4.5 Non-Linear PEO based electrolytes

In the literature, it quickly became apparent that a successful solid electrolyte utilizing purely linear PEO doped with salt has certain limitations, seemly impossible to overcome. One approach that has been utilized and to tackle these problems is the modification of the molecular architecture of the polymer matrix. Some of the most common types that have been published are comb-like, star-like and hyper branched polymers as well as crosslinked networks utilizing either solely PEO or copolymers with PEO[50]. Regarding star polymers, they have been reported to act as crystallization inhibitors[51] and also enhance the solubility of salt ($LiClO_4$)[50]. Both of the above observations are crucial for SPE applications and thus such molecules have attracted

lot of attention[52,53,54]. The global effect of architecture on polymer electrolyte performance though is far from being well understood. For start, there are very few works on high functionality regime of star polymers. Due to the largely different mechanism of flow on such systems, improving mechanical properties with architecture while maintaining fast segmental dynamics might be viable in such systems and this would greatly help to overcome the inherent viscosity – conductivity coupling.

1.5 Present Study

In this study, we try to set up the experimental apparatus of impedance/conductivity measurements, to revisit some basics of polymer ionic conduction when measured on our systems that use *poly(ethylene-oxide)* as an ionic conductor and make a brief study of the impact, star polymer architecture can have on the properties of PEO:Salt type electrolytes.

Due to the fact that the ultimate goal for the prepared materials is their potential use as electrolytes for Li-ion batteries, as an ion source for our electrolytes we use the salt Lithium bis(trifluoromethanesulfonyl)imide, commonly known as LiTFSI. This substance is widely used and is considered one of the best candidates for such use due to its high degree of dissociation and the plasticizing effect of the anion[55]. Main characterization of our samples is done by means of Differential Scanning Calorimetry (DSC) and Electrochemical Impedance Spectroscopy (EIS). Electrolytes of various salt concentrations and different polymer matrices were prepared and their measured thermal and electrical properties are presented, compared and contrasted. We simultaneously try to link the observed behaviours with the molecular characteristics of the molecules and extract information helpful for the design of new innovative polymers for electrolyte applications.

2. Materials and Experimental Techniques

2.1 Materials

Table 2.1 summarizes all the polymers used to prepare electrolytes throughout this thesis along with their main characteristics.

Table 2.1: Molecular characteristics of the polymers used in this study

Polymer	M_w (kg/mol)	% wt. PEO	Number of PEO arms
Linear PEO (LPEO-0.55k)	0.55	100	-
Linear PEO (LPEO-1.9k)	1.9	100	-
Linear PEO (LPEO-5k)	5	100	-
Star PEO (S(3)PEO(0.87K))	2.6	100	3
Star PSnPEOn-7k-60k (S(60)PEO(60k))	PEO = 60x60 PS = 60x7 DVB = 170	86% (by NMR)	60

The star polymers utilized in this study were synthesized and characterized by the group of Prof. Sakellariou at the Chemistry Department of the National Kapodistian University of Athens, while the linear poly(ethylene oxides), PEO, were bought and used as received. Briefly, for the synthesis of S(3)PEO(0.87K), a trifunctional initiator was utilized on which 3 arms of PEO were grown to the desired length. The larger star (S(60)PEO(60K)) is a mictoarm star of polystyrene and poly(ethyleneoxide) bearing a divinylbenzene (DVB) core. For its synthesis, the arm first method was utilized where the polystyrene arms are first synthesized using anionic polymerization, then using divinylbenzene (DVB) these arms were crosslinked to a star-shaped molecule having a DVB core with living sites equal to the number of its arms. Finally, from the aforementioned sites, poly(ethyleneoxide) was grown to the desired length.

All polymers used were dried under vacuum and elevated temperature before storing and using in the Argon filled glovebox and other than that, no other purification was carried out. Lithium bis(trifluoromethanesulfonyl)imide, LiTFSI salt

used was dried extensively at 160°C under vacuum before entering the glovebox due to its very hygroscopic nature. Anhydrous Tetrahydrofuran, THF used for blending was bought septum sealed under inert atmosphere and did not go through any drying process.

2.2 Preparation of polymer electrolytes

For the preparation of the electrolytes, the desired amount of the polymer component and lithium bis(trifluromethane) sulfonamide, LiTFSI, were dissolved in dry tetrahydrofuran (THF), stirred until homogeneous and the initially dried at room temperature inside an argon-filled glove box (Mbraun EasyLAB) with sub ppm moisture concentration. The samples were subsequently placed under vacuum at 100°C for another 24 hours within the glove-box. For both EIS and DSC measurements, the cell and the pan respectively were filled and prepared in the glovebox. For EIS the sample was kept constantly under inert atmosphere (see also chapter 4.1) and DSC pans were only exposed to air for less than one minute until loaded in the dry nitrogen atmosphere of the DSC.

2.3 Differential Scanning Calorimetry (DSC)

Differential scanning Calorimetry or DSC is a widely used technique in the field of polymer thermal analysis. The purpose of it is to measure the rate that heat is absorbed or emitted by the sample under test. There are two main types of DSC instruments to achieve this. Heat Flux type and Power compensation type.[56]

The DSC related to this study and generally more commonly used is of the Heat Flux type and thus this is the one that will be further analyzed. In Heat Flux type DSC's, the principle of measurement is that the sample pan is heated in a furnace alongside a reference pan and their temperatures are constantly monitored. If the temperature of the two pans is equal, so is the heat that flows to or from each one of them. In case

their temperature is different, the difference is proportional to the difference in heat flows as dictated by Eq. 2.1:[56]

$$\Phi_m = -k'\Delta T \qquad [Eq.\ 2.1]$$

Where Φ_m is the difference in heat flow measured, k' is a calibration factor and ΔT is the temperature difference measured.

During measurement in a heat-flux DSC, both pans are placed in a furnace (usually made of Silver) on constantan surfaces, with each having a thermocouple (Chromel-constantan) beneath it formed by welding a chromel disc below the constantan platform. These thermocouples are interfaced differentially, obtaining a voltage proportional to the temperature difference of the two samples. After calculating ΔT and taking the k' factor into consideration using a computer, heat flow can be obtained. A schematic of the aforementioned setup is depicted in Figure 2.1 for a disc-type heat flux DSC.[56]

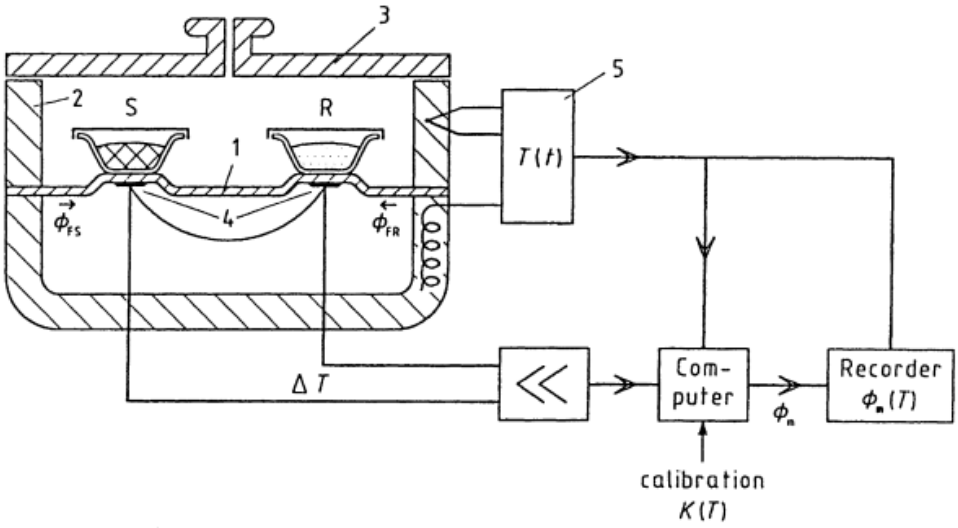

Figure 2.1: Schematic of a disc-type heat-flux DSC apparatus. (1) disc, (2) furnace, (3) lid, (4) differential thermocouples, (5) programmer and controller, (S) Sample pan, (R) Reference pan.[56]

More advanced instruments' cell (turret type) differs slightly from the one pictured in Figure 2.1 as pans are placed on thin walled constantan turrets and also have a third Chromel-constantan in the middle, taking account of the thermal inertia and improving baseline flatness (Tzero™ Technology). The platform and the layout of such cell are depicted in Figure 2.2.

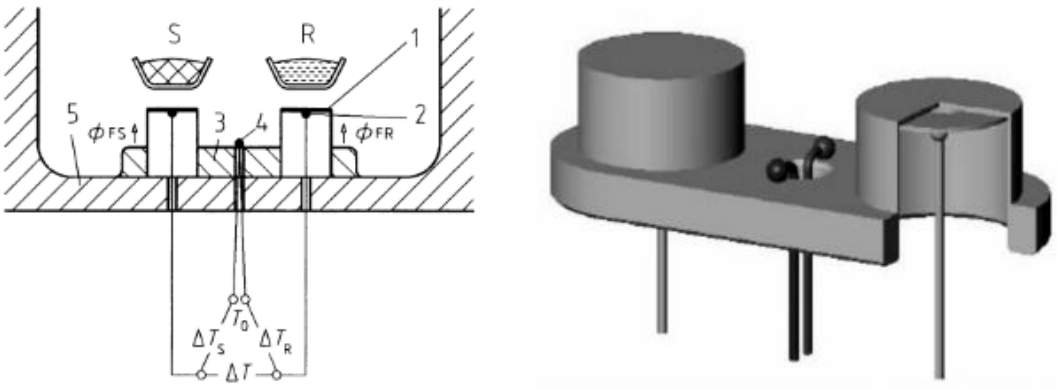

Figure 2.2: Schematic of a turret type heat-flux DSC cell featuring constantan turrets and a third Chromel-Constantan thermocouple (Tzero™ sensor).[57]

The Heat Flow as a function of temperature, or time, during cooling or heating may reveal information on the thermal properties of a material and it has been extensively utilized in polymer science. The main properties can be determined from a DSC experiment are the following:

- Heat capacity of the sample (C_p)
- Melting and crystallization temperature(s) (T_m, T_c)
- Glass transition temperature (T_g)
- Degree of crystallinity (χ_c)

The heat capacity ($J\ K^{-1}\ g^{-1}$) of the sample can be simply obtained by dividing the heat flow (usually *W* (*J/s*) by the mass of sample (*g*) and the heating/cooling rate (*K/s*); the heat capacity reflects the amount of heat needed to increase the temperature of 1 *g* of the material by 1 degree *K* under constant pressure.

During an endothermic event, such as melting, the heat capacity of the sample increases resulting to a heat flow peak (Figure 2.3 left). An exothermic event, such as crystallization has the opposite effect, as the heat capacity of the sample decreases (Figure 2.3 right). Please note that the direction of each peak, i.e. whether the endotherm direction is up or down is defined by the user and does not affect analysis; throughout this thesis we take as negative heat flow the absorption of heat by the sample. Figure 2.3 depicts a typical endothermic event as evidenced in a DSC thermogram. The transition temperature is taken as the most probable value of the peak measured. [58]

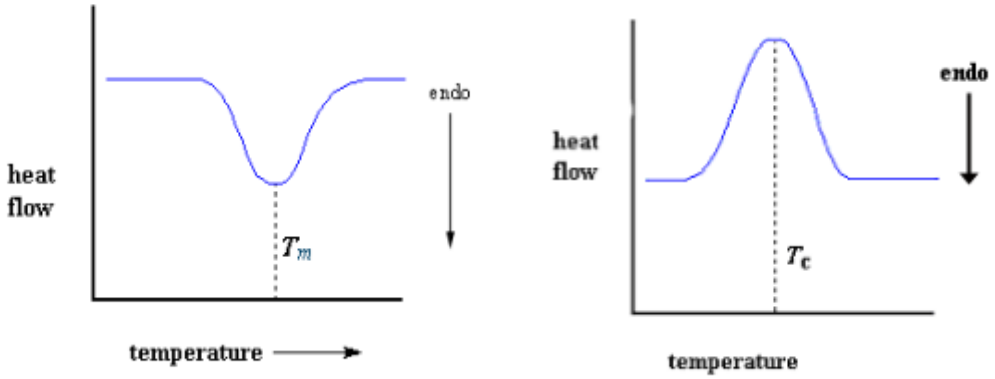

Figure 2.3: (Left) Endothermic event and (Right) Exothermic event as evidenced by DSC indicating the direction of heat absorption as well as the point at which transition temperature is taken.

During these thermodynamic transitions (crystallization or melting) the degree of crystallinity may be calculated. In more detail, if one calculates the area of the melting peak (i.e. the measured enthalpy change during the melting transition, ΔH) and knows the enthalpy change during melting of the corresponding material when 100% crystalized (ΔH_{cryst}), the degree of crystallization (X_c) can be estimated by using equation 2.2:

$$\chi_c = \frac{\Delta H}{\Delta H_{cryst}} \cdot 100\% \qquad [Eq.\,2.2]$$

DSC can also be utilized for the determination of the glass transition temperature (T_g), i.e. the process in which a polymer on heating changes its behavior from a polymer glass, for $T < T_g$, to a polymer melt at $T > T_g$. During glass transition, the heat capacity of the polymer changes, evidenced as a "step" in the heat flow vs temperature plot and the T_g is estimated as the midpoint of that step (Figure 2.4).[58]

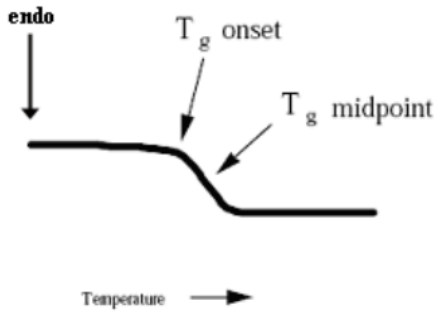

Figure 2.4: Glass transition temperature as evidenced by DSC.

2.4 Electrochemical Impedance Spectroscopy (EIS)

Impedance spectroscopy is a widely used experimental technique to study the electrochemical properties of materials. It's a valuable technique for many research fields regarding batteries[59], fuel cells[60] and photovoltaics[61] and is also commonly used to analyze corrosion[62] and coating[63] processes.

Impedance is the resistance a system presents to the passage of alternating current through it. One of the most fundamental relationships of electronics is Ohm's law. It describes the relationship between the voltage applied to a system of given resistance and the current that passes through it. This law though is valid for DC only and can be written as:

$$V = IR \qquad [Eq\ 2.3]$$

Generalizing this formula to describe the response of a system to AC also requires the introduction of Impedance, Z which is a complex quantity that replaces resistance

when voltage and current are alternating sinusoidal functions of time of constant frequency. The generalized form of Ohm's law for AC can be written as:

$$V(t) = I(t)\, Z \qquad [Eq.2.4]$$

On a linear response system, when an alternating voltage with amplitude V_0 is a applied (Eq. 2.5) the current will also be a sinusoidal function of time (Eq. 2.6) having a phase difference, θ, and an amplitude I_0 dictated by the impedance of the system at that frequency (Eq. 2.6 and Figure 2.5), while $|Z|$ is given by Eq. 2.7. Phase angle, θ indicates how resistive, inductive or capacitive of the system's behaviour is (please note that for an ideal resistor $\theta = 0$).

$$V(t) = V_0 \sin(\omega t) \qquad [Eq.\ 2.5]$$

$$I(t) = I_0\, sin\,(\omega t + \theta) \qquad [Eq.2.6]$$

$$|Z| = \frac{V_0}{I_0} \qquad [Eq.2.7]$$

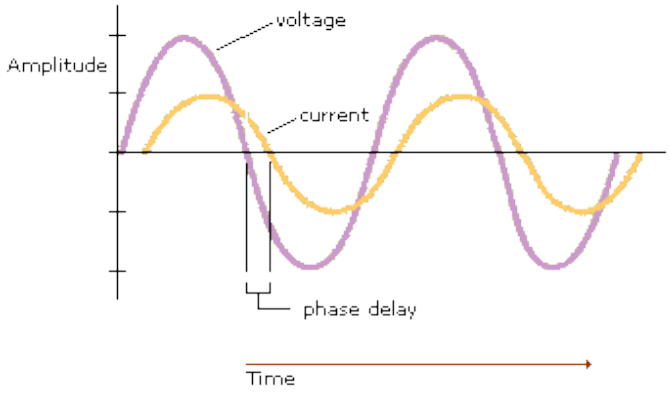

Figure 2.5: Voltage Current relationship of a not purely resistive system, highlighting the phase delay from which ϑ is extracted.[64]

As mentioned earlier, impedance (Z^*) is a complex quantity and thus can be separated into a real, Z', and an imaginary part, Z'' as:

$$Z^* = Z' + jZ" \qquad [Eq\ 2.8]$$

$$Z' = |Z|cos\theta \qquad [Eq.\ 2.9]$$

$$Z" = |Z|sin\theta \qquad [Eq.\ 2.10]$$

Experimentally, electrochemical impedance spectroscopy can be performed with two main methods, PEIS and GEIS. Perturbation in PEIS is voltage applied and the feedback is the current measured while in GEIS, perturbation applied is in the form of current and the potential difference is the feedback.

During a typical PEIS experiment, an alternating voltage is applied to the sample under test, and its frequency is swept through the desired range. Simultaneously, at each frequency the current amplitude and the phase delay between voltage and current are measured. For the results to be reliable, three conditions must be assured. First, that the amplitude of the stimulus signal needs to be small enough in order for the system to behave linearly, but large enough to cause a measurable response; second the system has to be stable and not degrade during the measurements and third the system has to be properly shielded from interferences from the surrounding environment so that the response measured is caused solely by the stimulus signal.

In electrochemical systems, valuable information can be extracted both by the |Z| and θ values, as well as their variation with frequency. To understand and present the obtained results Bode or Nyquist plots are most commonly used (Figure 2.6). The first shows the magnitude of impedance, $|Z|$ and the phase angle θ as a function of frequency, and the latter is a parametric plot of frequency having –Z" on the y axis and Z' on the x axis. In the analysis of electrochemical systems though, Nyquist plots tend to be the most common way of data representation.

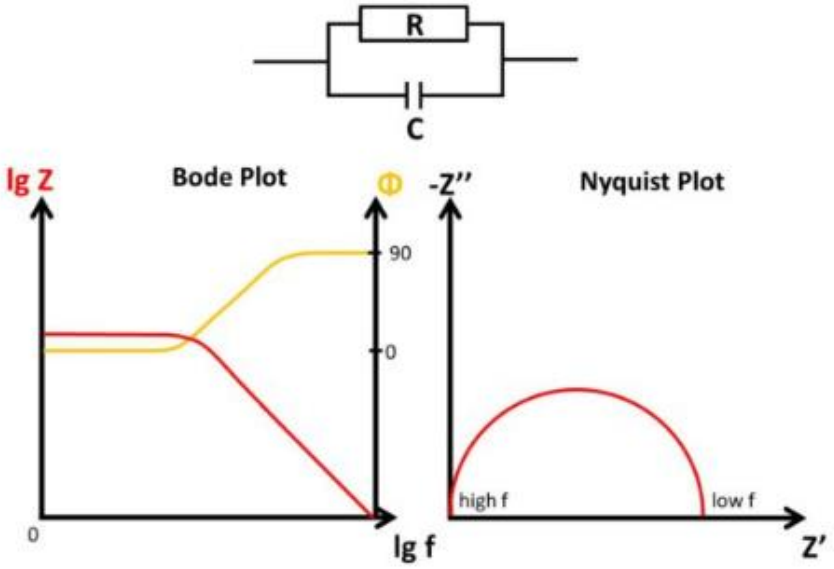

Figure 2.6: (Left) Bode Plot and (Right) Nyquist Plot representation of the impedance of an ideal parallel RC Circuit[65].

Regarding polymer electrolytes, they can be measured either using blocking or non-blocking electrodes. In non-blocking electrode measurements, electron transfer reactions take place between ions and the electrodes while with blocking electrodes there are no such reactions and the system behaves like a capacitor. Non-blocking electrode measurements contain information about the reactions happening and are naturally more complex and difficult to interpret. For the sake of simplicity, blocking electrodes are sometimes preferred to study the electrochemical behaviour of electrolytes.

Typical polymer electrolyte conductivity measurements are carried out using PEIS. In the case of blocking electrode measurements the electrolyte is kept in a cell of known volume, sandwiched between chemically inert electrodes, typically made of Stainless steel, Brass, Platinum etc. The assembly is measured using an impedance analyzer and the observed response is most commonly presented through the Nyquist plot. Typical Nyquist plots of such systems depict a semi circle followed by a tilted line as seen in Figure 2.7. From such measurement, bulk resistance, R_{bulk} of the electrolyte under test can be extracted as the value of Z' at the point where the data intercepts

the real axis after the semi-circle. From R_{bulk}, the D.C. conductivity, σ_{dc} of the electrolyte can be calculated using Equation 2.11.

$$\sigma_{dc} = \frac{H}{R_{Bulk}A} \qquad [Eq.2.11]$$

Where H is the thickness of the electrolyte and A is the electrode-electrolyte interfacial area.

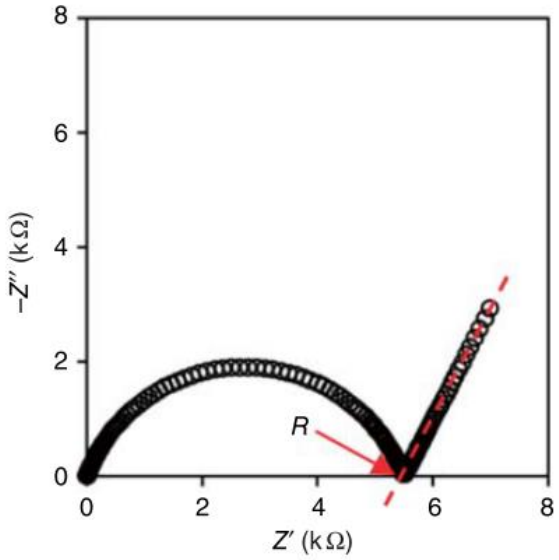

Figure 2.7 : Typical Nyquist plot of blocking electrode - polymer electrolyte EIS measurement indicating the point taken as R_{bulk} (red arrow) [Reprint from Ref.66].[66]

3.Thermal Characterization of PEO:LiTFSI electrolytes

3.1 Differential Scanning Calorimetry (DSC)

DSC was used to measure the thermal properties of the PEO-based electrolytes. The samples were subjected to two heating-cooling runs. First, each sample was heated up to 150°C and annealed for a minimum of 5 min to erase its thermal history. The sample was then cooled to -110°C at a cooling rate of 10°C/min, and subsequently heated to 150°C at a heating rate of 10°C/min. The reproducibility of the data was tested with an extra cooling/heating cycle and the data appeared identical.

Figure 3.1 shows the DSC traces of polymer electrolytes prepared by blending linear poly(ethylene oxide), PEO, with molecular weight M_w = 5 kg/mol (LPEO-5K) and lithium bis(trifluoromethane)sulfonamide (LiTFSI), at various molar ratios r = [Li^+] / [EO]. The DSC traces in Figure 3.1a represent the coolings after annealing at 150 °C, while Figure 3.2b are the subsequent heating runs; both cooling and heating were performed at a rate of 10°C /min. Three features are distinct on the thermograms for LPEO-5K:LiTFSI samples with $r \leq 0.07$: (1) an exothermic peak during cooling that corresponds to the crystallization of PEO (Figure 3.1a), (2) an endothermic melting event during heating (Figure 3.1b), and (3) end endothermic step (in both cooling and heating), at temperatures below melting, that corresponds to the glass transition temperature, T_g^{PEO}, of the amorphous LPEO-5K.

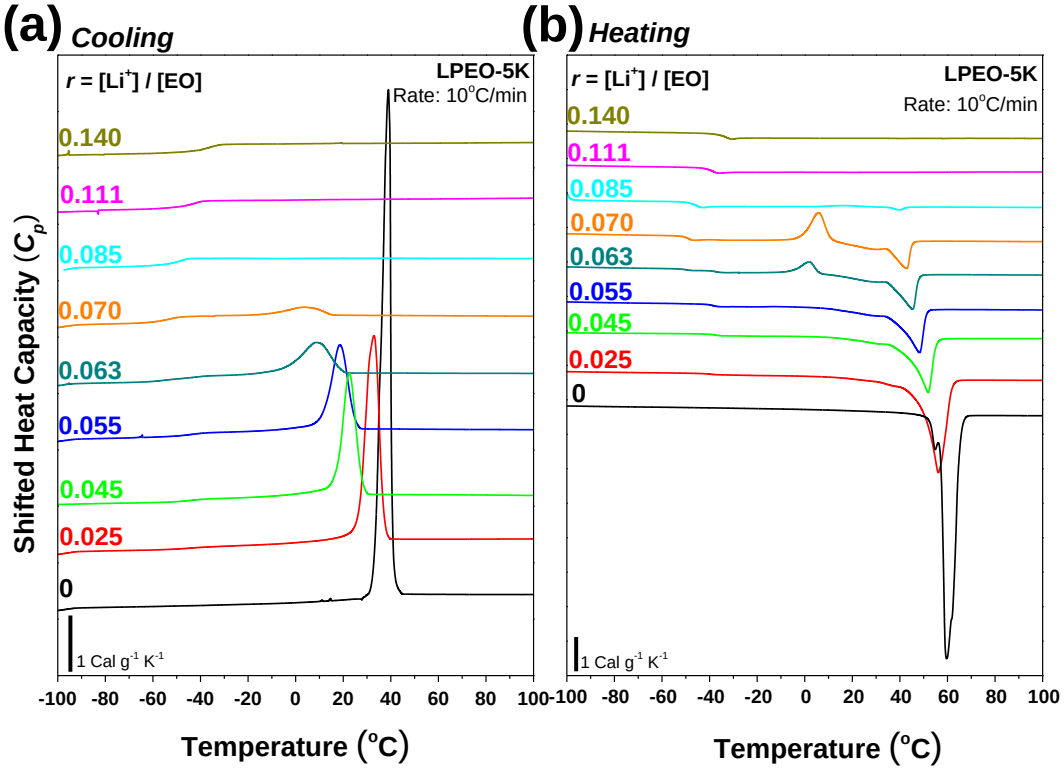

Figure 3.1: DSC traces of the polymer electrolytes LPEO-5K:LiTFSI with r = [Li$^+$]/[EO] ranging from 0.025 to 0.140 , on cooling (a) and subsequent heating (b) at a rate of 10 °C /min.

The degree of crystallinity (X_c) was calculated as X_c (%) = ($\Delta H_{exp}/\Delta H_{cryst}$)*100%, where ΔH_{exp} is the measured enthalpy change during the melting, normalized to the PEO weight fraction of the sample (i.e. the area of the endothermic event during heating divided by PEO fraction, see also Chapter 2.2.2), and ΔH_{cryst} is the theoretical heat of fusion of the 100% crystalline PEO and is taken equal to 196.4 *J/g*[67]. The X_c as a function of r = [Li$^+$] / [EO] is plotted in Figure 3.2a. Due to the interactions of the EO segments of the PEO and the L_i^+ of the LiTFSI salt, X_c monotonically decreases with r, while the PEO crystallization is completely suppressed for $r \geq 0.085$, leaving the polymer electrolyte in an amorphous state (blue regime in Figure 3.2a). Notably, for r = 0.063 and 0.073, i.e. close to the concentration at which the material remained amorphous, the samples remained amorphous during the cooling while crystallize during heating; seen as a cold crystallization exotherm on heating runs. This implies that salt alters / obstructs the kinetics of crystallization. At the same time, both the

crystallization and the melting temperatures (T_c and T_m, respectively) decrease monotonically with r. Last but not least, and as it will be discussed next, a significant increase in the T_g^{PEO} with r is observed.

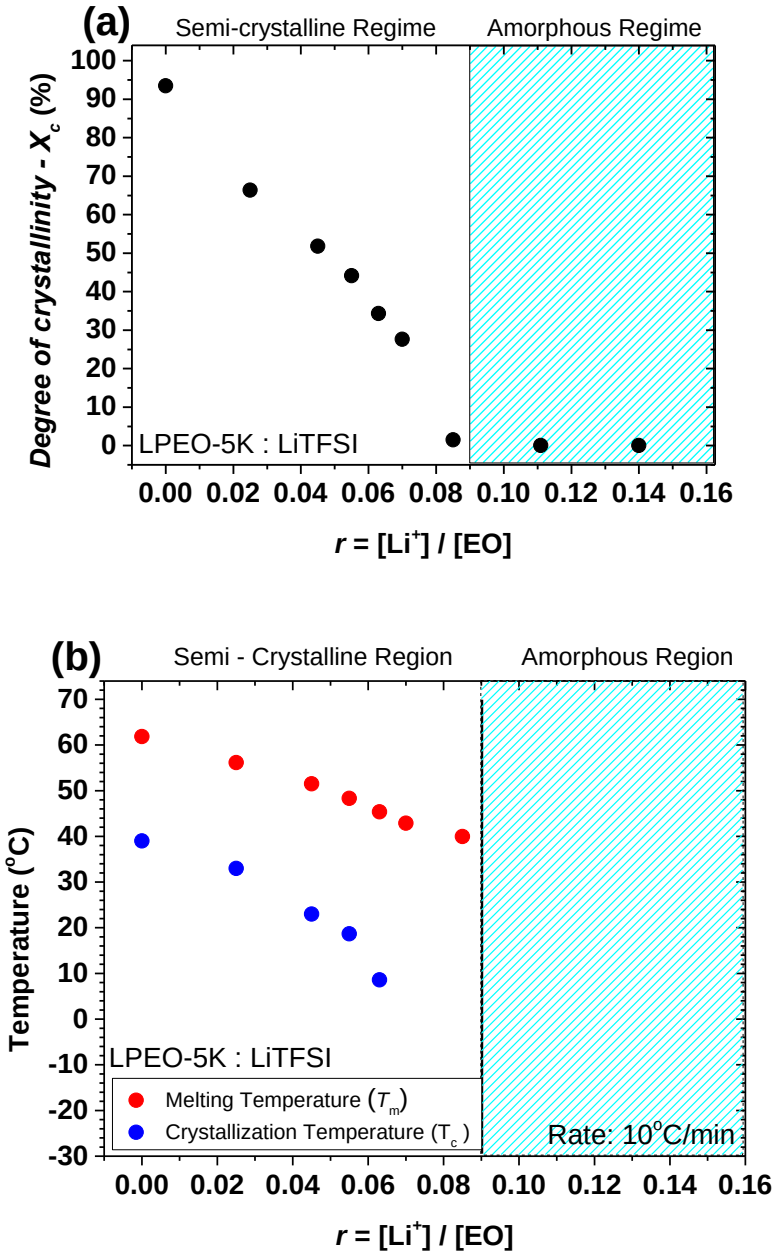

Figure 3.2: (a) Degree of crystallinity and (b) melting (red circles) and crystallization temperatures (blue circles) as a function of r = [Li$^+$] / [EO] of LPEO-5K:LiTFSI polymer electrolytes.

Figure 3.3 shows the heating trace after the LPEO-5K with r = 0.055 from 150 ^{o}C to -110 ^{o}C at a cooling rate of 10 ^{o}C /min, the so-called "normal scan" with blue line, along with the corresponding heating trace after the sample was quenched to -110^{o}C at a cooling rate of 65 ^{o}C /min (the fastest rate that could be achieved with the DSC set-up used). The latter cooling rate was large enough so the sample remained amorphous at -110 ^{o}C; no crystallization was observed during cooling and a large cold crystallization was seen during heating. Notably, the measured T_g^{PEO} for the quenched / amorphous sample is about 14^{o}C higher than the corresponding T_g^{PEO} of the semi-crystalized PEO electrolyte (T_g^{PEO} = - 53 ^{o}C and -39 ^{o}C, respectively). This can be explained by the fact that when in the semi-crystalline phase the concentration of LiTFSI is the amorphous PEO phase is higher than what is dictated by the *r*; the growing lamellae during crystallization expel LiTFSI which resides with the amorphous phase.[23] The situation described is not present in the quenched /amorphous PEO electrolyte where the whole PEO volume of the electrolyte is in the amorphous state. A direct consequence is the significant differences in the C_p change at the glass transition (ΔC_p); for the amorphous ΔC_p = 0.15 cal g^{-1} K^{-1} while for the semicrystalline ΔC_p =0.08 cal g^{-1} K^{-1}, a quantity directly proportional to the fraction of the sample going through glass transition. It is also important to point out that the melting temperature and degree of crystallinity appears to be unaffected by the thermal history of the sample.

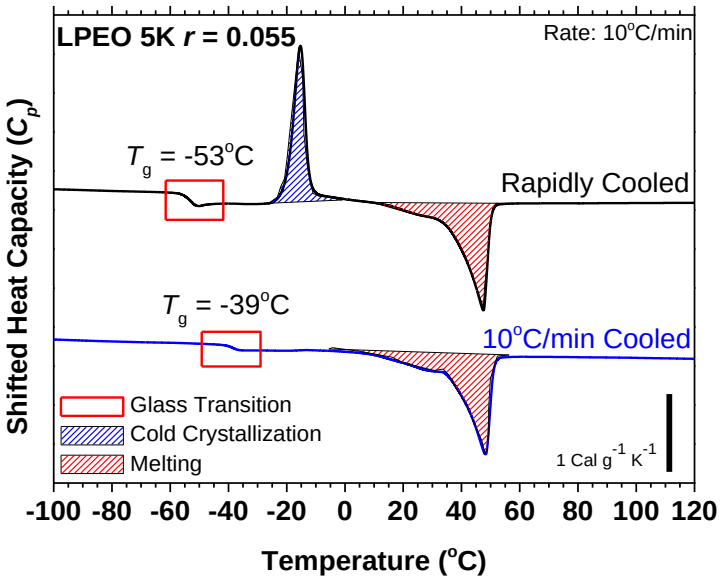

Figure 3.3: DSC traces during heating for LPEO-5K:LITFSI with r = 0.055 after a normal cooling at 10 °C/min (Blue trace) and after quenching (Black trace)

Figure 3.4 shows the T_g^{PEO} of the LPEO-5K:LiTFSI electrolytes as a function of *r*; the black solid symbols refer to the T_g^{PEO} for the samples that were cooled to -110°C at 10 °C /min (normal scan), while the open black symbols correspond to the T_g for the samples that were quenched to -110°C at 65°C/min (amorphous state). It is important to point out that for the LPEO-5K:LiTFSI electrolyte with *r* = 0.025, a quenched amorphous electrolyte could not be achieved even at 65°C /min, i.e. the fastest available with our current DSC set-up, and an exothermic crystallization peak during cooling was measured. It is clear that the T_g^{PEO} of the amorphous polymer electrolytes scales linearly with r, consistent with the literature.[68] In contrast, for the polymer electrolytes cooled at 10°C /min to -110°C, a discontinuity is observed at a critical $r > 0.07$, i.e. the critical *r* that the PEO:LiTFSI electrolytes are amorphous and thus no LiTFSI concentration variations due to crystallization are expected. It is important to point out that for the remaining of this work, the T_g^{PEO} values reported correspond to the samples that were successfully quenched to a fully amorphous state.

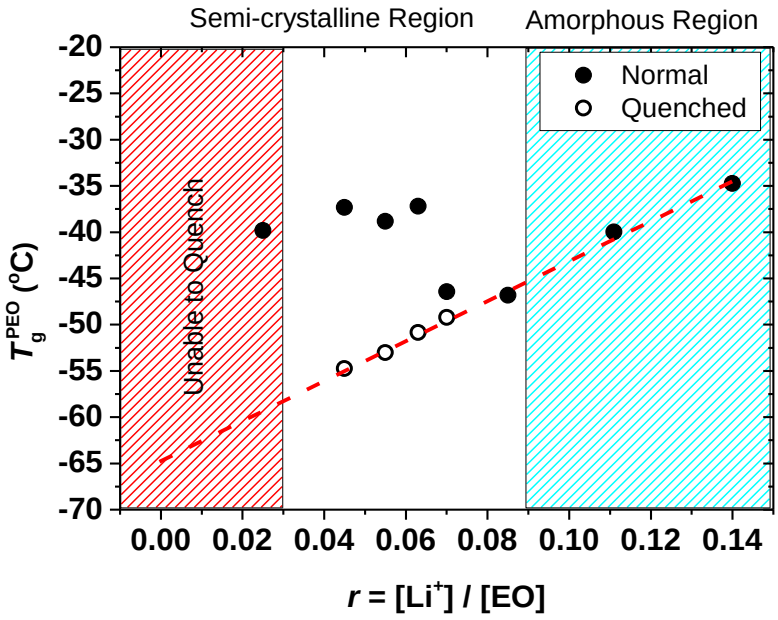

Figure 3.4: Glass transition temperatures for LPEO-5K:LiTFSI electrolytes for quenched (open symbols) and "normally" cooled samples at 10 C/min (solid symbols). Dashed line is a guide to the eye highlighting the linear relationship.

3.2 The Effect of PEO's molecular weight on the Thermal Properties of PEO:LiTFSI blends

In this section, the effect of the molecular weight of linear PEO:LiTFSI electrolytes is studied. Three different linear PEO were considered (Table 2.1) : one with M_w = 0.55 kg/mol (i.e. smaller than the entanglement M_w for PEO, M_e = 2 kg/mol) [26], one with M_w=1.9 kg/mol (LPEO-1.9K), i.e. around the entanglement molecular weight for PEO, and one with M_w=5 kg/mol (LPEO-5K). All three polymers were blended with LiTFSI salt at various r = [Li^+] / [EO] ratios and their thermal properties were studied with DSC. The cooling/heating traces for the LPEO-0.55K and LPEO-1.9K at various r are shown in Figure 3.5.

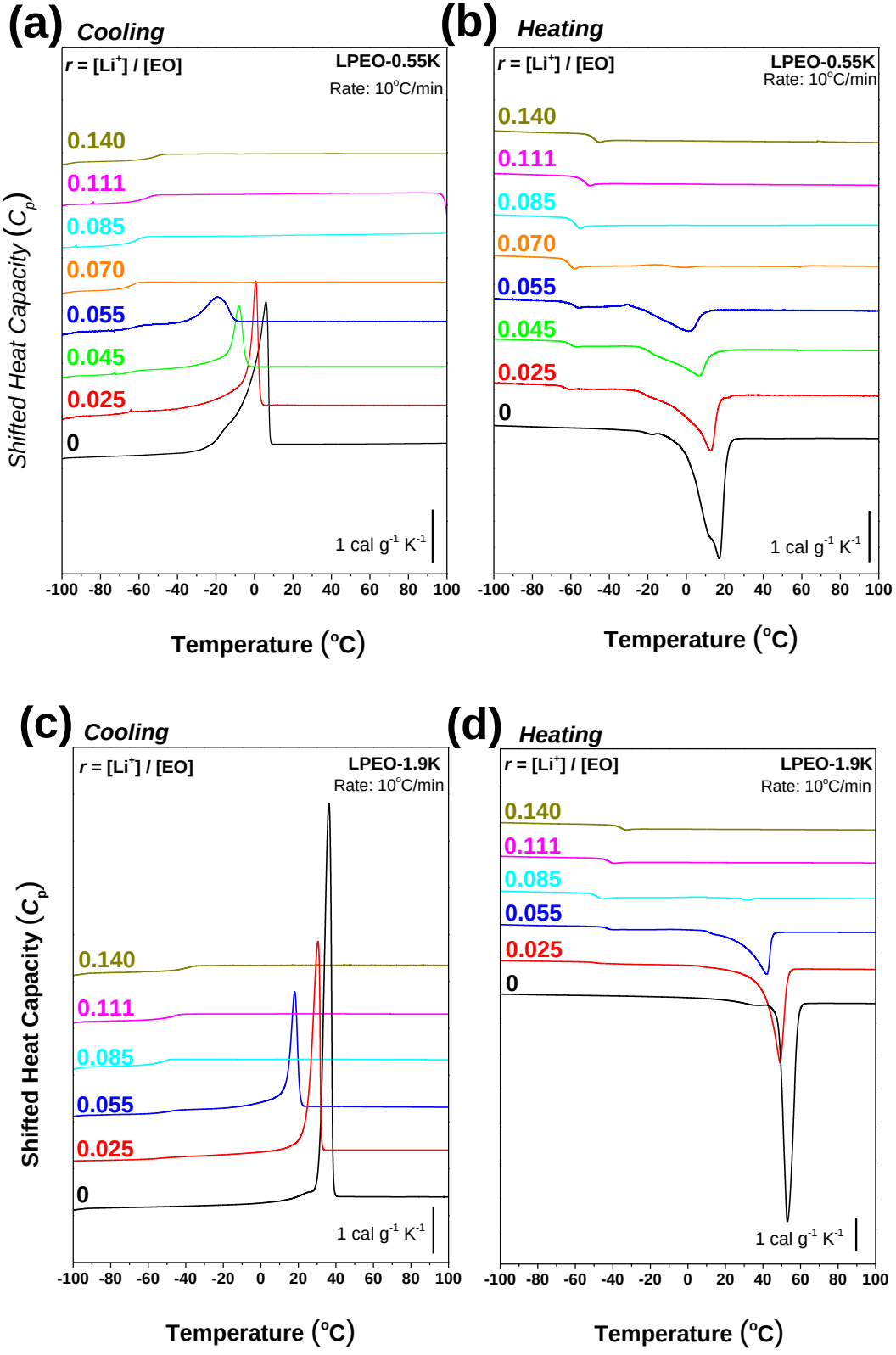

Figure 3.5: DSC traces of (a, c) Cooling and (b, d) Heating runs of (a, b) LPEO-0.55K:LiTFSI and (c, d) LPEO-1.9K:LiTFSI with $r = [Li^+] / [EO]$ ranging from 0.025 to 0.140 with a rate of 10 °C /min.

As in the case of the LPEO-5K:LiTFSI electrolytes, the addition of LiTFSI salt leads to the decrease of the degree of crystallinity. At the same time a shift to lower temperatures of T_m, T_c, and T_g is observed with increasing r. Again, for a critical value of r, no crystallization is observed and the PEO:LiTFSI blends are in the amorphous state. In order to understand the effect of M_w on the thermal properties of linear PEO:LiTFSI electrolytes, in Figures 3.6 and 3.7 the X_c, T_m and T_c are plotted as a function of r for the different LPEO considered in the current work.

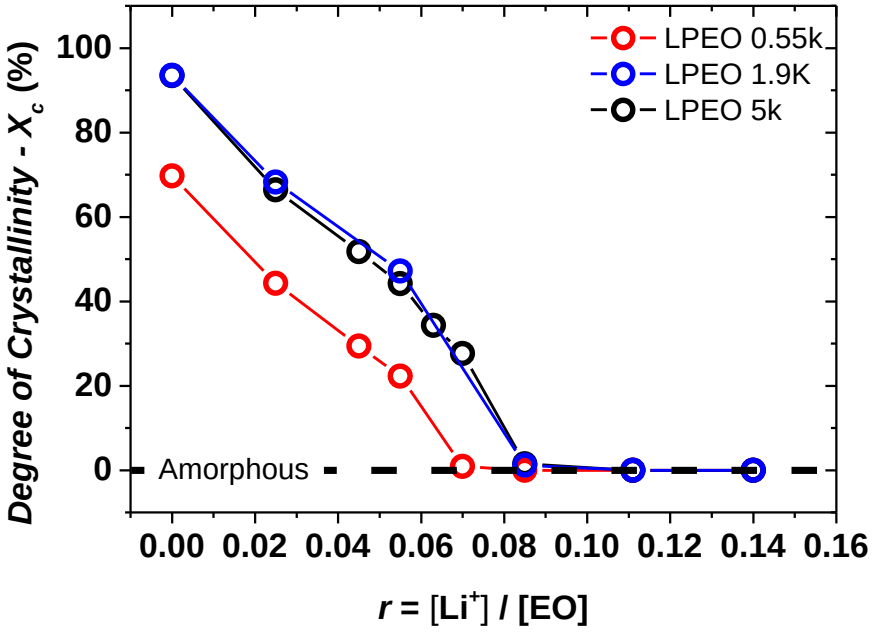

Figure 3.6: Effect of r = [Li$^+$] / [EO] and the M_w of linear PEO on (a) the degree of crystallinity (X_c) of LPEO:LiTFSI electrolytes.

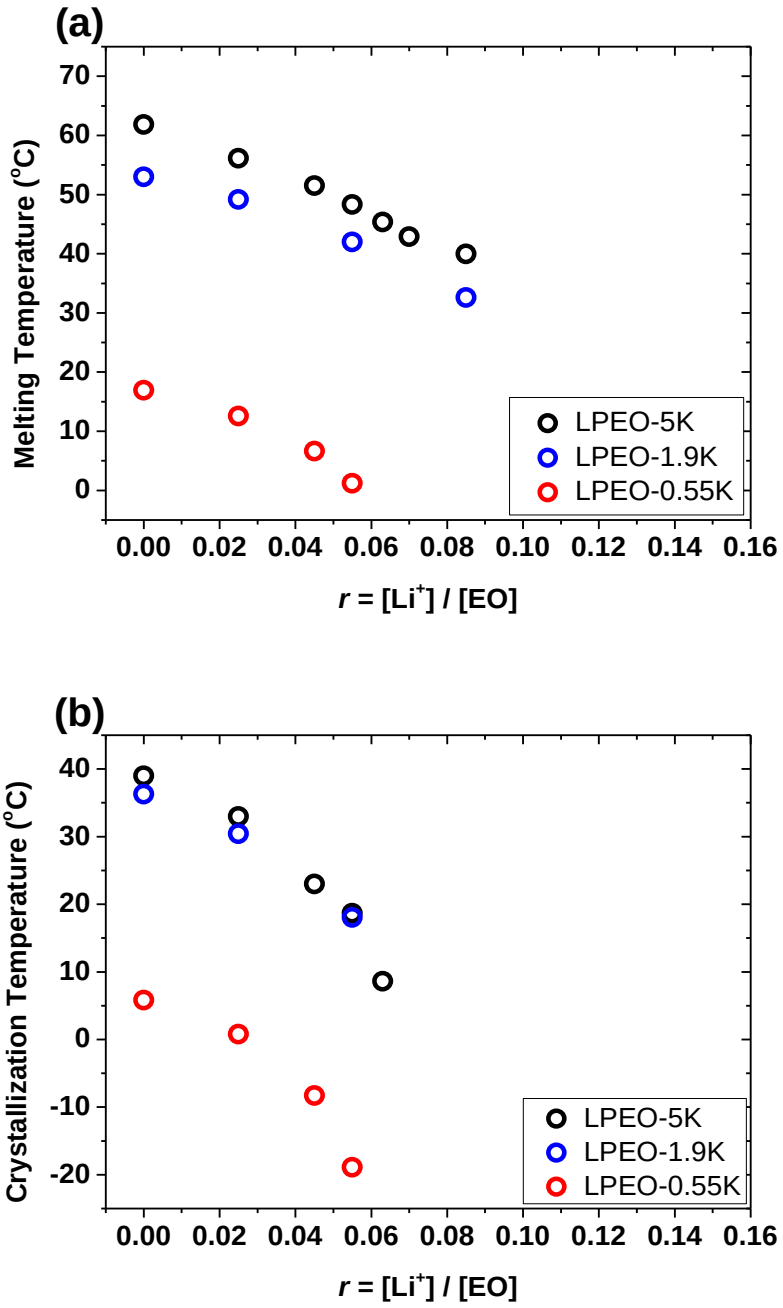

Figure 3.7: Effect of linear PEO's M_w on (a) the melting and (b) the crystallization temperatures of LPEO:LiTFSI polymer electrolytes as a function of r = [Li^+] / [EO] ratio.

Figure 3.6 reveals that the X_c of LPEO-1.9K and LPEO-5K are similar at r = 0 and decreases in the same manner/rate with r. In the case of LPEO-0.55K:LiTFSI electrolytes the X_c is systematically lower compared to that of the larger PEO molecules at all r , something known also for the pristine case.. This could be explained due to the fact that LPEO-0.55K has more free ends. It is important to point out that

X_c in the case of LPEO-0.55K is being suppressed in a similar manner/rate with r as in the case of longer PEO chains showing that the effect of LiTFSI is very similar to all three molecules.

Figure 3.8a, shows the T_g^{PEO} as a function of r, for various M_w of PEO. A sample of LPEO-10K with r = 0.085 was prepared and its T_g^{PEO} is plotted along with the corresponding T_g of LPEO-0.55K, LPEO-1.9K and LPEO-5K. It is clear that the T_g of PEO appears to be independent on the M_w for $M_w \geq 5$ kg/mol. This may be seen also in figure 3.8b, where the T_g of LPEO:LiTFSI electrolytes at r = 0.085 is plotted as a function of M_w. To this end, it is known that the T_g of polymers has a very weak dependence with the M_w for $M_w > M_e$ and our data indicate that this is the case also for the LPEO:LiTFSI electrolytes.

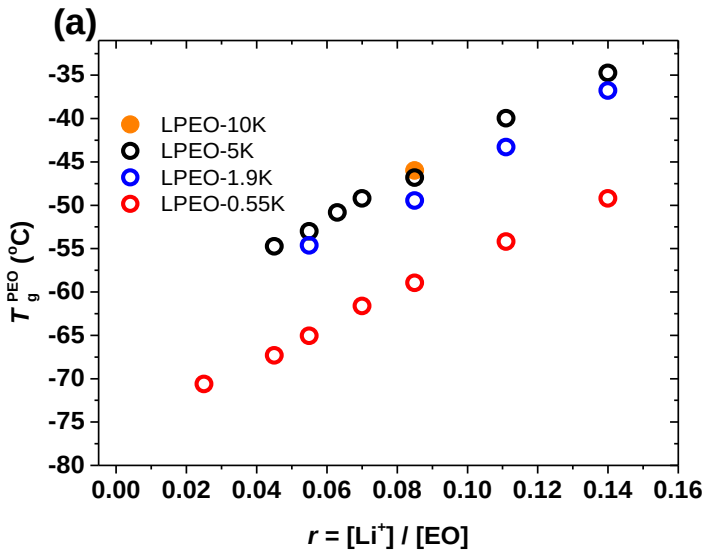

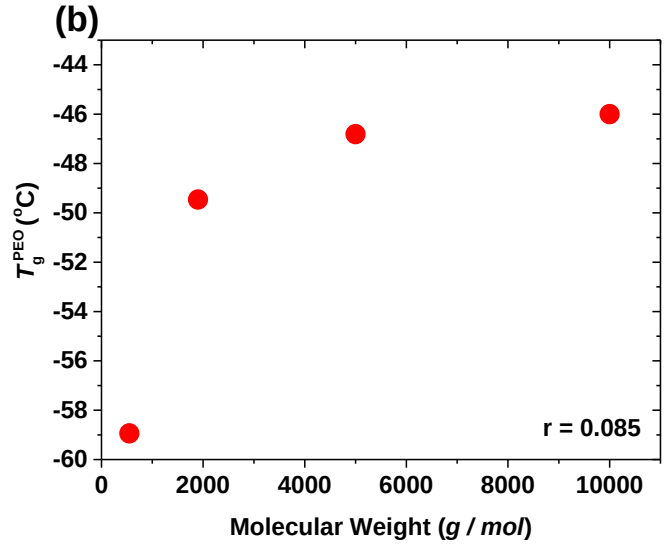

Figure 3.8*:* (a) Effect molecular weight of linear PEO on the glass transition temperatures of PEO in LPEO:LiTFSI polymer electrolytes as a function of r = [Li^+] / [EO]. One LPEO-10K:LiTFSI sample (*r = 0.085)* is also included to support that M_w dependence reaches a plateau. (b) Dependence of T_g on PEO's M_w for r = 0.085 clearly showing the reduced dependence on high M_w.

3.3 The effect of star-shaped architecture on the thermal properties of PEO:LITFSI blends

We now turn our attention on the effect of macromolecular architecture of PEO, and in particular that of star architecture, on the thermal properties of PEO-based:LiTFSI electrolytes. To do so, two different star-shaped PEO were considered (Table 2.1): (1) a three arm (f = 3) star PEO with arm molecular weight M_w^{arm} = 0.87kg/mol (i.e. S(3)PEO(0.87K)) and (b), a high fucntionality PS_nPEO_n mictoarm star with a DVB core mol (i.e. S(60)PEO(60K)). This star has n polyethyleneoxide and n polystyrene arms. Based on NMR, it is consisted from 86% PEO and n is about 60. Each PEO and PS arm has approximately M_w^{arm} = 60 kg/ and 7 kg/mol respectively. The star-shaped polymers were blended with LiTFSI at different molar ratios r and their thermal properties were studied.Figure 3.9 shows the DSC runs during coolings (a and c), and during heating (b and d) for the S(3)PEO(0.87K) and S(60)PEO(60K), of the

electrolytes prepared after blending the star-shaped PEO molecules with LiTFSI in various molar ratios, *r*.

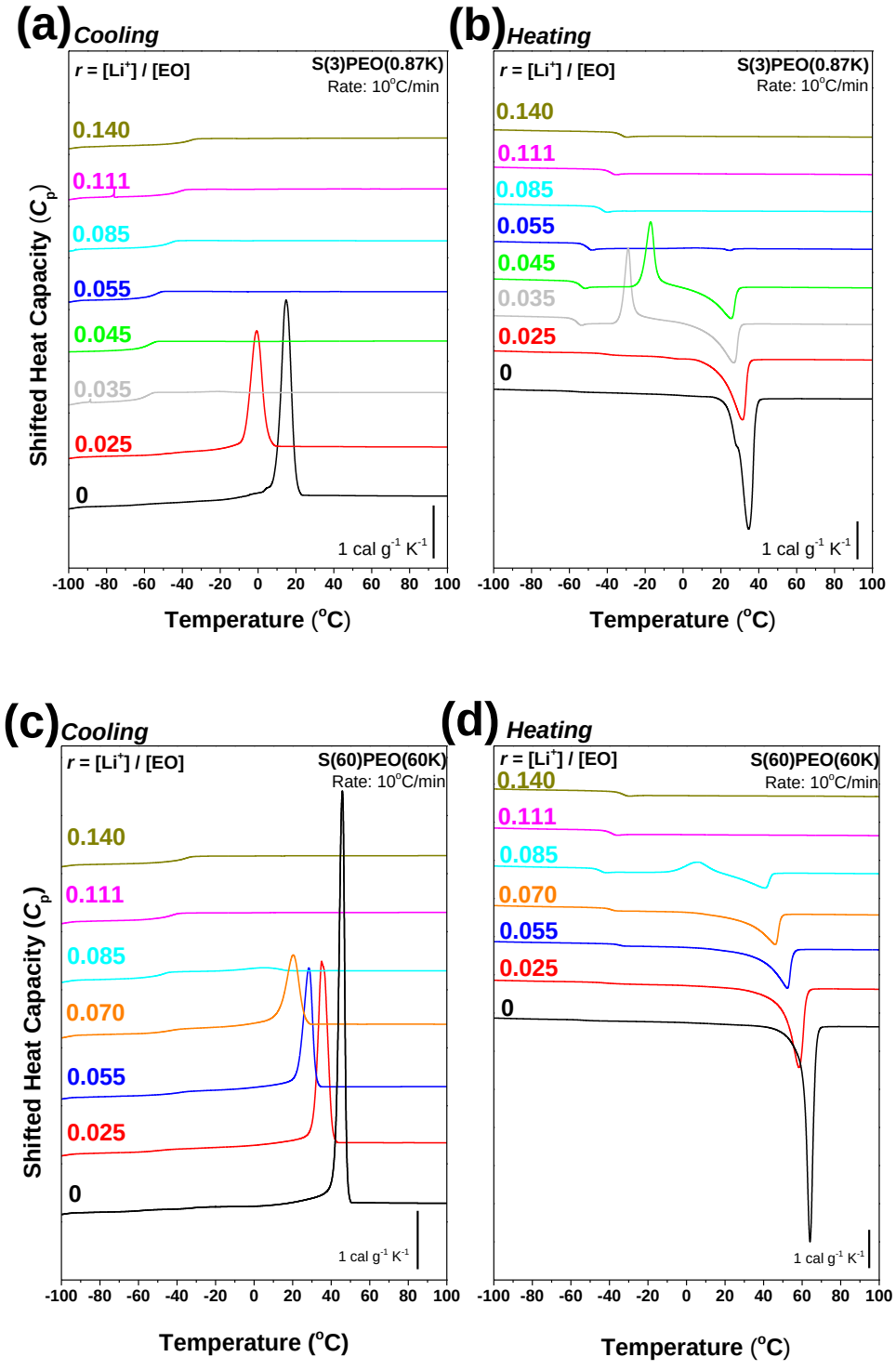

Figure 3.9: DSC traces of (a, c) Cooling and (b, d) Heating runs of (a, b) S(3)PEO(0.87K):LiTFSI and (c, d) S(60)PEO(60K):LiTFSI polymer electrolytes with $r = [Li^+] / [EO]$ ranging from 0.025 to 0.140 with a rate of 10°C /min.

In Figures 3.10, 3.11 and 3.12 below, the results from the thermal analysis of the star PEO based electrolytes are compared with the previous results for linear PEO.

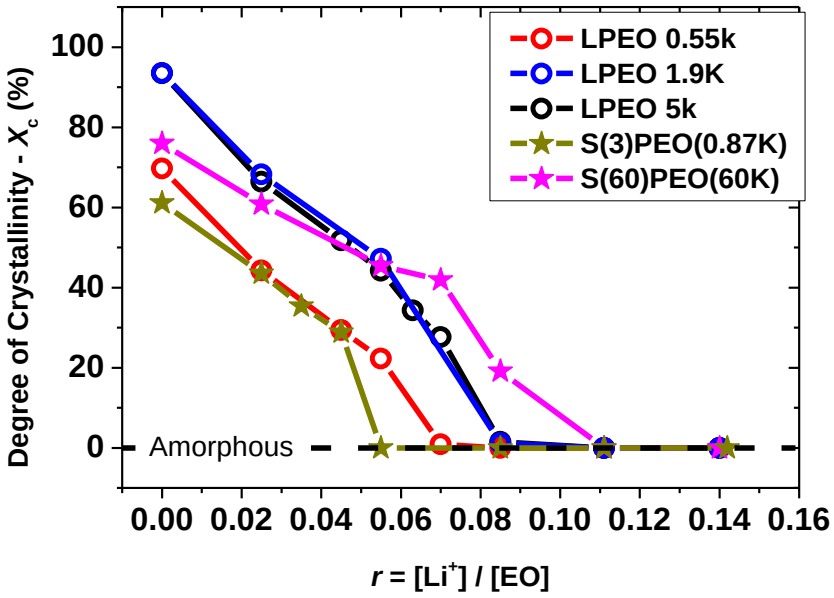

Figure 3.10: Effect of PEO molecular weight and architecture on the Degree of Crystallinity as a function of r = [Li$^+$] / [EO].

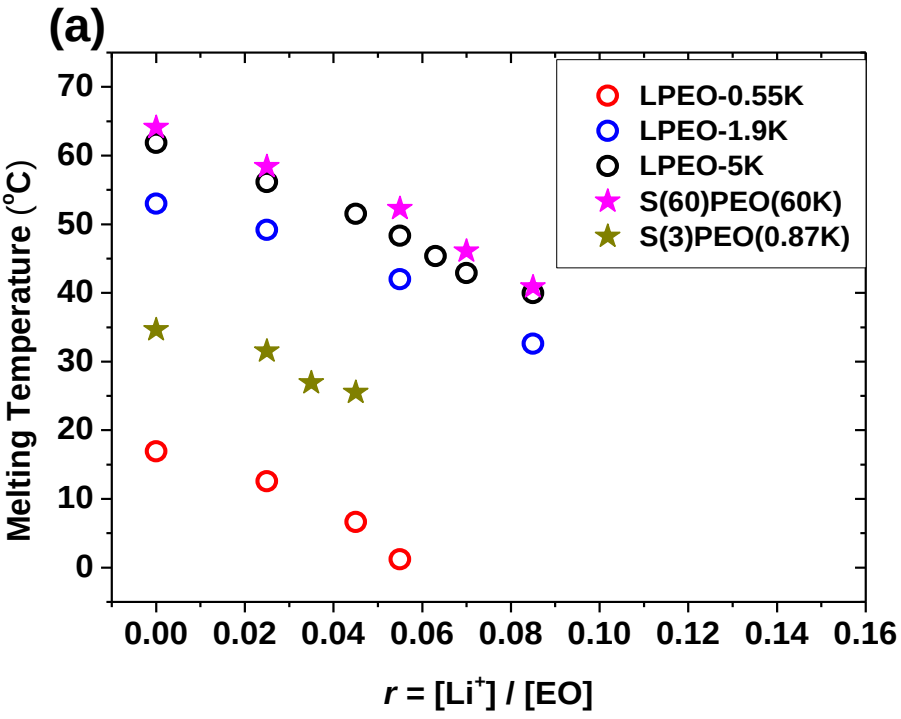

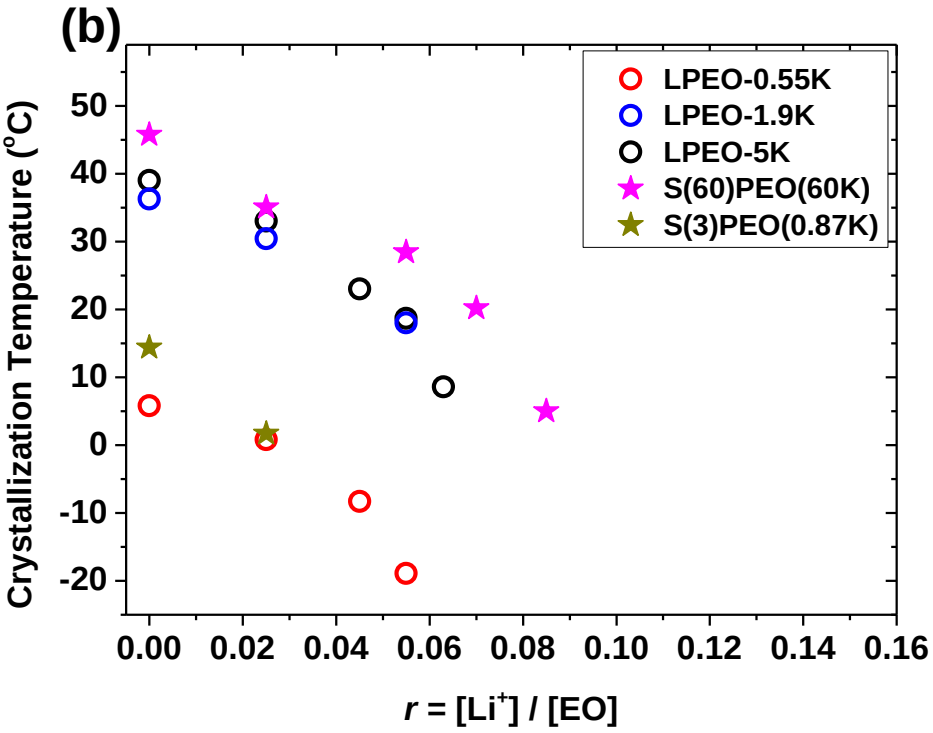

Figure 3.11: Effect of PEO molecular weight and architecture on (a) Melting and (b) Crystallization temperature as a function of r = [Li^+] / [EO].

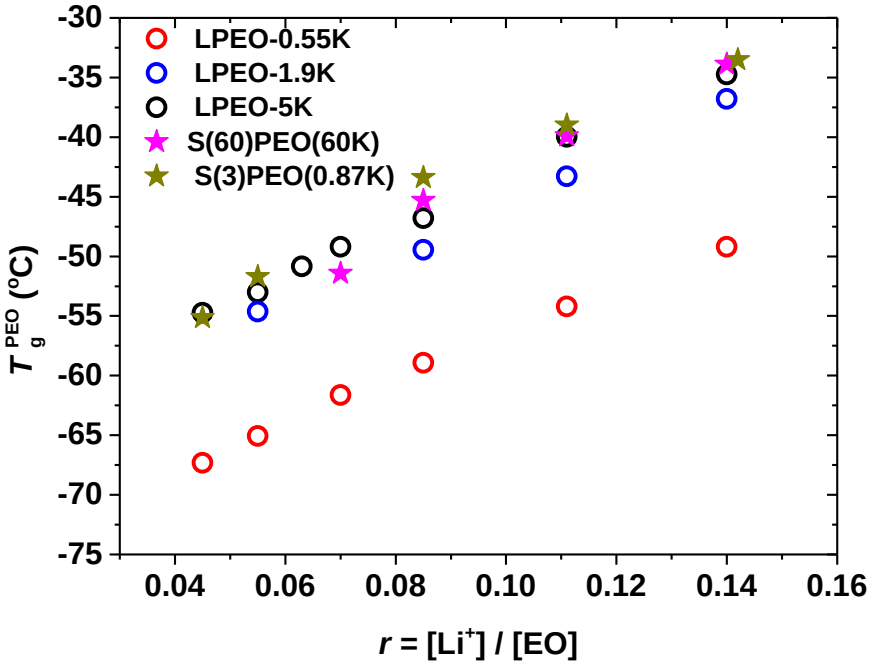

Figure 3.12*:* Effect of molecular weight and architecture on the glass transition temperatures for PEO:LiTFSI electrolytes as a function of r = [Li^+] / [EO].

Regarding the degree of crystallinity of the pristine PEO-based polymers (i.e. for r = 0), S(3)PEO(0.87K) due to branching and associated geometrical constrains has significantly smaller crystallinity than the corresponding linear PEO analogues with similar M_w as its arm (LPEO-1.9K) or with similar total M_w (LPEO-5K). Interestingly S(60)PEO(60K) has a larger degree of crystallinity than that of the 3-arm star PEO with 0.87K per arm and the oligomeric LPEO-0.55k, yet smaller than that of the LPEO-1.9K and LPEO-5K. When LiTFSI is added, the depedence of X_c of S(60)PEO(60K) on r seems to be weaker than any other molecule (Figure 3.11); it's the only macromolecule that still crystallized at r = 0.085. The above phenomenon implies that its architecture and its high functionality in particular, affects the interaction of PEO with LiTFSI and consequently reduces the effect that the latter has on the crystallization of the polymer. Notably, S(3)PEO(0.87K) has both melting and crystallization temperatures lower than the corresponding linear PEO molecule with comparable total molecular weight (Figure 3.10). Regardless of the lower melting and crystallization temperatures, both stars seem to have glass transition temperatures close to the highest molecular weight PEO considered here and with a very similar r depedence.

4.Electrical Characterization of PEO:LiTFSI electrolytes

4.1 Design and Assembly of a Custom Made Chamber for Electrical Characterization of Polymer Electrolytes under Controlled Temperature and Atmosphere

For the electrical characterization at a control atmosphere and temperature of the polymer electrolytes under investigation in this study, initially an environmental chamber and a conductivity cell was designed, manufactured, optimized and evaluated. A temperature controller was also designed and implemented in the home-made/custom-made set up.

4.1.1 Conductivity Cell for impedance measurements in liquid and solid electrolytes.

As several polymer electrolytes in this study were liquid-like for certain temperature ranges, a cell that would keep the fluid in well-known dimensions at different temperatures was designed for the ionic conductivity measurements. CAD views of the cell, as well a photograph of the final cell can be seen in Figure 4.1. The cell was made from brass electrodes (parts 1 and 5 in Figure 4.1), with a PTFE spacer (part 2 in Figure 4.1) to maintain a constant distance between the electrodes. PTFE spacers with various sample areas with diameters of 4, 6, and 8 mm and thicknesses of 1 and 2 mm (part 3 in Figure 4.1) were designed and used and notably, no effect of sample dimensions on conductivity measurements was observed. PTFE isolators (parts 4 in Figure 4.1) were introduced in the cell in order to ensure the electrical isolation

of the electrodes. The assembly processes and the corresponding steps may be seen in Figures 4.1 A, B, C and D. Cables were soldered on each electrode for the electrical interfacing of the cell with the impedance analyzer (red and green cable in Figure 4.1 E).

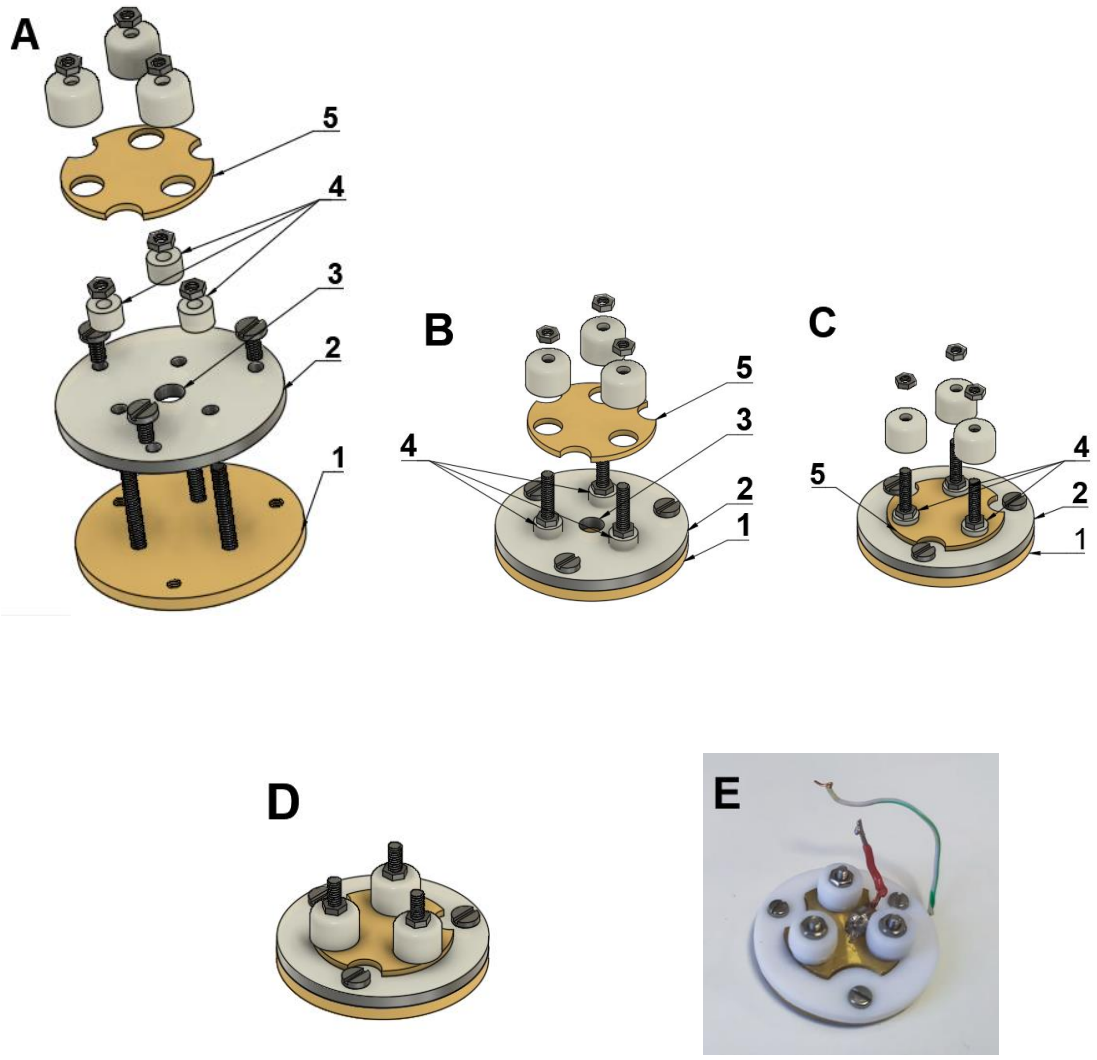

Figure 4.1: (A-D) CAD representations of conductivity cell showing its main components. (A) Full exploded, (B,C) Halfway assembled views (D) Full assembled view, (E) Photograph of assembled cell. The features highlighted are: (1) Bottom electrode, (2) PTFE Spacer, (3) Sample Area, (4) PTFE Isolation Rings, (5) Top Electrode.

4.1.2 Environmental Chamber for EIS measurements at various temperatures

PEO and LiTFSI salt are extremely hygroscopic and their - even short - exposure to ambient conditions may lead to moisture absorption that affects the ion conductivity measurements. Therefore, the PEO:LiTFSI electrolytes were exclusively prepared in an Argon filled glovebox with sub ppm moisture concentration. To ensure that the electrical conductivity measurements would be performed in an inert environment, an environmental, airtight, chamber was designed that was assembled in the glove box. More precisely, the chamber is made out of a metal cylinder and a lid, held together with bolts and an 'O'-ring to make the assembly airtight. On the lid there is a custom made 8 cable feed-through based on KF vacuum components. A pressure gauge and a valve were fitted to the chamber and then several tests were conducted to ensure that the chamber could both maintain a vacuum or elevated pressure. Inside the home made chamber, a PTFE platform was designed to hold the cell described above. The design was made such that the sample cell to be electrically isolated from its surroundings while placed in the middle of the chamber volume to avoid possible temperature gradients or electrical interferences. To record the exact temperature of the cell during measurements, a PT100 sensor was placed in contact with the bottom electrode of the cell. As PT100 is a Resistance Temperature Detector (RTD), a three wire configuration was utilized that accounts for the resistance of the cables as well as its dependence on temperature. The whole environmental chamber was wrapped with a heating tape, making it a controlled temperature oven.

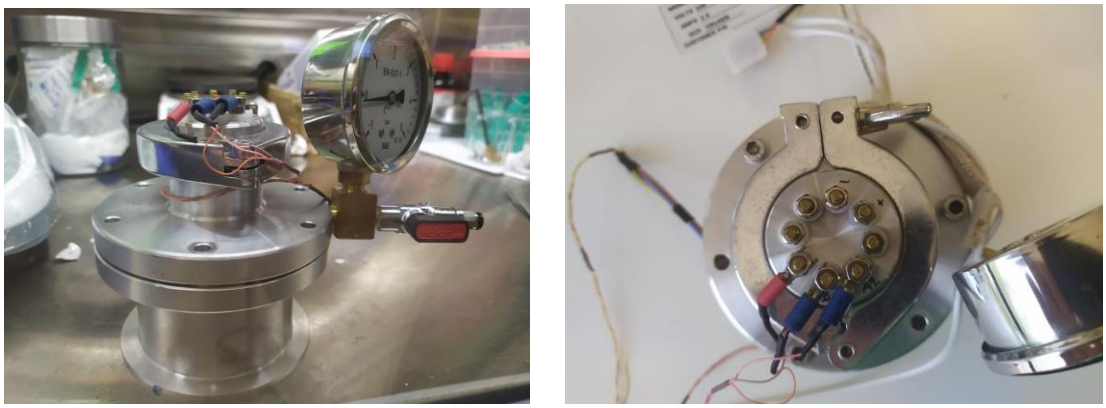

Figure 4.2: (Left) Side and (Right) top view of the inert atmosphere oven. Visible are the feedthrough on the top as well as the pressure gauge and valve.

4.1.3 Temperature controller and sample thermometer

To control the temperature of the environmental chamber a custom controller was designed. The requirements for it were to be able to control a heating element which would heat up the chamber while simultaneously "read" the temperature of the sample inside the chamber. The "heart" of the final system is an ATmega328p 8-bit microcontroller (MCU) as part of an Arduino UNO R3 board. Alongside it there are two MAX31865 RTD-to-Digital Converter modules operating in 3-wire configuration that measure the PT100's resistance and calculate the temperature as well as serially report it to the MCU. As peripheral components there are a 16x2 character LCD screen, a rotary encoder with a button, a status LED and a solid state relay.

Principle of Temperature Controller Operation

An ATmega328p 8-bit microcontroller (MCU) as part of an Arduino UNO R3 board "reads" two temperature values, one coming from the PT100 placed on the heating element (abbr. H.E.PT100) and one from the PT100 attached at the bottom electrode of the sample cell (abbr. SamplePT100). The setpoint temperature can be defined with a rotary encoder (Figure 4.5 right). The MCU calculates using the PID algorithm the power needed on the heating element for the H.E.PT100 to reach the user defined Setpoint temperature. The control of the heating element is done using a Solid State Relay (SSR), controlled by a low frequency (~30Hz) pulse width modulation (PWM), in parallel connected to the LED so that a LED lights up when the heating element is enabled. Alongside the H.E.PT100's temperature, PID algorithm also needs *P* or "Proportional, *I* or "Integral, and *D* or "Derivative" values stored in the MCU's EEPROM and can also be changed by the user. The controller is encased in a grounded aluminum case and is powered from PC's USB. The block diagram of the controller is pictured below. At the case of the controller, an LCD displays the Setpoint temperature, the temperature of the heating belt and the temperature of the bottom electrode.

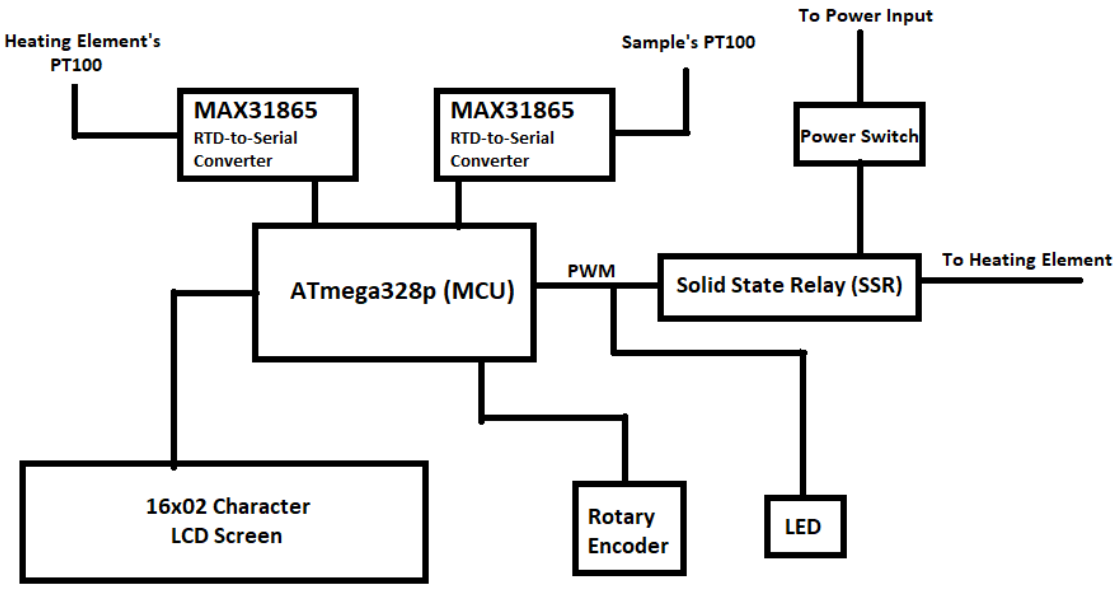

Figure 4.3 : Block Diagram of controller's components.

For the programming Arduino IDE was used and the Libraries utilized are the following:

1. PID by Brett Beauregard[69]
2. Adafruit_MAX31865 by Adafruit[70]
3. EEPROM by Arduino[71]
4. LiquidCrystal by Arduino[72]

For the wiring, a custom PCB was designed using Autodesk EAGLE, the design was transferred using the "toner transfer" method on an FR4 copper clad which was then etched using HCl / H_2O_2 solution to obtain the final board. The board's design as well as the picture of the final board are seen in Figure 4.4. The final assembly of the

controller can be seen in Figure 4.5, while the final set up with all the parts (Impedance analyzer, environmental chamber and temperature controller) can be seen in Figure 4.6.

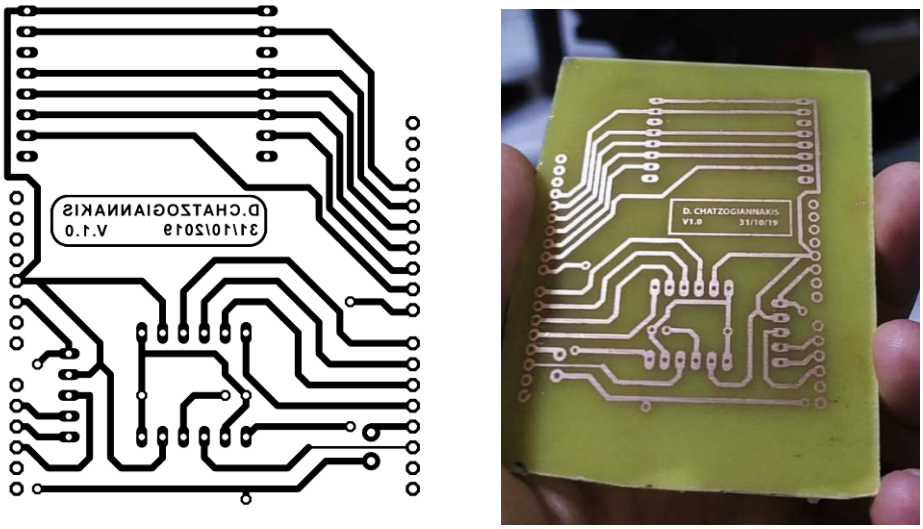

Figure 4.4: (Left) main PCB's design and (Right) the transferred and etched PCB

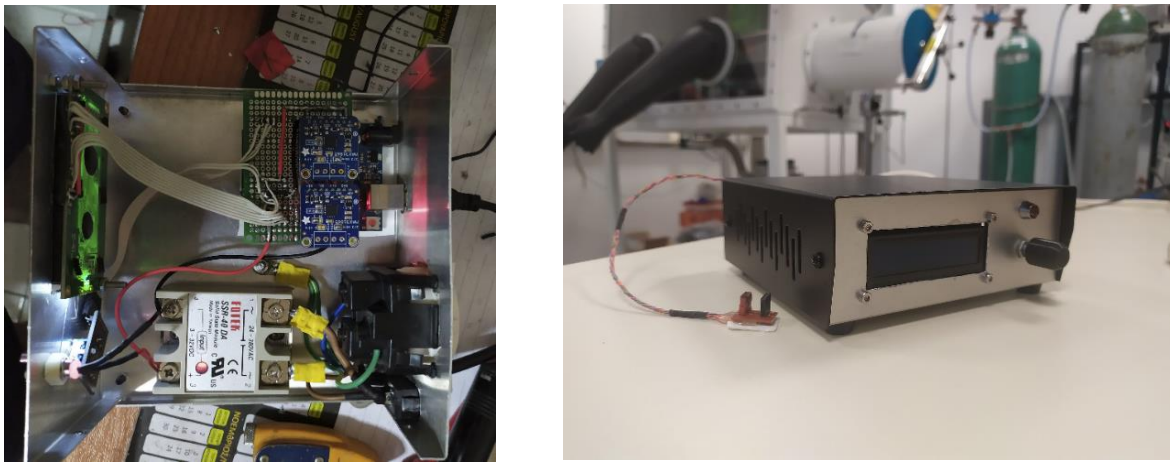

Figure 4.5: (Left) image showing the wired and assembled components in the controller. (Right) The completed controller.

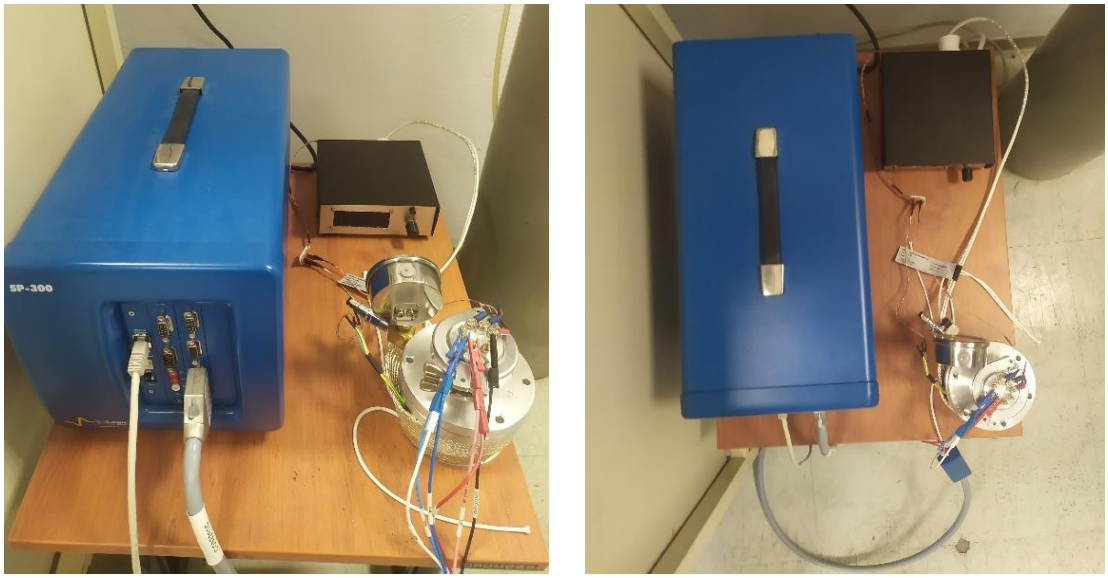

Figure 4.6: Images of the assembled Impedance measurement apparatus.

4.2 Electrochemical Impedance Spectroscopy (E.I.S.)

The conductivity measurement of polymer electrolytes was determined using Electrochemical Impedance Spectroscopy (EIS). For all the EIS measurements in this work, a cylindrical PTFE spacer with 4mm diameter and 2mm thickness was used in the home-made cell (Figure 4.1), which is assembled and loaded in an Argon filled Glovebox (MBraun EasyLab) and placed in the home-made airtight environmental chamber, as described in chapter 4.1. The home-made environmental chamber was then taken out of the Glovebox, wrapped with a heating belt, and was connected to the home-build controller and the impedance analyzer (Bio-Logic SP300).

Each polymer electrolyte was subjected to a slow heating and then a cooling scan from room temperature to 100^{o}C and back to room temperature with EIS spectra obtained every 5^{o}C. During both runs, the temperature was changed approximately 5^{o}C every 15 minutes. An excellent reproducibility of the ion-conductivity values during heating and cooling indicates both that the electrolyte has reached the target temperature and that no degradation of the electrolyte took place during the experiments.

Figure 4.7 shows a typical impedance spectra obtained from a polymer electrolyte with LPEO-5K and *r*=0.055.

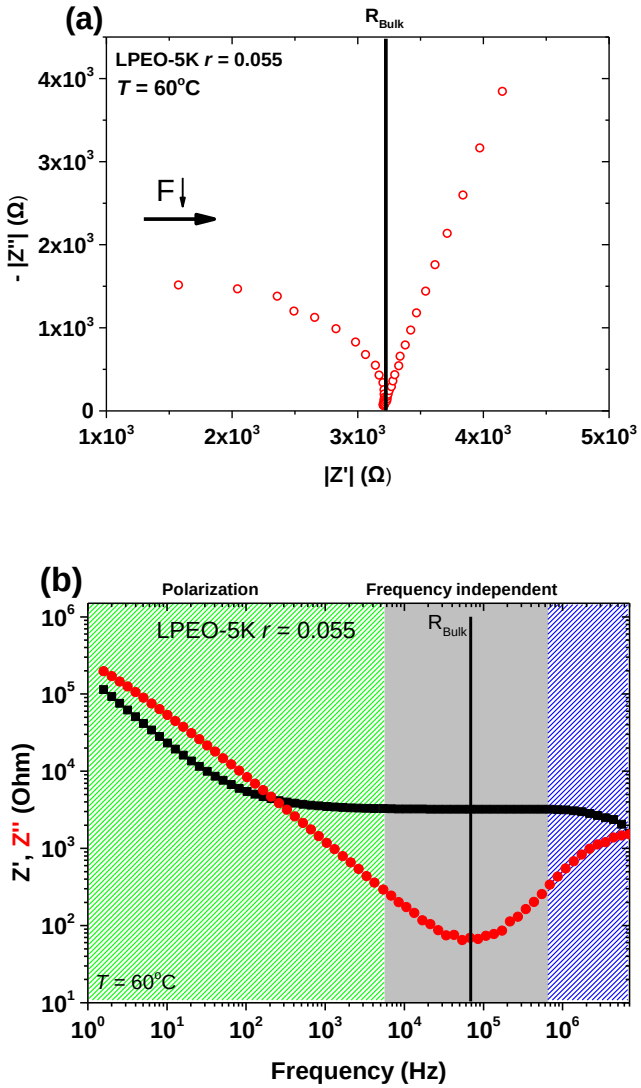

Figure 4.7: Impedance data obtained from LPEO-5K *r*=0.055 showing the typical behaviour of our electrolytes. Data are presented as (a) Nyquist plot and (B) Real (Z') and imaginary (Z") parts of conductivity as a function of Frequency. Solid black lines indicate the Bulk resistance, R_{bulk} of the electrolyte.

The D.C. Conductivity (σ_{dc}) was estimated from the bulk resistance (R_{bulk}) (as thoroughly described in Chapter 2) as:[68]

$$\sigma_{dc} = \frac{H}{R_{Bulk}A} \qquad [Eq. 4.1]$$

Where H is the thickness of the spacer, R_{bulk} is the impedance at the frequency independent plateau and A is the area of the electrode-sample interface.

We studied our systems in multiple temperatures and Figure 4.8 shows the effect of it on the Z' and Z'' of the LPEO-5K with r = 0.055 electrolyte. As one would expect, increasing temperature significantly lowers the R_{bulk} of the electrolyte and hence enhances its conductivity.

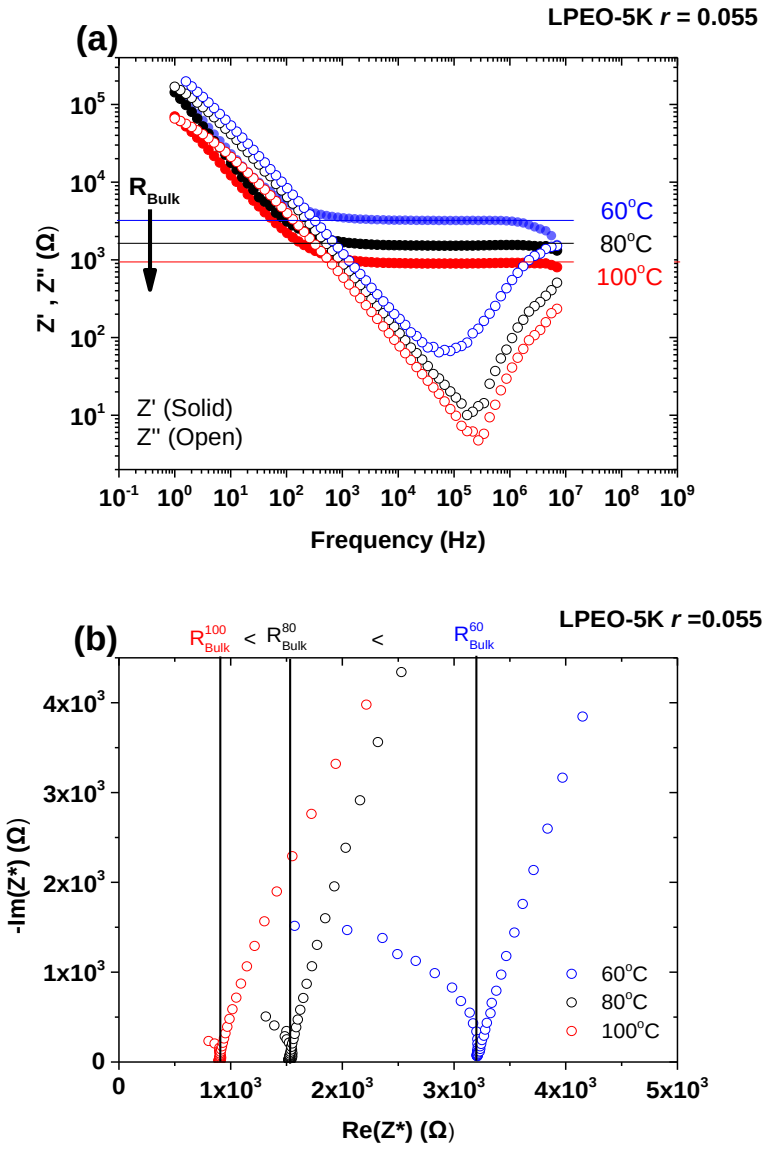

Figure 4.8: The effect of Temperature on (a) Z', Z'' vs Frequency and (b) Nyquist plot. Both plots show a significant reduction of bulk resistance with increasing temperature.

Figure 4.9 shows the ion conductivity as a function of temperature during heating (red open circles), and during cooling (blue triangles). During cooling there is an abrupt drop of ion conductivity at a temperature around 50°C, as the result of the crystallization of the specific polymer electrolyte. This is clear from Figure 4.10 where the ion conductivity during cooling is plotted along with the heat flow of the corresponding electrolyte during cooling (as measured with DSC). As it was discussed in the introduction, ion transport occur through the amorphous phase of the PEO based electrolyte. Similarly, the conductivity significantly increases when the materials goes through its melting temperature.

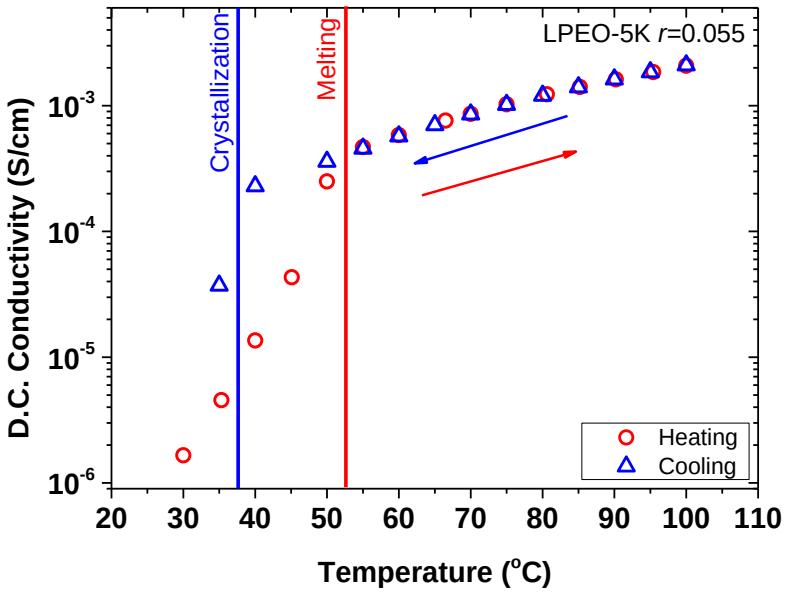

Figure 4.9: DC Conductivity of LPEO-5K:LiTFSI *r* = 0.055 as a function of temperature. Vertical Lines indicate the thermal transitions of the polymer during the scan. (Blue) Crystallization and (Red) Melting

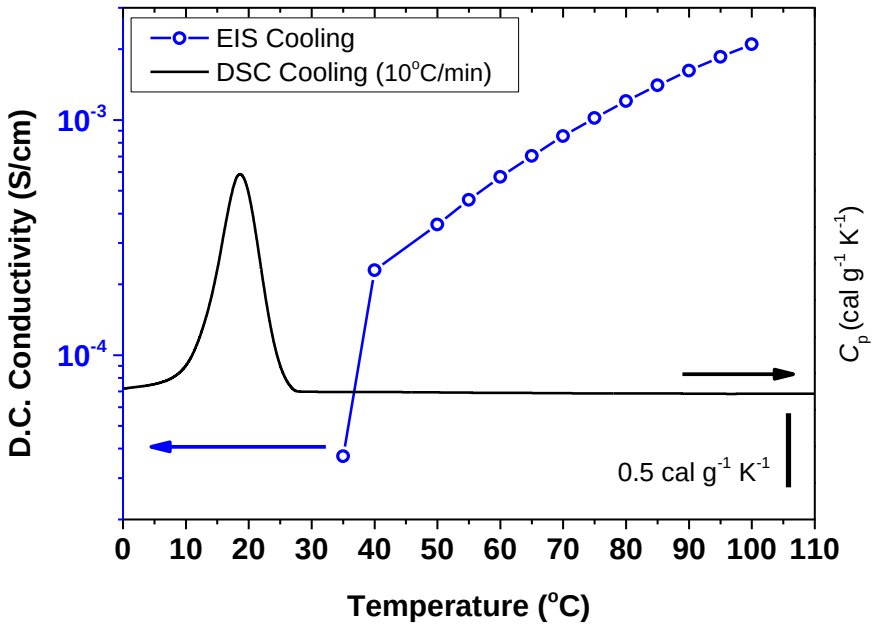

Figure 4.10: Overlay of EIS and DSC heating scans showing the agreement of the two techniques in the melting point of the sample LPEO-5K *r* = 0.055.

In Figure 4.11 with open symbol we plot the ion conductivity of LPEO-5k:LiTFSI electrolytes as a function of Lithium salt concentration for different temperatures. As expected and it has been reported for PEO:LiTFSI systems the conductivity increases the temperature while a non-monotonic behavior with *r* is seen.[5,25,27] The non-monotonic behavior can be explained in terms on the two competing effect discussed earlier (Chapter 1.4.3). . The solid symbols in Figure 4.11 is the data on PEO:LiTFSI electrolytes with similar M_w as in our case.[25] Notably, there is a very good agreement between the two sources indicating that the home-made set-up built during the course of this thesis produces reliable and accordance with the literature data.

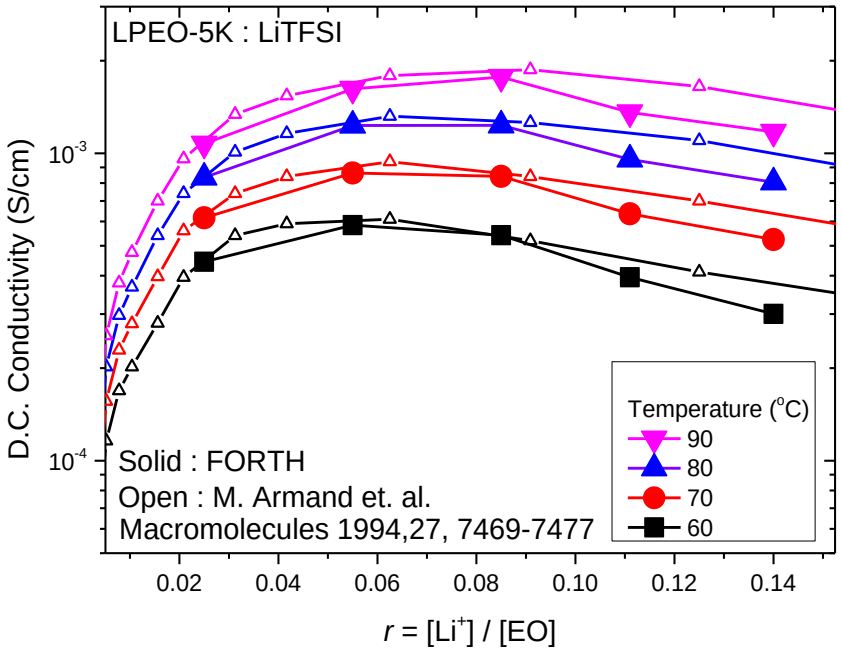

Figure 4.11: D.C. Conductivity as a function of *r* for various temperatures, a comparison between data measured in FORTH for this study (solid) and by Armand et.al (open).

4.3 Effect of PEO molecular weight (M_w) on the ionic conductivity of LPEO : LiTFSI blends.

We start our discussion on the effect of Mw on the conductivity properties from the PEO of the lowest M_w studied here, i.e. the LPEO-0.55K. Figure 4.12a, shows the ion-conductivity of LPEO-0.55K:LiTFSI electrolytes as a function of *r*, for different temperatures. . Noticeably, the maximum in conductivity (r_{max}) for the LPEO-0.55K electrolytes has a temperature dependence; r_{max} occurs at larger values as the temperature increases. This is clear in Figure 4.12b, where the ion-conductivity is plotted as a function of *r* for two temperatures. At T=30°C, the maximum in ion conductivity occurs at $r_{max} \approx 0.055$, while at T=100 °C occurs at $r_{max} \approx 0.085$ to 0.111. To

the best of our knowledge, such a temperature dependence on the r_{max} has not been reported before.

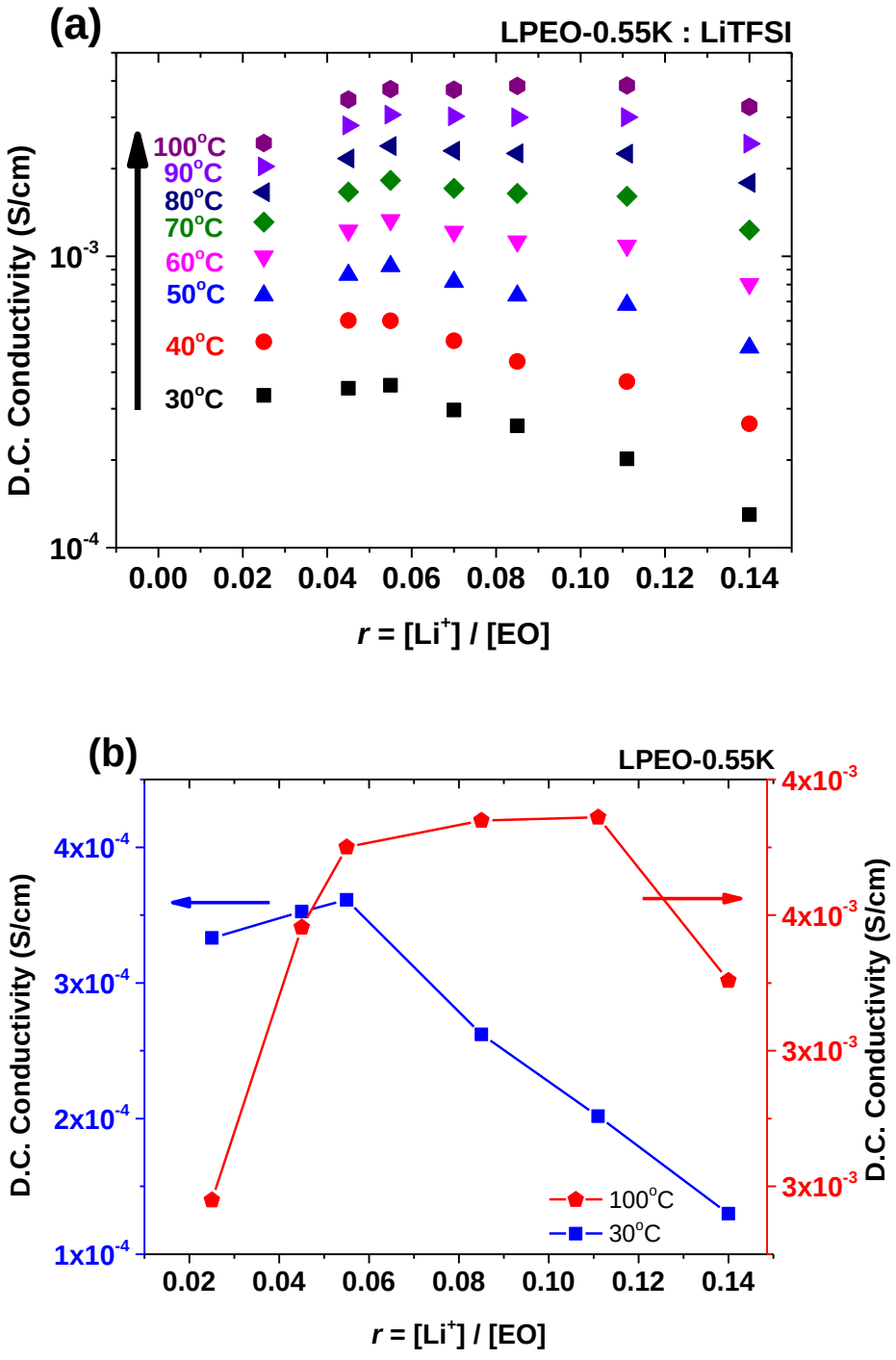

Figure 4.12: (a) D.C. Conductivity of LPEO-0.55K:LiTFSI electrolytes as a function of *r* for (a) various temperatures from 30°C to 100°C and (b) at 30°C (blue symbols, right axis) and at 100°C (red symbols, left axis)

As discussed in chapter 1.4.3, increasing LiTFSI amount in a PEO based electrolyte simultaneously slows down polymer's segmental dynamics and increases ion concentration resulting in a non-monotonic overall dependence of ion conductivity on *r*. In order to further investigate the aforementioned shift of r_{max} at higher temperatures, Raman spectroscopy was utilized to understand the effect of temperature on the degree of ion dissociation[24] (Figure 4.13) which could affect the number of free/dissociated ions in the sample. The principle of that analysis depends on a well-known $TFSI^-$ Raman peak, caused by a complex mixing of internal coordinates making the whole anion expand and contract and thus largely vary its polarizability. This absorption is evidenced at around 746 cm^{-1} when $TFSI^-$ is associated with Li^+. Separation of the two affects the electron density of $TFSI^-$ and causes the peak to shift to 740cm^{-1}. The *degree of dissociation* can be estimated by the ratio of the area under the free ion peak divided by the sum of the areas of both peaks. Figure 4.13a shows the range of interest of the Raman spectra of LPEO-0.55K *r*=0.070 sample showing that the area of the non-dissociated LiTFSI is negligible. In Figure 4.13b the ratio described above is plotted as a function of temperature. The two main points are that the degree of disassociation for the different LiTFSI amount used in this study is almost unity and most importantly does not change with temperature. The Raman measurements indicate that these samples have almost the entirety of the ions in the free state throughout the EIS measurement's temperature range. Please note that our measurements are consistent also with literature as ion aggregates (not fully LiTFSI dissociation) has been reported for $r > 0.125$.[24,29]

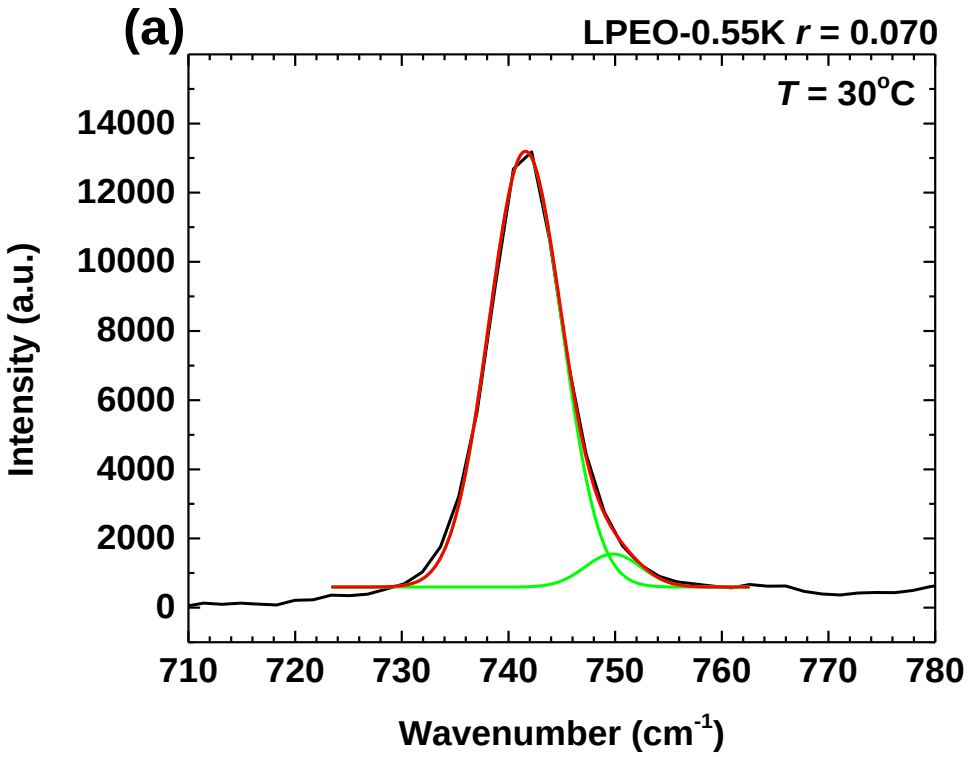

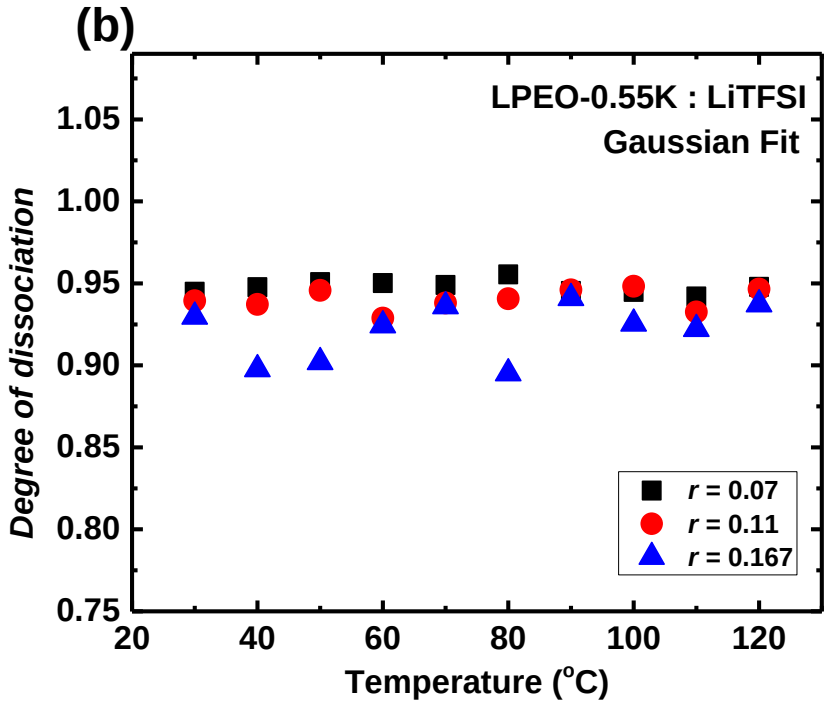

Figure 4.13: (a) Raman spectra obtained from LPEO-0.55K r=0.070 sample at 30°C showing the two peaks under interest for Degree of disassociation calculation and the corresponding fit used to deconvolute the peaks and obtain their areas. (b) Degree of

dissociation calculated for three LPEO-0.55K : LiTFSI electrolytes, all being very close to unity and invariant with temperature.

It is widely known that increasing temperature accelerates polymer dynamics which in turn increases the mobility of the ions contributing to the measured conductivity.

As discussed in chapter 1.4.7, the ion-conductivity of a polymer electrolyte has a non-monotonic dependence on the salt content, *r*. This is the result of two competing effects; as salt increases segmental dynamics become slower that tend decrease ion-conductivity (blue line in Figure 4.14), while simultaneously charge carrier density increase with *r* that tend to increase ion-conductivity (red line in figure 4. 14). As a result, the ion-conductivity has a non-monotonic behavior with r (black line if figure 4.14). As Raman measurements showed, changing the temperature of the electrolyte does not affect the charge carrier density, as no change on the degree of dissociation was measured in the temperature range from room temperature to 100°C. In other words the red line in figure 4.14 is unaffected with temperature. On the other hand, if temperature changes, for example decrease, polymer's segmental dynamics become slower, dashed blue line in figure 4.14. As a result, the competition between segmental dynamics and free-ion concentration result in a lower r_{max} for lower temperature (dashed black line in figure 4. 14).

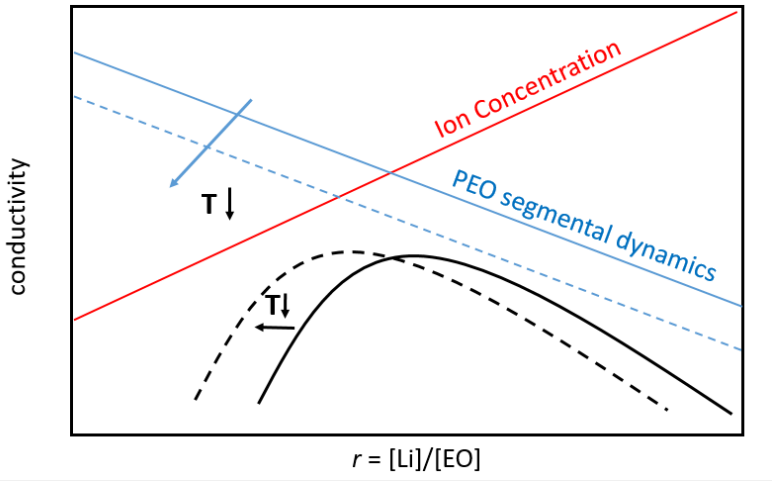

Figure 4.14: Qualitative explanation of r_{max} shift. Red line represents ion concentration. The blue solid line indicate the dependence of PEO segmental dynamics with *r*, that decreases with increasing *r*. The dashed line indicates the

corresponding segmental dynamics for a lower temperature. Black solid line represents the convolution of the two behaviours while black dashed line indicates the same response at lower temperature.

Figure 4.15a shows the effect of temperature on the ion conductivity of LPEO-0.55K:LiTFSI electrolytes at different ion concentrations, *r*. As discussed in Chapter 3.1, due to the interactions of Li^+ with EO, the addition of the LiTFSI increases the glass transition temperature of PEO, i.e. decrease the segmental dynamics of the PEO. In order to account for the difference in polymer dynamics with the addition of LiTFSI, Figure 4.15b plots the ionic conductivity as a function of T-T_g. It is clear, that with increasing the lithium salt the ionic conductivity increases as shown in the Tg-normalized plot.

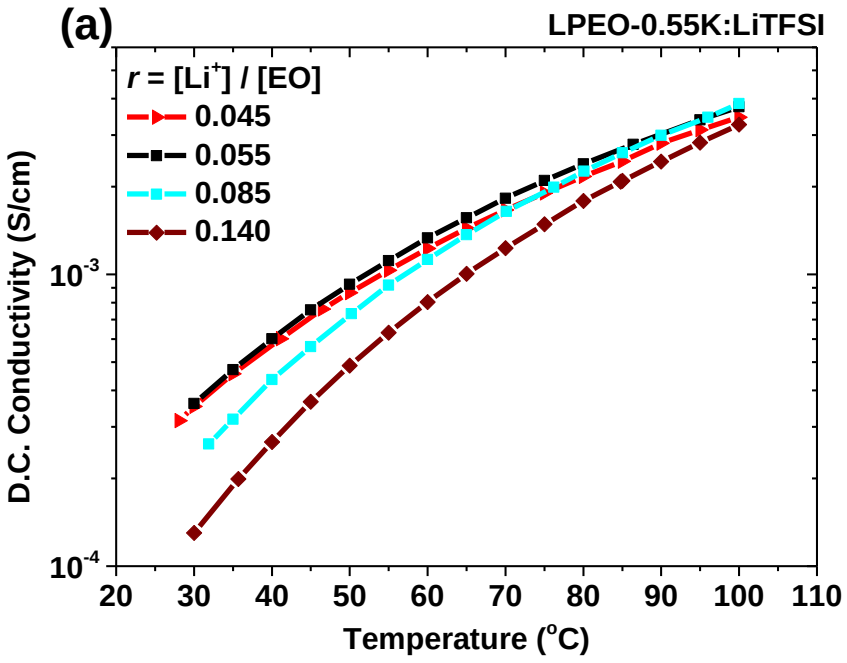

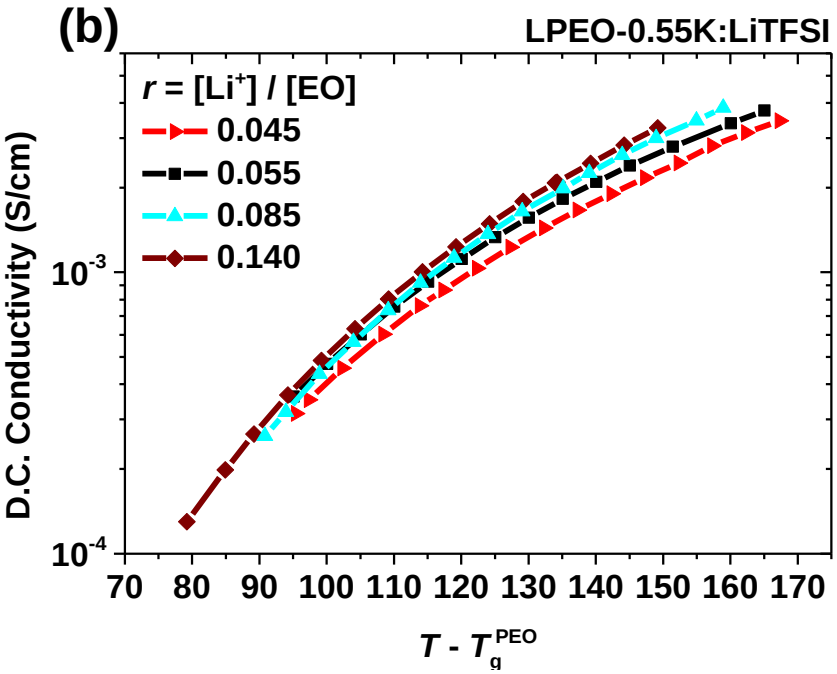

Figure 4.15: (a) LPEO-0.55K:LiTFSI D.C. Conductivity as a function of Temperature. (b) D.C. Conductivity vs T-T_g^{PEO} showing that when segmental dynamics of polymer is comparable, higher r improves conductivity.

As discussed in chapter 1, the ionic conductivity of a polymer electrolyte depends on the concentration of charge carriers as described by by Kohlrauch equation:

$$\sigma_{dc} \propto \sum_i \mu_i q_i n_i \qquad [Eq. 4.2]$$

Where i is each ion, μ_i is the mobility of the ion, q_i is its charge and n_i its concentration. The concentration, n, of LiTFSI in the polymer electrolyte could be estimated using the formula:[29]

$$n = n_{Li^+} + n_{TFSI^-} = 2\frac{\rho r}{M_{EO} + rM_{LiTFSI}} \qquad [Eq. 4.3]$$

Where ρ is the density of the sample as M_{EO} and M_{LiTFSI} are the molar masses of the ethyleneoxide monomer (44.05 g/mol) and LiTFSI (287.09 g/mol) respectively. Densities were calculated from interpolation of data from Pesko et.al [29]. Figure 4.16

plots the ion conductivity of the LPEO-0.55K:LiTFSI electrolytes, normalized by the ion concentration $n = (n_{Li}+n_{TFSI})$ versus $T - T_g$. It is clear that the data do not collapse to the same curve. Our data indicate that with increasing salt (i.e. with higher ion density) there is a reduced contribution of each charger carrier to the total conductivity. A possible explanation can be the ion-ion interactions forming clusters and temporarily "canceling out" charges, that get stronger with increasing *r*. Along the same line, Pesko et.al[29] reported that Lithium ions can move to the opposite to the applied electrical field with increasing salt concentration due to the formation of Li/TFSI clusters.

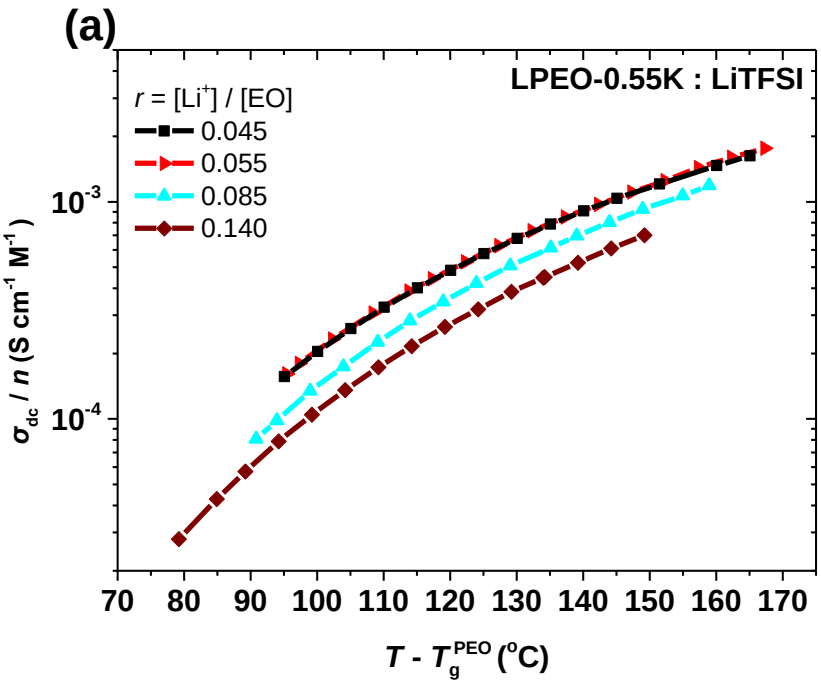

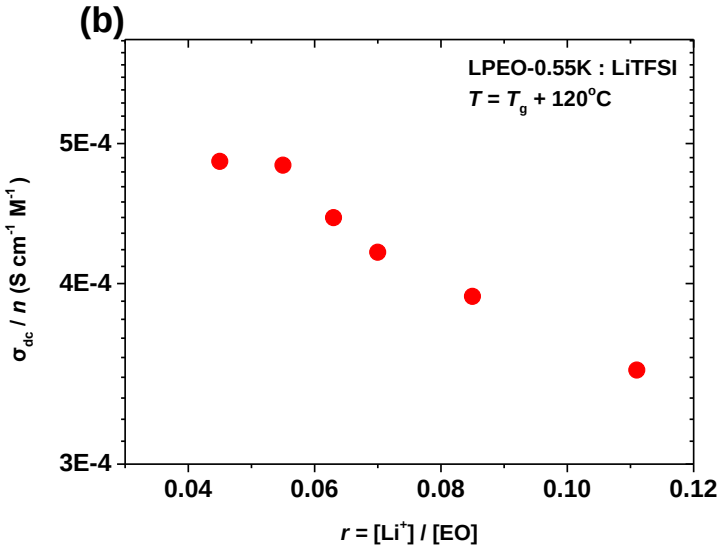

Figure 4.16: (a) Ratio of conductivity to concentration (σ_{dc} / (n_{Li}+n_{TFSI})) versus T-T_g showing the declining effect the addition of salt exhibits. T-T_g was used to remove segmental dynamics from the picture. (b) a different view of the declining value of σ_{dc} / (n_{Li}+n_{TFSI}) C with r at T = T_g + 120°C.

We now turn our attention on the effect of the molecular weight of linear PEO on the conductivity properties of PEO electrolytes. To do so, three polymers were used: Linear *poly*(*ethylene-oxide*) with molecular weights (M_w) of 550, 1900 and 5000 *g/mol* (LPEO-0.5K, LPEO-1.9K and LPEO-5K, respectively). Molecular weights were chosen due to PEO having a molecular weight of entanglement, M_e close to 2000 *g/mol*[26] and so, under study is a polymer significantly smaller than that (LPEO-0.55K), one with comparable M_w (LPEO-1.9K) and one significantly larger (LPEO-5K). The procedures followed for the conductivity measurements were the same as those explained in chapter 4.2. Figure 4.17 below shows the D.C. Conductivity as a function of r for (a) LPEO-1.9K and (b) LPEO-5K as shown for LPEO-0.55K in Figure 4.12a.

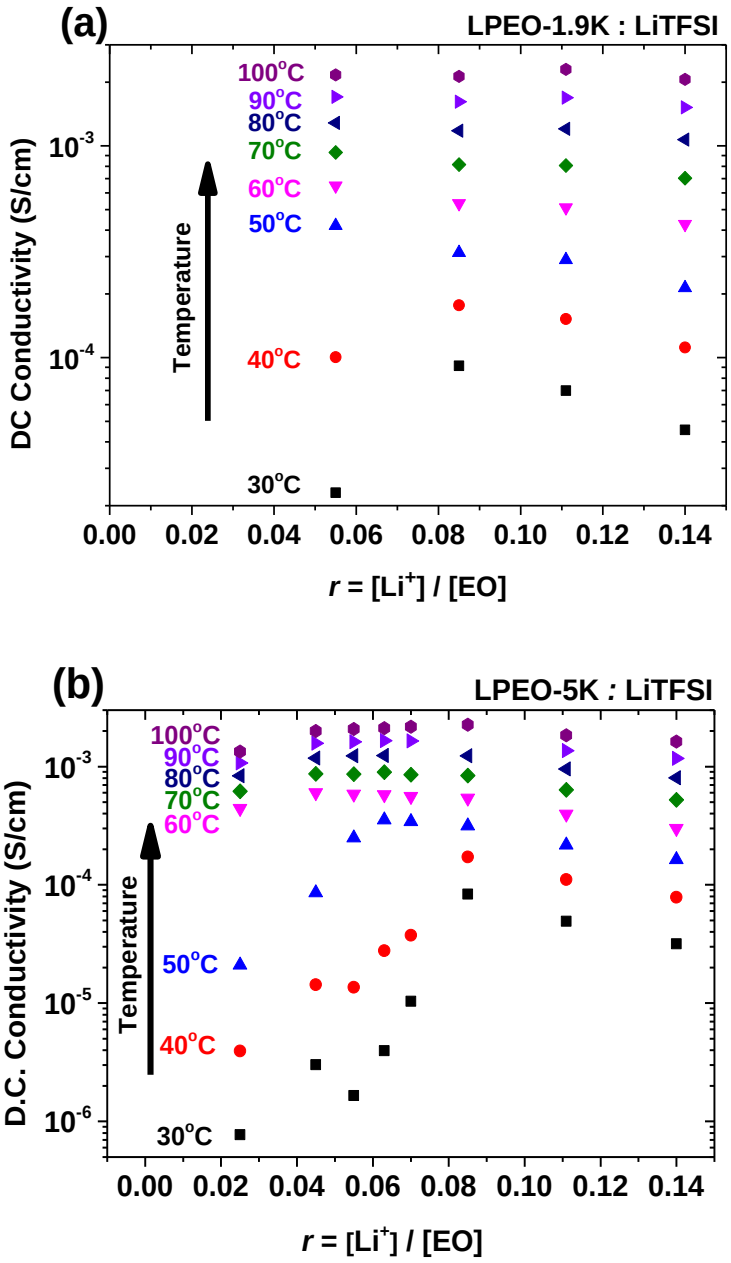

Figure 4.17: D.C. Conductivity as a function of *r* for (a) LPEO-1.9K:LiTFSI and (b) LPEO-5K:LiTFSI electrolytes

The temperature and LiTFSI concentration dependence of the ion conductivity of LPEO-1.9K and LPEO-5K behave qualitatively the same as the LPEO-0.55K (Figure 4.12). In particular, the conductivity increases with temperature, has a non-monotonic relationship with *r* and its maximum (r_{max}) shifts at larger values with temperature (Figure 4.18).

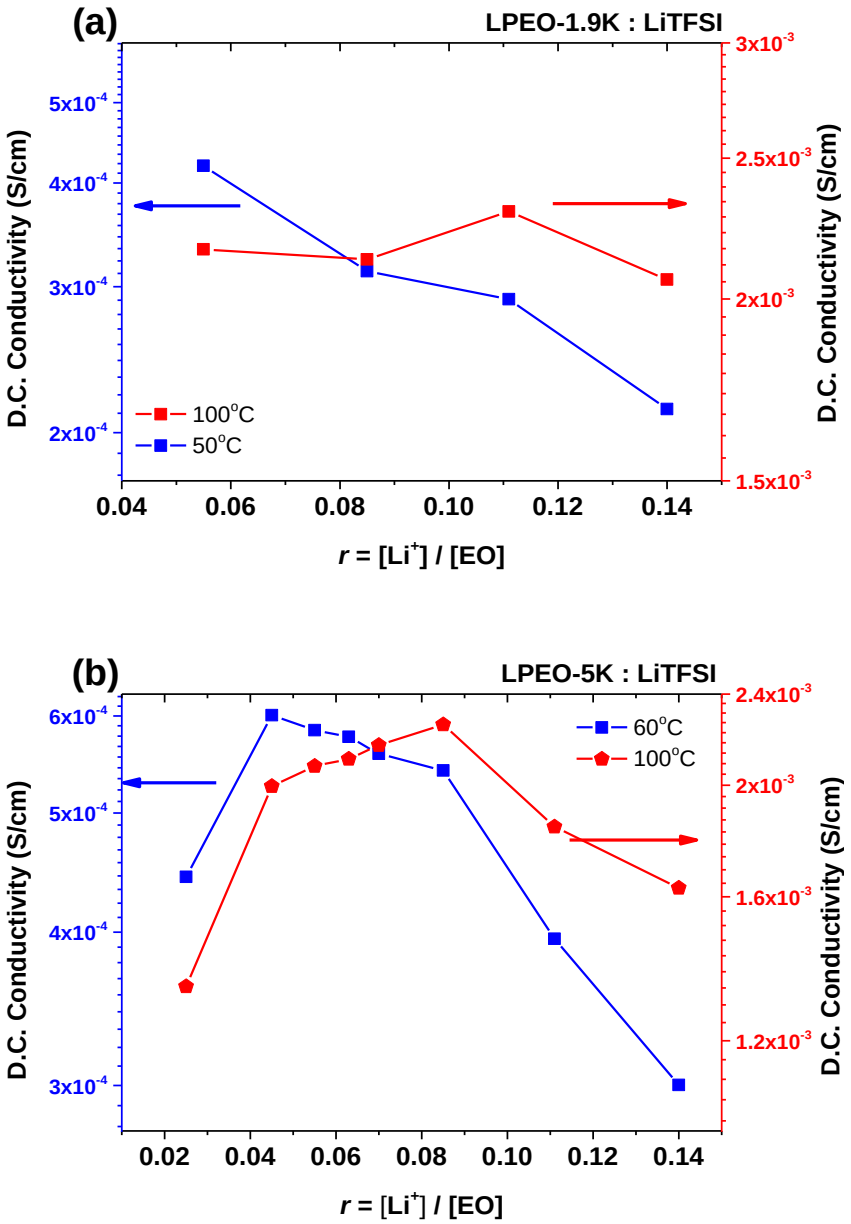

Figure 4.18: D.C. Conductivity as a function of *r* for high (red) and low (blue) temperature of (a) LPEO-1.9K:LiTFSI and (b) LPEO-5K:LiTFSI electrolytes.

The difference between those molecules shows when we plot comparatively their D.C. Conductivity as a function of temperature (Figure 4.19a) where one can see that LPEO-0,55K:LiTFSI electrolytes show much higher conductivity than the other two; LPEO-1.9K's and LPEO-5K's electrolytes show very similar conductivity values. Figure 4.19b shows that the dependence of Ion conductivity on temperature follows a Vogel

– Fulcher – Tammann (VFT) equation, which is consistent with the literature on these systems.[66]

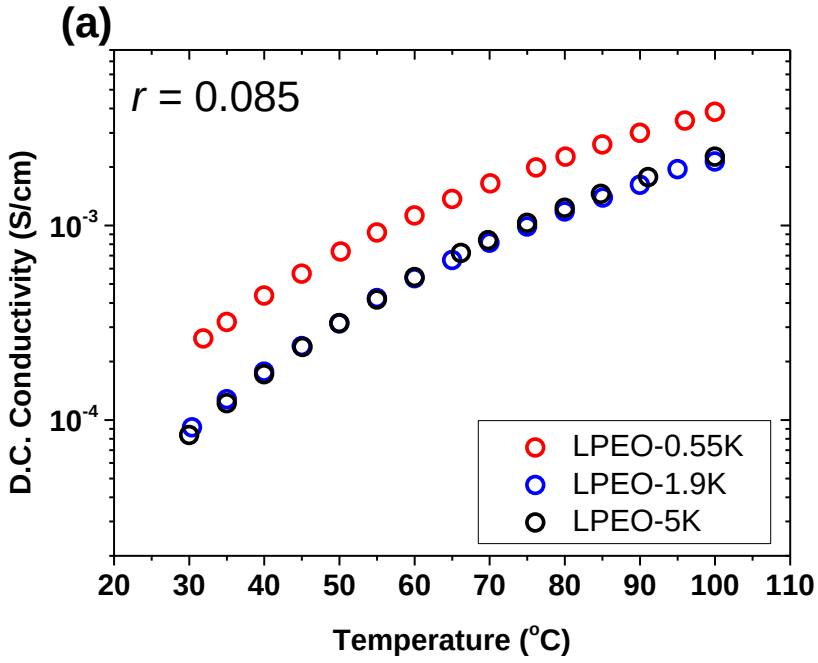

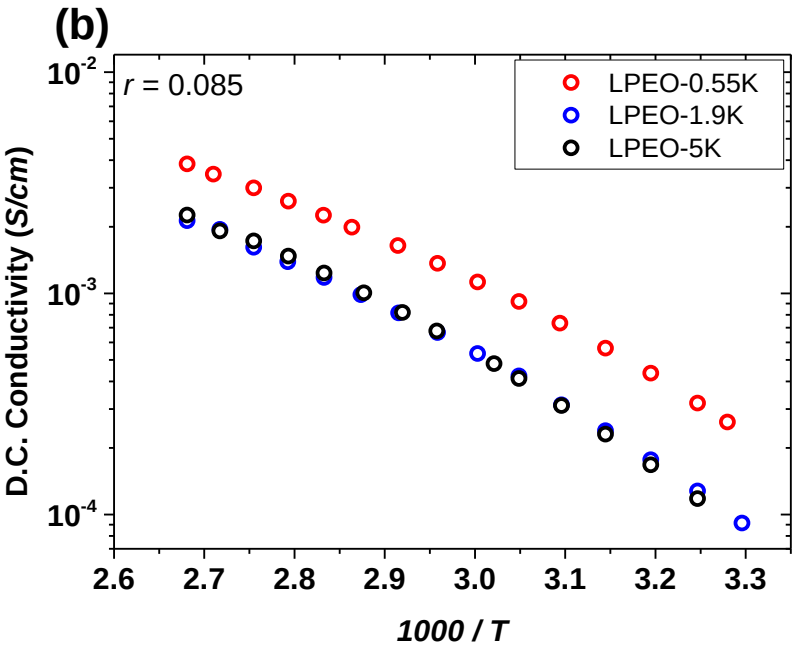

Figure 4.19: D.C. Conductivity as a function of Temperature for LPEO-0.55K (Red), LPEO-1.9K (Blue) and LPEO-5K (Black) based electrolytes (a) as a function of temperature T and (b) as a function of inverse temperature (1000/T).

Figure 4.20 shows the ion conductivity as a function of *r* for all the different linear PEO:LiTFSI electrolytes studied her at *T* = 40 °C and *T* = 100 °C for two different temperatures of 40 °C and 100°C, Figure 4.20 a and b respectively. While where the two higher molecular weight polymers show similar values with LPEO-0.55K being significantly the most conductive of all.

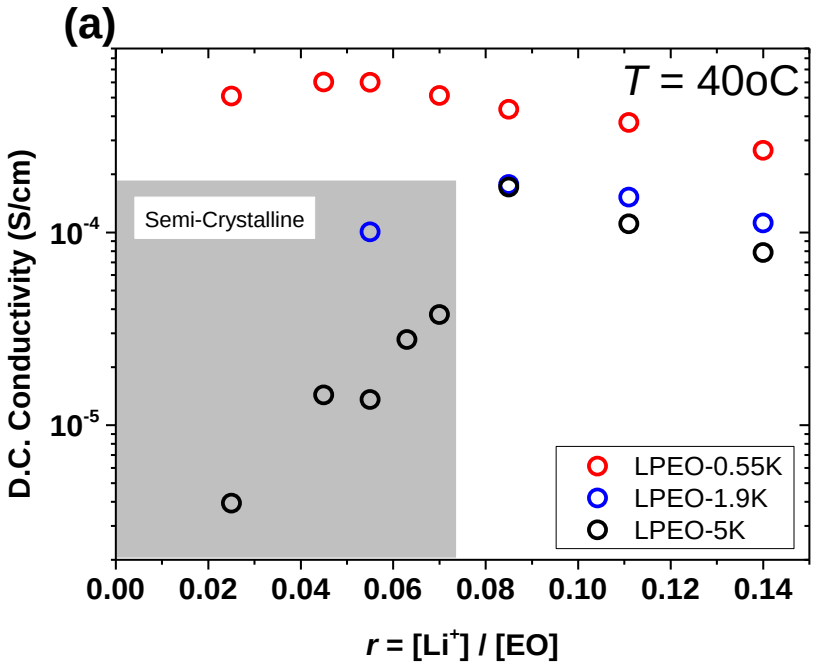

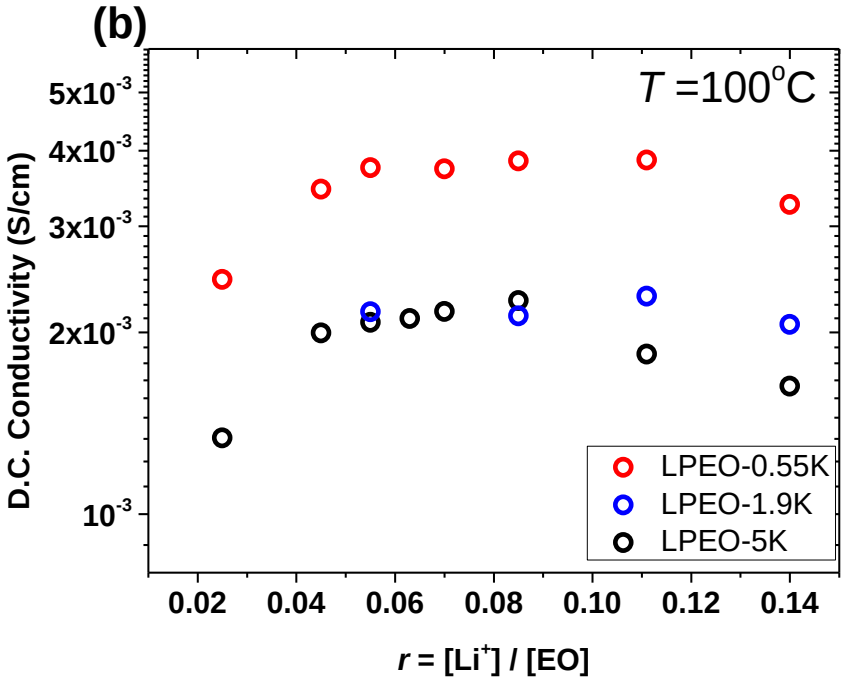

Figure 4.20: D.C. Conductivity of as a function of *r* for LPEO-0.55K (Red), LPEO-1.9K (Blue) and LPEO-5K (Black) based electrolytes at (a) 40°C and (b) 100°C. The grey area in figure 1 high-light the polymer electrolytes that were semi-crystalline at 40 °C.

The above behaviour has been seen in the literature[27] before and further increase of the molecular weight is not expected to significantly change the conductivity as the quantity reaches a plateau. To test that, the ion conductivity of PEO with M_w = 10 kg/mol blended with LiTFSI at r = 0.085 was measured and it is plotted along with the other linear PEO in the results confirm that at $M_w \geq M_e$ there is no M_w dependence on the ion conductivity. Noticeably, figure 4.20 indicates that r_{max} has a M_w dependence for the linear PEO electrolytes. In particular this is more pronounced at T = 40 °C where $r_{max} \approx 0.055$ for the LPEO-0.55K while for the LPEO-5K, $r_{max} \approx 0.085$. The analysis of the thermal properties of the linear PEO electrolytes showed that for the LPEO-5K the maximum in ion-conductivity occurs at the *r* concentration that LPEO is amorphous (Figure 3.2); please not that T_c for the LPEO is higher than room temperature. In other words, our data indicate that the r_{max} for the LPEO-5K is not dictated by the competition of the ion concentration and segmental dynamics, as in the case of LPEO-0.55K that is amorphous at room temperature, but rather by the presence of semicrystalline regions that decrease ion conductivity.

Interestingly, at T =100 C, i.e. at a temperature that both LPEO-0.55K and LPEO-5K are in the amorphous state for all r, the r_{max}, within the experimental, appear slightly larger for the LPEO-0.55K. This could be due to the fact that LPEO-0.55K is at much larger distance from T_g, polymer dynamics are faster and the turnover in ion-conductivity would occur at higher r (in a similar manner as Figure 4.14).

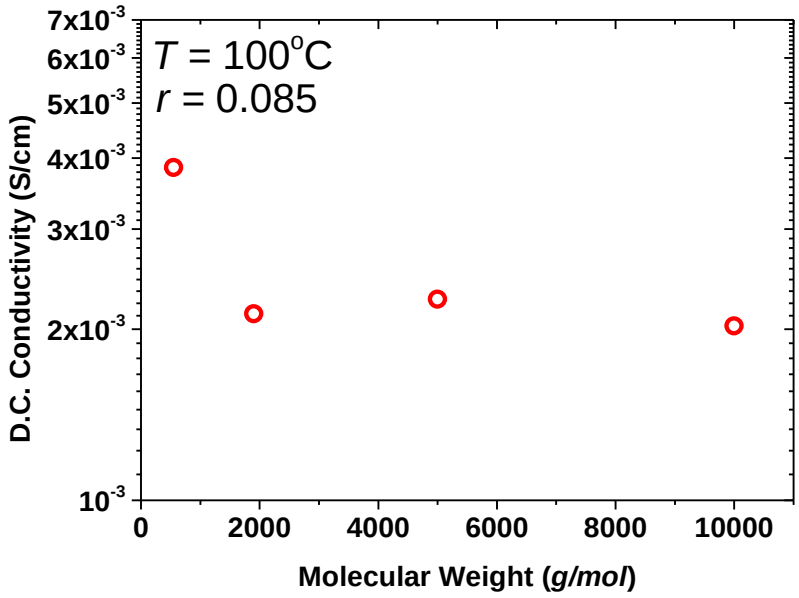

Figure 4.21: Effect of PEO's molecular weight on D.C. Conductivity at 100°C with r=0.085 showing no significant difference from 1900 to 10000 g/mol.

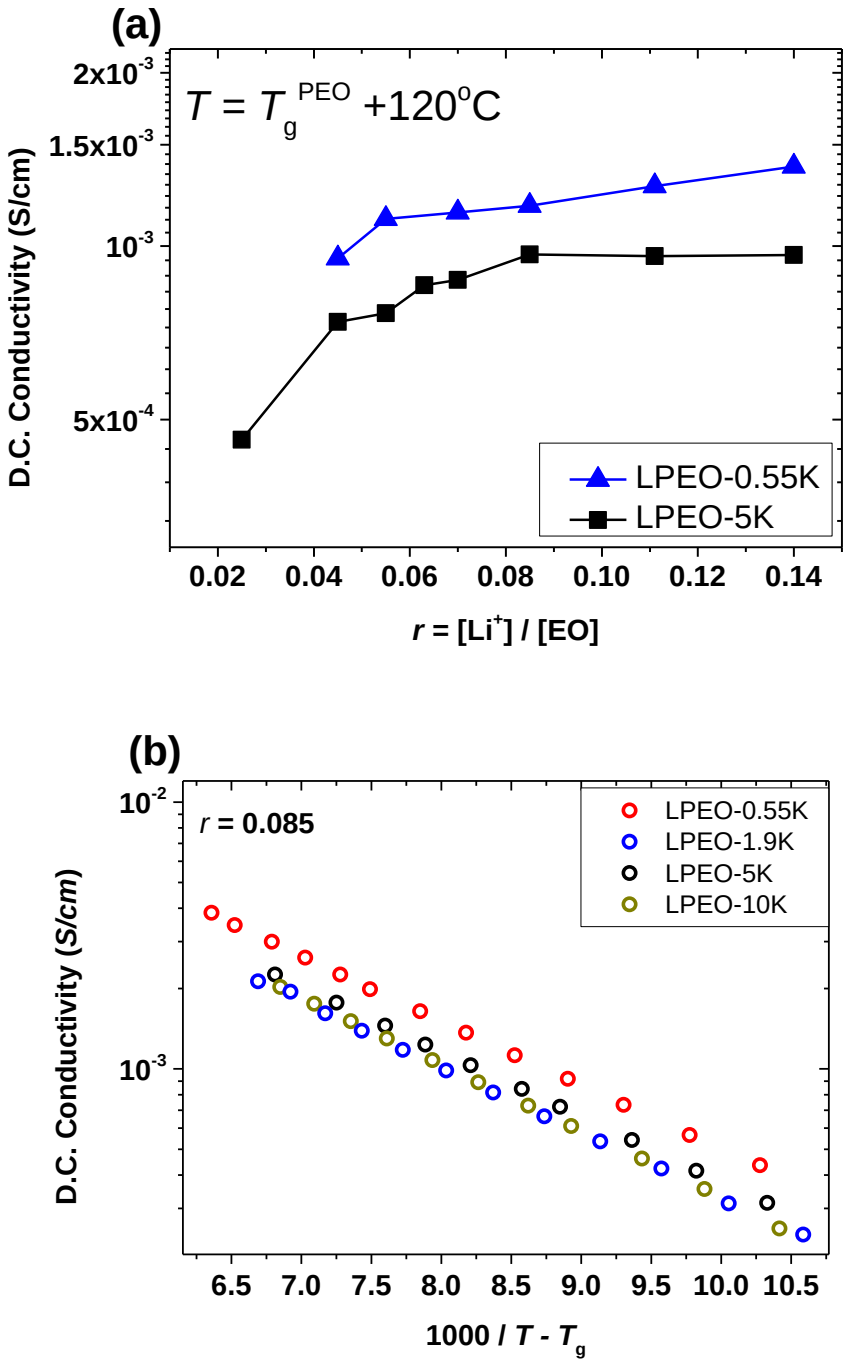

Figure 4.22: (a) D.C. Conductivity as a function of *r* at temperature 120°C above T_g^{PEO} for LPEO-0.55K and LPEO-5K electrolytes, (b) The D.C. Conductivity of all linear polymer electrolytes with *r* =0.085 as a function of $1000/T\text{-}T_g^{PEO}$ showing the superiority of LPEO-0.55K : LiTFSI electrolytes in terms of conductivity even when segmental dynamics are comparable.

One may argue that the larger ion conductivity of LPEO-0.55K:LiTFSI could be due to the faster segmental dynamics compared to higher M_W PEO, as it can be seen

also in Figure 3.8 in terms of the M_w dependence on the glass transition temperature of LPEO:LiTFSI systems. Nevertheless, Figure 4.22a where the ion Conductivity of LPEO-5K:LiTFSI and LPEO-0.55K:LiTFSI electrolytes are plotted as a function of *r*at equal distance from T_g (T_g+120^{o}C) and Figure 4.22b where the ion Conductivity is plotted as a function of $1000/T\text{-}T_g$ indicates that the differences in segmental dynamics does not account *per se* for the observed M_w dependence on conductivity. As discussed in chapter 1.4.2 ions move through electrolyte using two main mechanisms, "Fluctuation driven diffusion / Hopping" and "Vehicular diffusion".[27,73] At $M_w \leq M_e$ molecular weights chains such as those of LPEO-0.55K can easily diffuse and the measured conductivity is primarily attributed to the faster "vehicular diffusion" type. For $M_w \geq M_e$, entanglements and corresponding constrained significantly affect, slow down diffusion and the main mechanism of ion transport is through the slower hopping mechanism.

It is important to point out that low molecular weight PEO overcomes most of the problems associated with the low ionic conductivity of PEO electrolytes with $M_w \geq M_e$ but lacks the necessary mechanical properties for its utilization in solid polymer electrolytes. Nevertheless, understanding the ion-transport properties in such materials is or paramount importance as such low M_w PEO electrolytes could be used as the "fast" ion-conductive phase in nanostructured, multiphase polymer electrolytes. In particular, it was demonstrated that when poly(methyl methacrylate), PMMA, nanoparticles (PMMA-NP) were added to the liquid LPEO-0.55K polymer electrolyte, both the elastic modulus and the ionic conductivity of the resulting SPE increased compared to the linear blend analogues. In particular, the addition of 53 wt% PMMA nanoparticles resulted in SPEs that exhibited two orders of magnitude higher conductivity and one order of magnitude higher mechanical strength as compared to their linear PMMA blend analogues.[5,74] Notably, at room temperature PMMA-NP/PEO/LiTFSI electrolytes have a $\sigma > 10^{-4}$ *S/cm* and a shear modulus of G' ≈1 *MPa*, outperforming the corresponding nanocomposite electrolytes made with the addition of silica NPs.[75,76] The key to this phenomenon is the morphology of the resulting SPEs as nanostructured composite materials with highly interconnected conducting regions, pure in liquid PEO, were formed as the result of PMMA

nanoparticle dispersion within the liquid electrolyte. These differences in morphology resulted in a significant decoupling of conductivity from the mechanical strength for the PMMA-NP/PEO blends, even when the electrolyte was in the solid state.

Furthermore, it has recently been shown that when "amphiphilic" nanostructured polymer particles, composed of mikto-arm stars with a very large number of arms (functionality) of ion conducting poly(ethylene oxide), PEO, along with stiff insulating polystyrene arms, PS, PS_nPEO_n, where n = 30 the number of each type of arms), were added to LPEO:LiTFSI electrolyte, SPEs that exhibit and unprecedented combination of high modules and ionic-conductivity at room temperature are formed. In particular, the addition of 44 wt% $PS_{30}PEO_{30}$ in liquid PEO:LiTFSI electrolyte resulted in SPEs with a shear modulus of G' ~ 0.1 *GPa* and ion conductivity σ ~ 10^{-4} *S/cm*, at room temperature.[53,5] The SPEs showed a strong decoupling between the mechanical behavior and the ionic-conductivity as G' remains fairly constant for temperatures up to the glass transition temperature of the PS blocks, while the conductivity monotonically increased to reach $\sigma \sim 10^{-2}$ *S/cm*. The key to the performance of the SPEs is their morphology that stems from the ability of the $PS_{30}PEO_{30}$ nanoparticles to self-assemble in highly interconnected structures within the liquid electrolytes host.

4.4 Effect of star architecture on the ionic conductivity of PEO:LiTFSI blends

To study the effect of macromolecular architecture on the ionic conductivity of PEO:LiTFSI electrolytes, two star-shaped PEO polymers were considered in the study One having 3 arms with a molecular weight per arm M_w^{arm} = 0.87 kg/mol and one with and one with 60 PEO arms bound on a DVB core and M_w^{arm} = 60 kg/mol . As described in chapter 2 the latter was synthesized with the "arm-first" method and its core was made by sequential anionic polymerization of styrene and divinylbenze with equal nymber of PS arms with a low molecular weight of 6K. NRM indicated that wt% of the core is only 14 (See table 2.1). . The two molecules are named upon the number

and length of their arms and thus the former will be referred to as S(3)PEO(0.87K) and the latter S(60)PEO(60K).

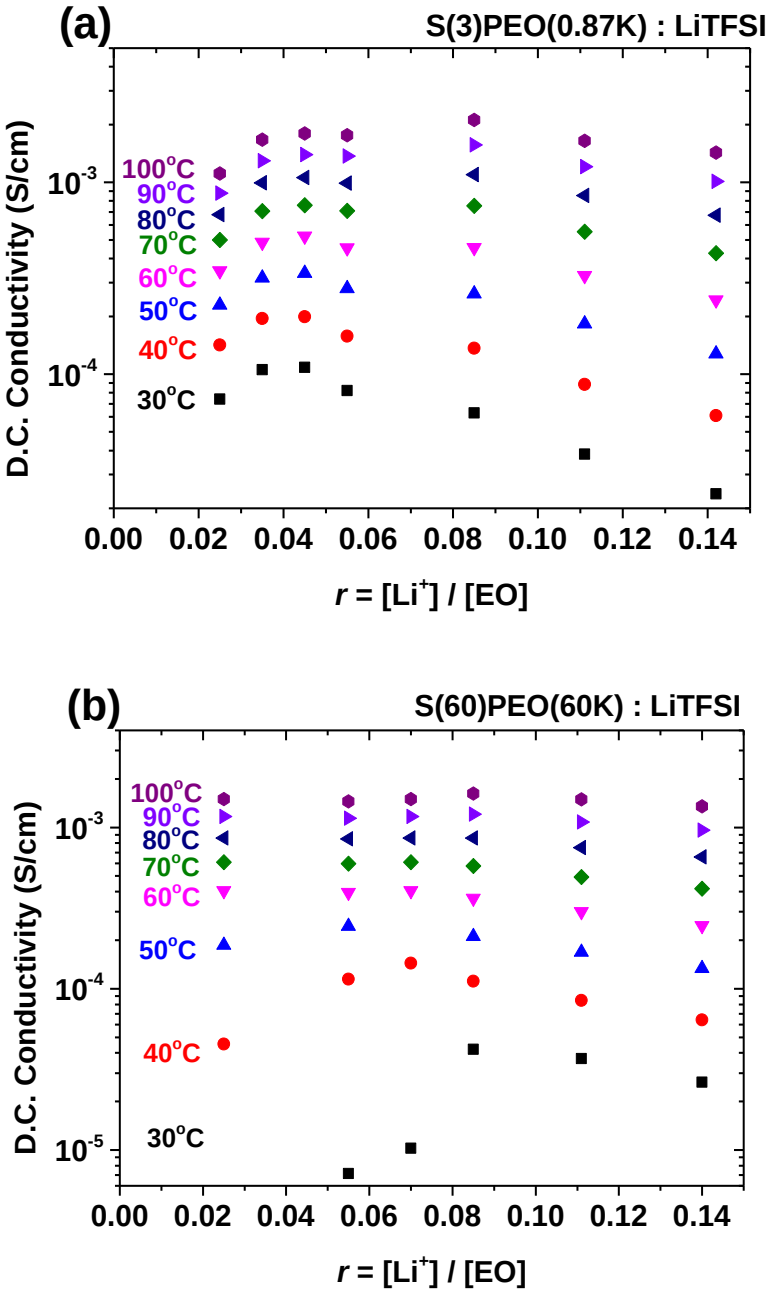

Figure 4.23 : D.C. Conductivity as a function of *r* for the SPEO:LiTFSI electrolytes based on (a) S(3)PEO(0.87K) and (b) S(60)PEO(60K).

Figure 4.23 shows the ion Conductivity as a function of *r* for the two star-shaped PEO polymers. As in the case of linear PEO electrolytes, the conductivity of star-shaped PEO electrolytes increases with temperature and has a non-monotonic on *r*. The high

functionality star has a weaker dependence on r while the shift of r_{max} at larger values with temperature for both stars occurs at around 0.085

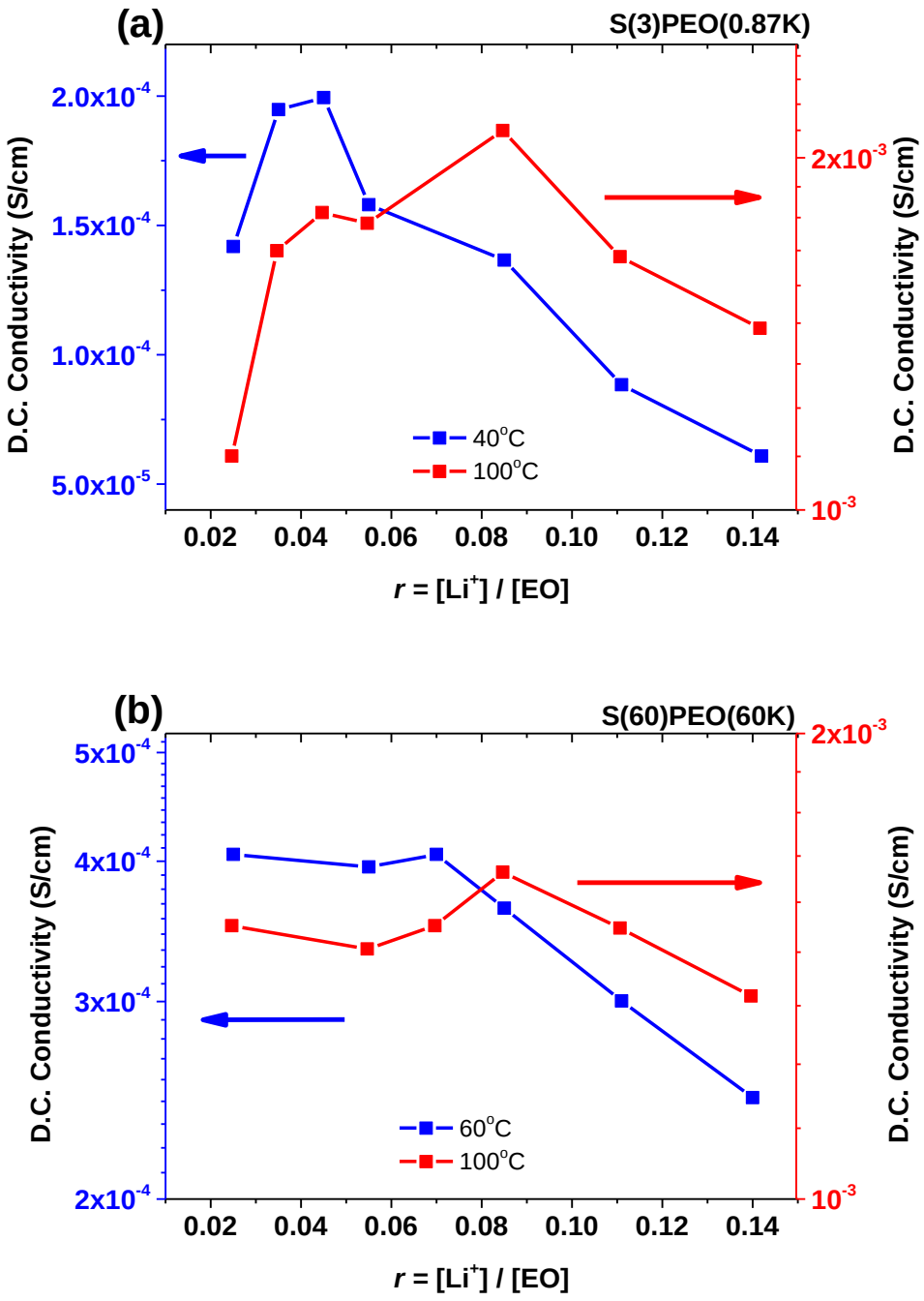

Figure 4.24: D.C. Conductivity as a function of *r* for two temperatures showing the shift of the observed maximum.

Figure 4.25 plots the effect of *r* of ion conductivity at two different temperatures for the star-shaped polymers, along with the corresponding data of

linear PEO electrolytes. It is immediately apparent that both stars have conductivity values comparable to those of the larger linear ones. The gray area in Figure 4.25a, highlights the sample that the material was semicrystalline (as was reported in Chapter 3, based on DSC measurements). Interestingly, S(3)PEO(0.87K) due to its low melting temperature is in the amorphous state for the whole *r* ranged studied and its ion conductivity appears much larger compared to the corresponding linear polymer PEO with the same molecular weight, LPEO-5K. Notably, even at higher temperatures the ion conductivity of S(3)PEO(0.87K) is very similar to that of LPEO-5K.

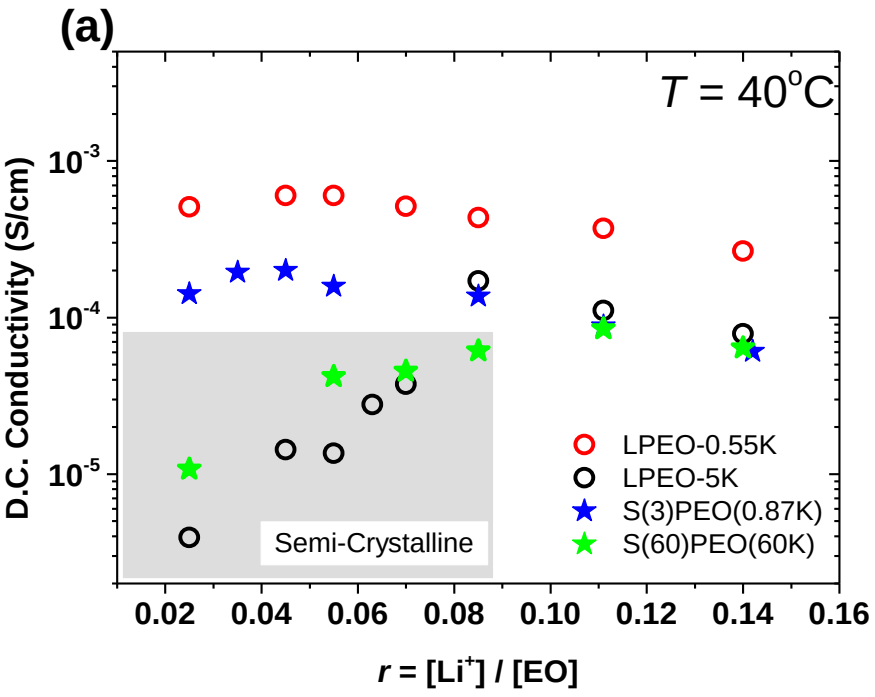

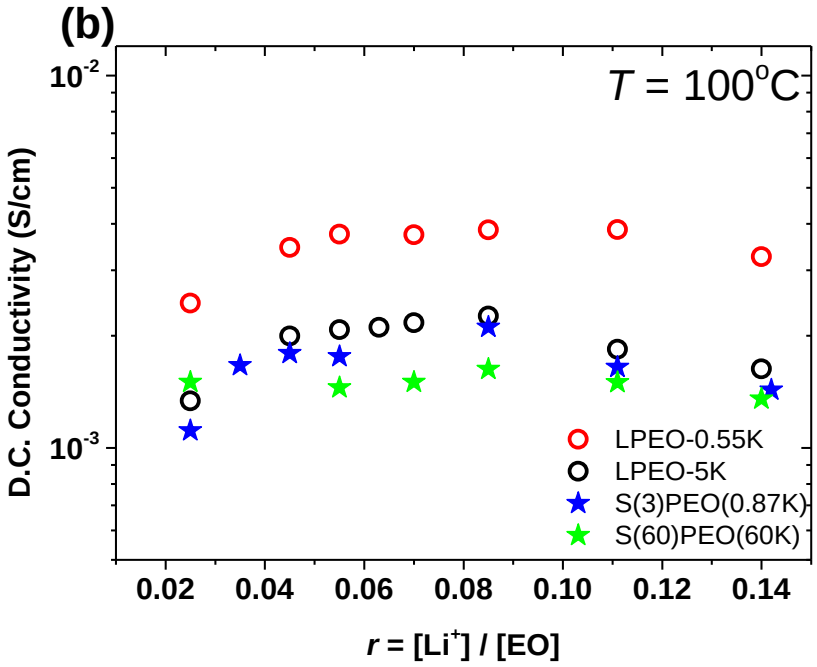

Figure 4.25: D.C. Conductivity as a function of *r* for 4 different molecules at temperature (a) T=40°C and (b) T=100°C. The grey area in figure (a) indicate the polymer electrolytes that were semi-crystalline at 40 °C.

Regarding the high functionality S(60)PEO(60K) star, the ion conductivity appear slightly lower compared to the other PEO electrolytes. Please note that the 14wt% is the PS/DVB core, i.e. not conductivity, and also as discussed in chapter 2, due to geometrical constrains associated with its star shaped architecture and high functionality, the EO segmental dynamics close to the core are significantly slower compared to the 3-arm star or of the linear PEO electrolytes.

In terms of solid polymer electrolyte development though, one has to take into account both conductivity and mechanical properties of the polymer used. The reason S(60)PEO(60K) is included in this study is the fact that its mechanical behaviour is expected to be superior over its linear PEO analogue. Figure 4.26 plots the ion – conductivity as a function of zero shear viscosity of the S(60)PEO(60K) at *r* = 0.085 (solid black stars) along with the corresponding values of LPEO-0.5K at r =0.055.

It is clear that while S(60)PEO(60K) has less than an order of magnitude lower conductivity than To support this argument, zero sheer viscosity was measured for LPEO-0.55K and S(60)PEO(60K) electrolytes. In Figure 4.26, D.C. Conductivity is plotted as a function of Zero sheer viscosity.

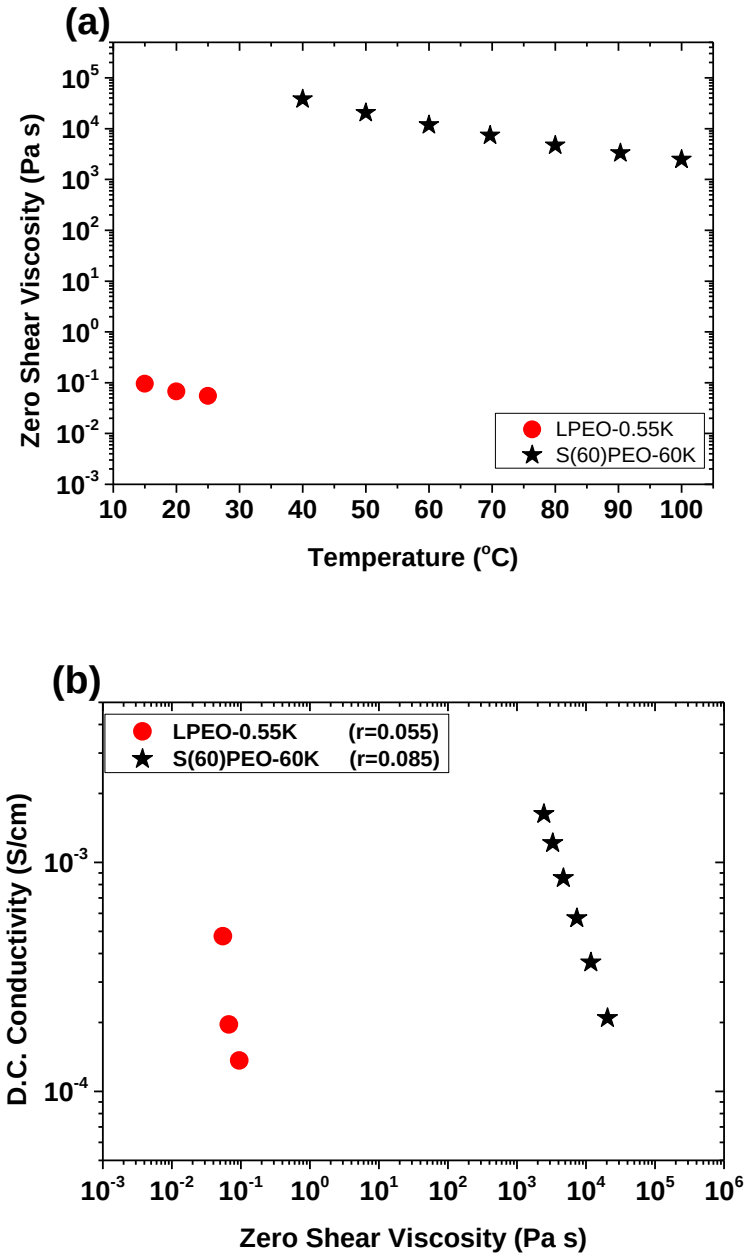

Figure 4.26 : (a) Zero shear viscosity as a function of Temperature and (b) D.C. Conductivity as a function of Zero shear viscosity for LPEO-0.55K and S(60)PEO(60K) at their best performing molar ratio *r.*

From Figure 4.26 we see that for the same conductivity the star based electrolyte (S(60PEO(60K):LiTFSI *r*=0.055) shows 5 orders of magnitude higher viscosity, an extreme difference that makes it much more suitable for solid state electrolyte applications.

5.Conclusions

Starting with thermal properties of the polymer electrolytes under investigation in this study, we observed that in both linear and star polymers, the addition of LiTFSI reduces the degree of crystallinity as well as the melting and crystallization temperatures of the polymer electrolytes as Li^+ forms complexes with the oxygen atoms of PEO. While the degree of crystallinity of all linear molecules decreased with the same rate with *r*, star-shaped PEO with a large number of 60 arms, showed a weaker dependence on *r*, implying that macromolecular geometrical constrains, imposed by the star architecture, reduce the interaction of the LiTFSI salt with the PEO. Finally, for all polymers, the glass transition temperature showed a linear increase as the molar ratio, *r* of the salt was increased.

For the electrical characterization of the prepared electrolytes, an environmental chamber was designed, manufactured, optimized and tested as well as a complementary temperature controller and a cell with well known sample dimensions. Measurements on linear PEO with a molecular weight of 5 kg/mol were in an excellent agreement with the literature. .

All the electrolytes showed a non-monotonic dependence of their conductivity on salt's molar ratio *r.* There is an initial increase in σ with *r* due to the increasing concentration of ions, reaches a maximum at r_{max} and then decrease with r due to the slow-down of segmental dynamics with *r*. Interestingly, we observed that r_{max} is temperature dependent and shifts to larger values with increasing temperature. Raman measurements revealed that the degree of LiTFSI dissociation, and hence the ion density, is unaffected to the temperature range in our study, indicating that the shift observed in r_{max} is primarily due to the change in the segmental dynamics with temperature.

We observed a significant effect of the molecular weight of linear PEO chain on the ion conductivity properties of PEO based electrolytes. In particular we showed

that for $M_w < M_e$ (M_e is the molecular weight for entanglement, i.e. for PEO M_e~2*kg/mol*)), the ionic conductivity increases with decreasing molecular weight. This is due to the fact that for $M_w < M_e$, ion transport occurs via the diffusion of the entire linear PEO chain with the coordinated ion, while for $M_w > M_e$ ion diffusion is primarily mediated by segmental dynamics and Li^+ hopping between adjustment oxygen atoms with the process of breaking/forming Li-O bonds. Noticeably, we showed that r_{max} has a M_w dependence for the LPEO electrolytes. In particular for the LPEO-0.55K the r_{max} ≈ 0.055 while for the LPEO-5K, r_{max} ≈ 0.085. The analysis of the thermal properties of the linear PEO electrolytes showed that for the LPEO-5K the maximum in ion-conductivity occurs at the *r* concentration that LPEO is amorphous; LPEO has a T_c above room temperature. In other words, the r_{max} for the LPEO-5K is not dictated by the competition of the ion concentration and segmental dynamics, as in the case of LPEO-0.55K that is amorphous at room temperature, but rather by the presence of semicrystalline regions that decrease ion conductivity.

Regarding the low functionality and low molecular weight star-shaped PEO, its conductivity was comparable to its linear analogue, yet managed to stay amorphous at lower temperatures due to its lower crystallization/melting temperatures. For the larger S(60)PEO(60K) star PEO, the ion conductivity was measured to be lower, less than an order of magnitude than that of linear PEOs. Nevertheless, the rheological measurements showed that S(60)PEO(60K) have a 6 orders of magnitude higher viscosity than the linear PEO with the highest conductivity. Our study indicates that the use of high-functionality star-shaped PEO polymer may hold the key for the synthesis of polymer electrolytes that have simultaneously high viscosity and conductivity.

Bibliography

(1) BP Statistical Review of World Energy 2020. **2020**.

(2) Linden, D.; Reddy, T. B. Handbook of Batteries. *Choice Rev. Online* **1995**, *33* (04), 33-2144-33–2144. https://doi.org/10.5860/choice.33-2144.

(3) Energizer Brands, L. Alkaline Manganese Dioxide Handbook and Application Manual. **2018**, 1–15.

(4) Yoshiaki Kato, Zempachi Ogumi, J. M. P. M. *Lithium-Ion Batteries: Overview, Simulation, and Diagnostics*; Kato, Y., Ogumi, Z., Martín, J. M. P., Eds.; Jenny Stanford Publishing, 2019. https://doi.org/10.1201/9780429259340.

(5) Glynos, E.; Pantazidis, C.; Sakellariou, G. Designing All-Polymer Nanostructured Solid Electrolytes: Advances and Prospects. *ACS Omega* **2020**. https://doi.org/10.1021/acsomega.9b04098.

(6) Wang, R.; Cui, W.; Chu, F.; Wu, F. Lithium Metal Anodes: Present and Future. *Journal of Energy Chemistry*. Elsevier B.V. and Science Press 2020, pp 145–159. https://doi.org/10.1016/j.jechem.2019.12.024.

(7) Bouchet, R. Batteries: A Stable Lithium Metal Interface. *Nat. Nanotechnol.* **2014**, *9* (8), 572–573. https://doi.org/10.1038/nnano.2014.165.

(8) Lin, D.; Liu, Y.; Cui, Y. Reviving the Lithium Metal Anode for High-Energy Batteries. *Nat. Nanotechnol.* **2017**, *12* (3), 194–206. https://doi.org/10.1038/nnano.2017.16.

(9) Tarascon, J.-M.; Armand, M. Issues and Challenges Facing Rechargeable Lithium Batteries. *Nature* **2001**, *414* (6861), 359–367. https://doi.org/10.1038/35104644.

(10) Wei, S.; Choudhury, S.; Tu, Z.; Zhang, K.; Archer, L. A. Electrochemical Interphases for High-Energy Storage Using Reactive Metal Anodes. *Acc. Chem. Res.* **2018**, *51* (1), 80–88. https://doi.org/10.1021/acs.accounts.7b00484.

(11) Monroe, C.; Newman, J. The Impact of Elastic Deformation on Deposition Kinetics at Lithium/Polymer Interfaces. *J. Electrochem. Soc.* **2005**, *152* (2), A396. https://doi.org/10.1149/1.1850854.

(12) Stone, G. M.; Mullin, S. A.; Teran, A. A.; Hallinan, D. T.; Minor, A. M.; Hexemer, A.; Balsara, N. P. Resolution of the Modulus versus Adhesion Dilemma in Solid Polymer Electrolytes for Rechargeable Lithium Metal Batteries. *J. Electrochem. Soc.* **2012**, *159* (3), A222–A227. https://doi.org/10.1149/2.030203jes.

(13) Zhu, Y.; He, X.; Mo, Y. Origin of Outstanding Stability in the Lithium Solid Electrolyte Materials: Insights from Thermodynamic Analyses Based on First-Principles Calculations. *ACS Appl. Mater. Interfaces* **2015**, *7* (42), 23685–23693. https://doi.org/10.1021/acsami.5b07517.

(14) Fenton, D. E.; Parker, J. M.; Wright, P. V. Complexes of Alkali Metal Ions with Poly(Ethylene Oxide). *Polymer (Guildf).* **1973**, *14* (11), 589. https://doi.org/10.1016/0032-3861(73)90146-8.

(15) Armand, M. Polymer Solid Electrolytes - an Overview. *Solid State Ionics* **1983**, *9–10*, 745–754. https://doi.org/https://doi.org/10.1016/0167-2738(83)90083-8.

(16) Varzi, A.; Raccichini, R.; Passerini, S.; Scrosati, B. Challenges and Prospects of the Role of Solid Electrolytes in the Revitalization of Lithium Metal Batteries. *J. Mater. Chem. A* **2016**, *4* (44), 17251–17259. https://doi.org/10.1039/c6ta07384k.

(17) Xue, Z.; He, D.; Xie, X. Poly(Ethylene Oxide)-Based Electrolytes for Lithium-Ion Batteries. *J. Mater. Chem. A* **2015**, *3* (38), 19218–19253. https://doi.org/10.1039/c5ta03471j.

(18) Berthier, C.; Gorecki, W.; Minier, M.; Armand, M. B.; Chabagno, J. M.; Rigaud, P. Microscopic Investigation of Ionic Conductivity in Alkali Metal Salts-Poly(Ethylene Oxide) Adducts. *Solid State Ionics* **1983**, *11* (1), 91–95. https://doi.org/10.1016/0167-2738(83)90068-1.

(19) Gadjourova, Z.; Andreev, Y. G.; Tunstall, D. P.; Bruce, P. G. Ionic Conductivity in

Crystalline Polymer Electrolytes. *Nature* **2001**, *412* (6846), 520–523. https://doi.org/10.1038/35087538.

(20) Marzantowicz, M.; Dygas, J. R.; Krok, F.; Tomaszewska, A.; Florjańczyk, Z.; Zygadło-Monikowska, E.; Lapienis, G. Star-Branched Poly(Ethylene Oxide) LiN(CF3SO2)2: A Promising Polymer Electrolyte. *J. Power Sources* **2009**, *194* (1), 51–57. https://doi.org/10.1016/j.jpowsour.2009.01.011.

(21) Mindemark, J.; Lacey, M. J.; Bowden, T.; Brandell, D. Beyond PEO—Alternative Host Materials for Li+-Conducting Solid Polymer Electrolytes. *Prog. Polym. Sci.* **2018**, *81*, 114–143. https://doi.org/10.1016/j.progpolymsci.2017.12.004.

(22) Thelen, J. L.; Wang, A. A.; Chen, X. C.; Jiang, X.; Schaible, E.; Balsara, N. P. Correlations between Salt-Induced Crystallization, Morphology, Segmental Dynamics, and Conductivity in Amorphous Block Copolymer Electrolytes. *Macromolecules* **2018**, *51* (5), 1733–1740. https://doi.org/10.1021/acs.macromol.7b02415.

(23) Marzantowicz, M.; Dygas, J. R.; Krok, F.; Nowiński, J. L.; Tomaszewska, A.; Florjańczyk, Z.; Zygadło-Monikowska, E. Crystalline Phases, Morphology and Conductivity of PEO:LiTFSI Electrolytes in the Eutectic Region. *J. Power Sources* **2006**, *159* (1 SPEC. ISS.), 420–430. https://doi.org/10.1016/j.jpowsour.2006.02.044.

(24) Edman, L. Ion Association and Ion Solvation Effects at the Crystalline-Amorphous Phase Transition in PEO-LiTFSI. *J. Phys. Chem. B* **2000**, *104* (31), 7254–7258. https://doi.org/10.1021/jp000082d.

(25) Lascaud, S.; Perrier, M.; Vallée, A.; Besner, S.; Prud'homme, J.; Armand, M. Phase Diagrams and Conductivity Behavior of Poly(Ethylene Oxide)-Molten Salt Rubbery Electrolytes. *Macromolecules* **1994**, *27* (25), 7469–7477. https://doi.org/10.1021/ma00103a034.

(26) Mark, J. E. *Physical Properties of Polymers Handbook*; Mark, J. E., Ed.; Springer New York: New York, NY, 2007; Vol. 199. https://doi.org/10.1007/978-0-387-69002-5.

(27) Hallinan, D. T.; Balsara, N. P. Polymer Electrolytes. *Annu. Rev. Mater. Res.* **2013**, *43* (1), 503–525. https://doi.org/10.1146/annurev-matsci-071312-121705.

(28) Wang, Y.; Fan, F.; Agapov, A. L.; Saito, T.; Yang, J.; Yu, X.; Hong, K.; Mays, J.; Sokolov, A. P. Examination of the Fundamental Relation between Ionic Transport and Segmental Relaxation in Polymer Electrolytes. *Polymer (Guildf).* **2014**, *55* (16), 4067–4076. https://doi.org/10.1016/j.polymer.2014.06.085.

(29) Pesko, D. M.; Timachova, K.; Bhattacharya, R.; Smith, M. C.; Villaluenga, I.; Newman, J.; Balsara, N. P. Negative Transference Numbers in Poly(Ethylene Oxide)-Based Electrolytes. *J. Electrochem. Soc.* **2017**, *164* (11), E3569–E3575. https://doi.org/10.1149/2.0581711jes.

(30) Gray, F. M. Polymer Electrolytes II: Physical Principles. In *Solid State Electrochemistry*; Cambridge University Press, 1994; pp 119–162. https://doi.org/10.1017/CBO9780511524790.007.

(31) Grest, G. S.; Fetters, L. J.; Huang, J. S.; Richter, D. Star Polymers: Experiment, Theory, and Simulation; 2007; Vol. XCIV, pp 67–163. https://doi.org/10.1002/9780470141533.ch2.

(32) Adams, C. H.; Brereton, M. G.; Hutchings, L. R.; Klein, P. G.; McLeish, T. C. B.; Richards, R. W.; Ries, M. E. Deuterium NMR Study of Selectively Labeled Polybutadiene Star Polymers. *Macromolecules* **2000**, *33* (19), 7101–7106. https://doi.org/10.1021/ma0008490.

(33) Likos, C. N. *Effective Interactions in Soft Condensed Matter Physics*; 2001; Vol. 348. https://doi.org/10.1016/S0370-1573(00)00141-1.

(34) Likos, C. N.; Löwen, H.; Watzlawek, M.; Abbas, B.; Jucknischke, O.; Allgaier, J.; Richter, D. Star Polymers Viewed as Ultrasoft Colloidal Particles. *Phys. Rev. Lett.* **1998**, *80* (20), 4450–4453. https://doi.org/10.1103/PhysRevLett.80.4450.

(35) Watzlawek, M.; Likos, C. N.; Löwenen, H. Phase Diagram of Star Polymer Solutions. *Phys. Rev. Lett.* **1999**, *82* (26), 5289–5292. https://doi.org/10.1103/PhysRevLett.82.5289.

(36) Snijkers, F.; Cho, H. Y.; Nese, A.; Matyjaszewski, K.; Pyckhout-Hintzen, W.; Vlassopoulos, D. Effects of Core Microstructure on Structure and Dynamics of Star Polymer Melts: From Polymeric to Colloidal Response. *Macromolecules* **2014**, *47* (15), 5347–5356. https://doi.org/10.1021/ma5008336.

(37) Pakula, T.; Vlassopoulos, D.; Fytas, G.; Roovers, J. Structure and Dynamics of Melts of Multiarm Polymer Stars. *Macromolecules* **1998**, *31* (25), 8931–8940. https://doi.org/10.1021/ma981043r.

(38) Vlassopoulos, D.; Pakula, T.; Fytas, G.; Roovers, J.; Karatasos, K.; Hadjichristidis, N. Ordering and Viscoelastic Relaxation in Multiarm Star Polymer Melts. *Europhys. Lett.* **1997**, *39* (6), 617–622. https://doi.org/10.1209/epl/i1997-00403-3.

(39) Chremos, A.; Glynos, E.; Green, P. F. Structure and Dynamical Intra-Molecular Heterogeneity of Star Polymer Melts above Glass Transition Temperature. *J. Chem. Phys.* **2015**, *142* (4), 0–9. https://doi.org/10.1063/1.4906085.

(40) Gury, L.; Gauthier, M.; Cloitre, M.; Vlassopoulos, D. Colloidal Jamming in Multiarm Star Polymer Melts. *Macromolecules* **2019**, 3–9. https://doi.org/10.1021/acs.macromol.9b00674.

(41) Johnson, K. J.; Glynos, E.; Sakellariou, G.; Green, P. Dynamics of Star-Shaped Polystyrene Molecules: From Arm Retraction to Cooperativity. *Macromolecules* **2016**, *49* (15), 5669–5676. https://doi.org/10.1021/acs.macromol.6b00456.

(42) Vlassopoulos, D.; Fytas, G.; Pakula, T.; Roovers, J. Multiarm Star Polymers Dynamics. *Journal of Physics Condensed Matter*. 2001. https://doi.org/10.1088/0953-8984/13/41/202.

(43) Rouse, P. E. A Theory of the Linear Viscoelastic Properties of Dilute Solutions of Coiling Polymers. *J. Chem. Phys.* **1953**, *21* (7), 1272–1280. https://doi.org/10.1063/1.1699180.

(44) Ferry, J. D. *Viscoelastic Properties of Polymers*; 1980. https://doi.org/10.1149/1.2428174.

(45) Rubinstein, M.; Colby, R. H. *Polymer Physics*; Oxford University Press, 2003.

(46) de Gennes, P. G.; Witten, T. A. Scaling Concepts in Polymer Physics. *Physics Today*. 1980, pp 51–54. https://doi.org/10.1063/1.2914118.

(47) Ball, R. C.; McLeish, T. C. B. Dynamic Dilution and the Viscosity of Star Polymer Melts. *Macromolecules* **1989**, *22* (4), 1911–1913. https://doi.org/10.1021/ma00194a066.

(48) Fetters, L. J.; Kiss, A. D.; Pearson, D. S.; Quack, G. F.; Vitus, F. J. Rheological Behavior of Star-Shaped Polymers. *Macromolecules* **1993**, *26* (4), 647–654. https://doi.org/10.1021/ma00056a015.

(49) Pearson, D. S.; Helfand, E. Viscoelastic Properties of Star-Shaped Polymers. *Macromolecules* **1984**, *17* (4), 888–895. https://doi.org/10.1021/ma00134a060.

(50) Zhang, X.; Daigle, J.-C.; Zaghib, K. Comprehensive Review of Polymer Architecture for All-Solid-State Lithium Rechargeable Batteries. *Materials (Basel).* **2020**, *13* (11), 2488. https://doi.org/10.3390/ma13112488.

(51) Stowe, M. K.; Liu, P.; Baker, G. L. Star Poly(Ethylene Oxide) as a Low Temperature Electrolyte and Crystallization Inhibitor. *Chem. Mater.* **2005**, *17* (26), 6555–6559. https://doi.org/10.1021/cm050673m.

(52) Wang, A.; Xu, H.; Zhou, Q.; Liu, X.; Li, Z.; Gao, R.; Wu, N.; Guo, Y.; Li, H.; Zhang, L. A New All-Solid-State Hyperbranched Star Polymer Electrolyte for Lithium Ion Batteries: Synthesis and Electrochemical Properties. *Electrochim. Acta* **2016**, *212*, 372–379. https://doi.org/10.1016/j.electacta.2016.07.003.

(53) Glynos, E.; Papoutsakis, L.; Pan, W.; Giannelis, E. P.; Nega, A. D.; Mygiakis, E.; Sakellariou, G.; Anastasiadis, S. H. Nanostructured Polymer Particles as Additives for High Conductivity, High Modulus Solid Polymer Electrolytes. *Macromolecules* **2017**, *50* (12), 4699–4706. https://doi.org/10.1021/acs.macromol.7b00789.

(54) Niitani, T.; Amaike, M.; Nakano, H.; Dokko, K.; Kanamura, K. Star-Shaped

Polymer Electrolyte with Microphase Separation Structure for All-Solid-State Lithium Batteries. *J. Electrochem. Soc.* **2009**, *156* (7), A577. https://doi.org/10.1149/1.3129245.

(55) Vallée, A.; Besner, S.; Prud'Homme, J. Comparative Study of Poly(Ethylene Oxide) Electrolytes Made with LiN(CF3SO2)2, LiCF3SO3 and LiClO4: Thermal Properties and Conductivity Behaviour. *Electrochim. Acta* **1992**, *37* (9), 1579–1583. https://doi.org/10.1016/0013-4686(92)80115-3.

(56) Hohne, G.; Hemminger, W. F.; Flammersheim, H. J. *Differential Scanning Calorimetry*.

(57) Klančnik, G.; Medved, J.; Mrvar, P. Differential Thermal Analysis (DTA) and Differential Scanning Calorimetry (DSC) as a Method of Material Investigation. *Mater. Geoenvironment* **2010**, *57* (1), 127–142.

(58) Papananou, H. Polymer Structure and Dynamics under Confinement, University of Crete, 2017.

(59) Shih, H.; Lo, T.-C. *Electrochemical Impedance Spectroscopy for Battery Research and Development*; 1996.

(60) Yuan, X.; Wang, H.; Colin Sun, J.; Zhang, J. AC Impedance Technique in PEM Fuel Cell Diagnosis-A Review. *Int. J. Hydrogen Energy* **2007**, *32* (17), 4365–4380. https://doi.org/10.1016/j.ijhydene.2007.05.036.

(61) Von Hauff, E. Impedance Spectroscopy for Emerging Photovoltaics. *J. Phys. Chem. C* **2019**, *123* (18), 11329–11346. https://doi.org/10.1021/acs.jpcc.9b00892.

(62) Encinas-Sánchez, V.; de Miguel, M. T.; Lasanta, M. I.; García-Martín, G.; Pérez, F. J. Electrochemical Impedance Spectroscopy (EIS): An Efficient Technique for Monitoring Corrosion Processes in Molten Salt Environments in CSP Applications. *Sol. Energy Mater. Sol. Cells* **2019**, *191* (August 2018), 157–163. https://doi.org/10.1016/j.solmat.2018.11.007.

(63) Hinton, A. J. Determination of Coating Adhesion Using Electrochemical

Impedance Spectroscopy.

(64) Biodynamics Corporation. Bioimpedance Measurements https://www.biodyncorp.com/knowledgebase/bioimpedance_measurements.html.

(65) PalmSens. Bode and Nyquist Plot https://www.palmsenscorrosion.com/knowledgebase/bode-and-nyquist-plot/.

(66) Winie, T.; Arof, A. K.; Thomas, S. *Polymer Electrolytes: Characterization Techniques and Energy Applications*; John Wiley & Sons, 2020.

(67) Dreezen, G.; Koch, M. H. J.; Reynaers, H.; Groeninckx, G. Miscible Binary Blends of Poly(Ethylene Oxide) and an Amorphous Aromatic Polyamide (Aramide 34I): Crystallization, Melting Behavior and Semi-Crystalline Morphology. *Polymer (Guildf).* **1999**, *40* (23), 6451–6463. https://doi.org/10.1016/S0032-3861(98)00849-0.

(68) Zheng, Q.; Pesko, D. M.; Savoie, B. M.; Timachova, K.; Hasan, A. L.; Smith, M. C.; Miller, T. F.; Coates, G. W.; Balsara, N. P. Optimizing Ion Transport in Polyether-Based Electrolytes for Lithium Batteries. *Macromolecules* **2018**, *51* (8), 2847–2858. https://doi.org/10.1021/acs.macromol.7b02706.

(69) Beauregard, B. Arduino PID Library https://github.com/br3ttb/Arduino-PID-Library.

(70) Adafruit. Adafruit_MAX31865 https://github.com/adafruit/Adafruit_MAX31865.

(71) Stoffregen, P.; Boesing, F. EEPROM Library V2.0 for Arduino https://github.com/PaulStoffregen/EEPROM.

(72) Liquid Crystal Library for Arduino https://github.com/arduino-libraries/LiquidCrystal.

(73) Timachova, K.; Watanabe, H.; Balsara, N. P. Effect of Molecular Weight and Salt Concentration on Ion Transport and the Transference Number in Polymer

Electrolytes. *Macromolecules* **2015**, *48* (21), 7882–7888. https://doi.org/10.1021/acs.macromol.5b01724.

(74) Glynos, E.; Petropoulou, P.; Mygiakis, E.; Nega, A. D.; Pan, W.; Papoutsakis, L.; Giannelis, E. P.; Sakellariou, G.; Anastasiadis, S. H. Leveraging Molecular Architecture To Design New, All-Polymer Solid Electrolytes with Simultaneous Enhancement in Modulus and Ionic Conductivity. *Macromolecules* **2018**, *51* (7), 2542–2550. https://doi.org/10.1021/acs.macromol.7b02394.

(75) Schaefer, J. L.; Moganty, S. S.; Yanga, D. A.; Archer, L. A. Nanoporous Hybrid Electrolytes. *J. Mater. Chem.* **2011**, *21* (27), 10094–10101. https://doi.org/10.1039/C0JM04171H.

(76) Srivastava, S.; Schaefer, J. L.; Yang, Z.; Tu, Z.; Archer, L. A. 25th Anniversary Article: Polymer–Particle Composites: Phase Stability and Applications in Electrochemical Energy Storage. *Adv. Mater.* **2014**, *26* (2), 201–234. https://doi.org/10.1002/adma.201303070.